Models of convection and segregation in heterogeneous partially molten crustal roots with a VOF method - Part I: flow regimes

Aurélie Louis–napoléon, Thomas Bonometti, Muriel Gerbault, Roland Martin, Olivier Vanderhaeghe

To cite this version:

Aurélie Louis–napoléon, Thomas Bonometti, Muriel Gerbault, Roland Martin, Olivier Vanderhaeghe. Models of convection and segregation in heterogeneous partially molten crustal roots with a VOF method - Part I: flow regimes. Geophysical Journal International, 2022, 10.1093/gji/ggab510 . hal-03551831

HAL Id: hal-03551831
https://hal.science/hal-03551831

Submitted on 1 Feb 2022

submitted to *Geophys. J. Int.*

Models of convection and segregation in heterogeneous partially molten crustal roots with a VOF method - Part I: flow regimes

Aurélie Louis–Napoléon[1,2], Thomas Bonometti[1], Muriel Gerbault[2]

Roland Martin[2], Olivier Vanderhaeghe[2]

SUMMARY

We investigate numerically some thermo-mechanical conditions for the development of crustal scale diapirism and convection in a heterogeneous continental crust independently from the action of regional tectonics. Here, we consider a hot crust where convection is generated below a melting front, with unmolten and partially molten domains of specific temperature and strain-rate dependent power-law rheologies. We take advantage of the VOF (Volume Of Fluid) method to capture the coalescence and separation of deformable inclusions in the partially molten domain. The inclusions, of several hundred meters in size, are more or less dense and more or less viscous with respect to the ambient medium (they also behave with a power-law rheology). We restrict our study to a 20 Myr time scale, during which gravitational dynamics may dominate over lateral tectonics and lithospheric thermal reequilibration. The motion of these inclusions during the development of gravitational instabilities allows to define distinct flow regimes that depend on two Rayleigh numbers denoted Ra_{UM} and Ra_{PM}, for the unmolten and partially molten rock properties, respectively. A 'suspension' regime occurs at high Ra_{UM} and high Ra_{PM}, in which most of the light compositional heterogeneities remain entrained in the convective cells. In contrast at low Ra_{UM} and high Ra_{PM}, a 'layering' regime is characterized by merging of the light inclusions as floating clusters below the rigid upper crustal lid. This regime occurs occurs in association with a sharp viscosity gradient at upper-to-middle crust transitional depths. In these two regimes, the dense inclusions accumulate at the bottom of the partially molten zone. Finally at moderate Ra_{PM}, a 'diapiric' regime reflects the segregation of the heavy and the light inclusions, respectively downward and upward, without global convection. These numerical experiments lead to a first order evaluation of the physical parameters required for the segregation of deformable inclusions of variable densities and convection, in a partially molten crust, and provide insights on the conditions for the development of migmatite domes. Geological data indicate that these processes likely occur in a large number of settings from Archean to Phanerozoic times, and contribute to the differentiation of the continental crust.

Key words: Diapirism, Heat generation and transport , Rheology: crust and lithosphere, Dynamics: gravity and tectonics, Numerical modelling, Composition and structure of the continental crust

1 Introduction

The continental crust is compositionally differentiated into a mafic lower crust, an intermediate middle crust and a felsic upper crust (Rudnick & Fountain 1995; Mooney et al. 2002). At the grain scale, this differentiation primarily results from element fractionation during partial melting, magma transfer and fractional crystallisation (e.g. Sawyer 1994; Brown 1995; Leitch & Weinberg 2002; Vanderhaeghe 2009). Melt segregation and magma transfer from the grain scale to the crustal scale are attested by the presence of migmatites, dikes, plutons and volcanoes. Moreover, kilometric size domes cored by migmatites, typical of hot Archean-Proterozoic crust and thermally mature Phanerozoic orogenic belts, testify of the upward ”en masse” motion of the deep, partially molten root of the crust. These domes have been attributed to the combined influence of regional tectonics and diapiric gravitational instabilities (Ramberg 1967; Cruden et al. 1995; Weinberg & Podladchikov 1994; Perchuk et al. 1992; Van Kranendonk et al. 2004; Whitney et al. 2004; Schenker et al. 2012). More specifically, in several orogenic contexts, such massive exhumation of the orogenic crustal root has been invoked to develop independently from tectonics, e.g. during the transition from compressional to extensional regional tectonics (Ganne et al. 2014; Kruckenberg et al. 2011; Gerbault et al. 2018). Furthermore, some of migmatite domes have recently been interpreted as reflecting crustal scale convection on a timescale of Myr to tens of Myr, based on their structural, petrological and geochronological record (Riel et al. 2016; Vanderhaeghe et al. 2018). Crustal convection has been also assessed by numerical modeling (Babeyko et al. 2002; Schenker et al. 2012; Cao et al. 2016). As a complement to these previous models, in this paper we investigate thermo-mechanical conditions for the development of crustal scale diapirism and convection and their impact on the segregation of crustal material, independently from the action of regional tectonics.

In terms of rheology, a key property of crustal rocks is their heterogeneous composition and their non-linear behaviour. Decades of laboratory rock experiments have explored the influence of composition, water, temperature, pressure; various modes of deformation were found to compete at small scale, such as grain boundary sliding, grain boundary diffusion, dislocation creep, and studies have managed to upscale these deformation modes as a function of temperature and strain-rate power-law relationships (e.g. Kohlstedt et al. 1995; Bürgmann & Dresen 2008). The additional complexities brought by partial melting leads to an overall drastic decrease in viscosity (Arzi 1978; Vigneresse 1995; Rosenberg & Handy 2005; Vanderhaeghe 2009), which facilitates gravitational destabilisation.

Hence, convection in hot orogenic crust can be viewed as convection below a melting front between solid (unmolten) and liquid (partially molten) phases. This kind of system has been investigated for environments such as the Earth's core and mantle, magma chambers or other types of industrial fluids (see e.g. Davis et al. 1984; Ulvrová et al. 2012; Esfahani et al. 2018; Favier et al. 2019; Purseed et al. 2020). It was shown that when compositional heterogeneities evolve in a convective system, two regimes can occur, namely 'suspension' or 'layering' (Sparks et al. 1984; Martin & Nokes 1988; Höink et al. 2005; Lavorel & Le Bars 2009; Patočka et al. 2020; Sturtz et al. 2021).

During melting, the separation, coalescence and segregation of layers of contrasted compositions occur. Minerals can aggregate at different scales and form clusters of more or less viscous, more or less dense material with respect to the surrounding environment. This aggregation depends on thermodynamic variables (pressure-temperature) and metamorphic reactions, and can result from the local dynamics of initial heterogeneities (Culha et al. 2020) or from porous flow dynamics (Sawyer 1994; Rabinowicz & Ceuleneer 2005; Brown 2010, 1995; Katz & Weatherley 2012; Connolly & Podladchikov 2015; Riel et al. 2016). Several models have attempted to account for the chemical and lithological heterogeneities of partially molten crust over large geological time and space scales by considering an equivalent single phase medium with strongly non-linear rheology (e.g. Gerya & Burg 2007; Schenker et al. 2012; Cao et al. 2016; Gerbault et al. 2018), and recently by accounting for two-phase flow in porous media (Schmeling et al. 2019; Keller et al. 2013). Whereas the latter studies manage to decipher quite well the conditions for melt transport via whole matrix motion or via localised porous flow, they remain challenging to achieve numerically, and a gap still remains in bridging the influence of compositional heterogeneities at the intermediate scale, e.g. that of several hundred meters, between the pore scale and the crustal scale. Hence here, we choose to formulate a conceptual representation of crustal heterogeneities of sizes of the order of several hundred meters, by introducing in the models, heterogeneous inclusions of that size. While the continental crust has on average a composition equivalent to that of a granodiorite, it is in fact very heterogeneous, as a result of many superimposed sedimentary, magmatic and tectonic processes over time, that lead to a variety of compositions ranging from mafic to felsic (Dewey 1986; Wedepohl 1995; Rudnick et al. 2003). The propension of these different rock types to melt is also variable (Thompson & Connolly 1995) and this inherited layering at scales of meters to kilometers is further enhanced by partial melting and melt/solid segregation (Brown 1995; Vanderhaeghe et al. 2003; Kisters et al. 2009; Toé et al. 2013).

From a modeling view point, the influence of rigid inclusions on fluid flow has been explored at the scale of magma-chambers (Suckale et al. 2012; Yamato et al. 2015; Shibano et al. 2013) or at that of the whole mantle (Patočka et al. 2020), but seldom at the crustal scale (Deubelbeiss & Kaus 2008). In fact no previous model has explicitly incorporated deformable compositional heterogeneities in a partially molten crust, most probably because numerical codes encounter issues with mass conservation and numerical diffusion at layers interfaces (Deubelbeiss & Kaus 2008; Schmeling et al. 2008; Suckale et al. 2010; Hillebrand et al. 2014; Pusok et al. 2017; Heister et al. 2017). This motivates the use of a Volume-Of-Fluid (VOF) method, dedicated to the conservation of compositional interfaces. Recently, Puckett et al. (2018); Robey & Puckett (2019); Louis-Napoléon et al. (2020) have shown that the VOF method is relevant to model interfaces separating chemical compositions in geological contexts. As an alternative to the VOF method, the Level-Set method (Osher & Sethian 1988; Sethian & Smereka 2003) was employed by Suckale et al. (2010) to model the flow dynamics of magmatic chambers. This method uses a fix grid like the VOF method. It captures the interfaces dynamics by solving a transport equation for the signed distance function, also called level-set, while in the VOF method the transport equation deals with the phases volume fraction. The level-set method, when coupled with the ghost fluid method (Fedkiw et al. 1999), is particularly accurate when specific processes occur at materials interfaces (e.g. phase change, surface tension).

Here, we take advantage of the VOF method to capture the coalescence and separation of deformable inclusions of several hundred meters in size; we incorporate three different fluid-phase compositions which all obey to temperature and strain-rate dependent properties. Because the actual distribution of heterogeneities is variable in the continental crust in terms of amplitude, length-scales, and interconnectivity, we set up models of an orogenic crustal domain containing an ad-hoc distribution of chemical heterogeneities, which are topologically isolated rather than interconnected. We investigate the consequences of such crustal heterogeneity on the dynamics of buoyancy-driven flow. At the onset of our simulations, partial melting is absent, but it initiates at given solidus-liquidus temperature thresholds resulting from the applied internal and basal heat sources.

We explore the interaction between convective flow and inclusions motion with evolving Rayleigh numbers, as a consequence of basal and internal heating. Our purpose here is to describe with two-dimensional (2D) simulations the resulting regimes of suspension and segregation of light and heavy inclusions in association with convective flow. An application to the specific case of Naxos's domes (Greece) is provided in a companion paper (*Louis-Napoleon et al., part II, in prep*). Here, the physical framework is first described (section 2), then the numerical setup is presented (section 3). Note that the mathematical details of the VOF method are available in Louis-Napoléon et al. (2020), hence it is only briefly exposed here. We present in section 4 various model cases of a partially molten crust, first without, then with heterogeneities. We discuss our results in Section 5, with a synthetic representation of the observed regimes, and propose some guidelines to help identifying these regimes on the field. Finally, conclusions and perspectives are drawn in Section 6.

2 Physical model

2.1 System of equations

In the present work, we consider the motion of a fluid whose properties may change due to partial melting, and inside which spatial heterogeneities may appear. The local properties (density, viscosities) vary as a function of temperature and strain rate. A schematic representation of the flow we intend to investigate is displayed in Figure 1. In order to capture the motion of the various fluid phases, we introduce local indicators denoted by their volume fractions C_i (subscript i defines the phase).

The general set of governing equations describes the transport of the volume fractions, mass, momentum and energy, respectively expressed as:

$$\frac{\partial C_i}{\partial t} + \mathbf{U} \cdot \nabla C_i = -\nabla \cdot (\mathbf{U}_r C_r), \tag{1}$$

$$\nabla \cdot \mathbf{U} = 0, \tag{2}$$

$$\rho_{ref} \frac{\partial \mathbf{U}}{\partial t} + \rho_{ref} \mathbf{U} \cdot \nabla \, \mathbf{U} = -\nabla P + \tilde{\rho} \mathbf{g} + \nabla \cdot [\tilde{\mu}(\nabla \mathbf{U} + (\nabla \mathbf{U})^T)], \tag{3}$$

$$\frac{\partial T}{\partial t} + \mathbf{U} \cdot \nabla T = \nabla \cdot (\kappa(T) \nabla T) + \frac{H_r}{C_p(T)}, \tag{4}$$

where $\mathbf{U}$, P, T are the local velocity, pressure and temperature of the fluid, respectively, and $\mathbf{g}$ is the gravitational acceleration. Note that the r.h.s. of Eq. (1) is artificially added to reduce the effects of numerical smearing of the interface in the present numerical approach, namely OpenFOAM. We refer the reader to Berberović et al. (2009) and Louis-Napoléon et al. (2020) for more details about OpenFOAM and the numerical approach.

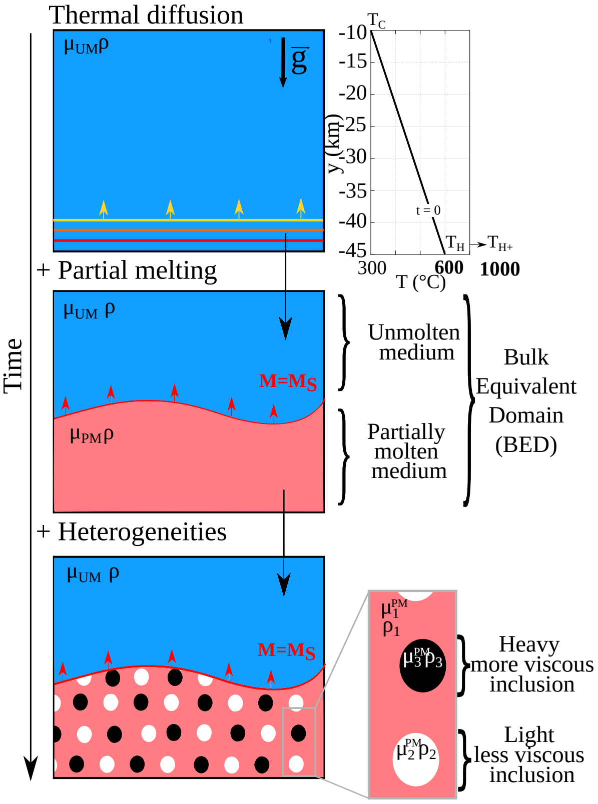

Figure 1. Schematic representation of the numerical setup. At time $t = 0$ Myr, the basal temperature is switched from $T_H = 600^o$C to $T_{H+} = 1000^o$C. First, heat diffuses from the base of the domain across the bulk equivalent domain (BED, blue and red regions). As melting occurs phase properties evolve as prescribed with the critical melt fraction M_S, which separates the unmolten medium (UM) from the partially molten medium (PM) in the BED. Note that convection may develop at this stage. In a second modeling step, spatial heterogeneities are accounted for (black and white inclusions, for heavy, more viscous, and light, less viscous material, respectively). These inclusions become active only when the melt fraction exceeds the critical fraction M_S: they may then segregate vertically or be carried away within the convective cells.

In Eq. (3), ρ_{ref} and $\tilde{\rho}$ are the reference and the local density, respectively, while $\tilde{\mu}$ is the local dynamic viscosity. These quantities are detailed below. In Eq. (4), $\kappa(T)$ is the thermal diffusivity (in $\mathrm{m}^2.\mathrm{s}^{-1}$), H_r is the radioactive heating (in $\mathrm{W.kg}^{-1}$) and $C_p(T)$ is the heat capacity (in $\mathrm{m}^2.\mathrm{s}^{-2}.\mathrm{K}^{-1}$). Here, we use the Boussinesq approximation that describes the temperature-dependency of density, and which appears only in the gravitational term $\tilde{\rho}\mathbf{g}$ of Eq. (3), namely:

$$\tilde{\rho} = \rho_{ref} \times [1 - \alpha(T - T_{ref})], \tag{5}$$

where α is the thermal expansion coefficient assumed constant in the present work ($\alpha = 3 \times 10^{-5} K^{-1}$) and T_{ref} is a reference temperature here defined as the temperature imposed at the top of the domain, namely $T_{ref} = T_C = 300^o$C at depth 10 km.

The effect of latent heating related to melting and crystallisation processes is accounted for via the dependence of κ and C_p on temperature, following Whittington et al. (2009):

$$\kappa(T) = \left| \begin{array}{ll} \left(\dfrac{567.3}{T} - 0.062\right) \cdot 10^{-6} & \text{if } T < 846 \text{ K}, \\ (0.732 - 1.35 \times 10^{-4} T) \cdot 10^{-6} & \text{if } T > 846 \text{ K}, \end{array} \right. \tag{6}$$

$$C_p(T) = \left| \begin{array}{ll} 902.7 + 0.387T - 22.6 \times 10^{-6} T^{-2} & \text{if } T < 846 \text{ K}, \\ 1037.6 + 0.146T - 216.7 \times 10^{-6} T^{-2} & \text{if } T > 846 \text{ K}. \end{array} \right. \tag{7}$$

The influence of latent heat could alternatively be explicitly incorporated in the resolution of the heat equation (4). Its influence is actually tested in Appendix 3, following the explicit expression of Ulvrová et al. (2012); with differences of about 10% observed in the flow regimes, and acknowledging that this is of the order of the range of influence of other thermal parameters such as using an identical κ and C_p amongst different material phases, we assume in the following that latent heat varies only via the dependency of κ and C_p on temperature as described in Eqs. 6 and 7, respectively.

2.2 Implementation of partial melting and heterogeneities

2.2.1 Partial melting

As a first approximation, the volumetric fraction of melt M is assumed to increase linearly with temperature, in a way similar to Gerya & Yuen (2003) or Burg & Gerya (2005) :

$$M = \frac{T - T_{sol}}{T_{liq} - T_{sol}}, \tag{8}$$

where T_{sol} and T_{liq} are the solidus and liquidus temperatures of the considered rock, respectively. As a first approximation, T_{sol} and T_{liq} are prescribed as constant values $T_{sol} = 600^o$C and $T_{liq} = 1000^o$C. Here and following the above mentioned studies, we assume distinct fluid properties according to a critical value of the melt fraction denoted M_S, cf. sections 2.2.3 and 2.2.4 below. Note also that the

1000^oC limit is imposed along the bottom boundary of the model domain, so that full melting conditions actually never occur inside the model domain. A more precise parametrization of the temperature and pressure dependency of melt would be necessary in an effort to better fit natural crustal melting systems.

2.2.2 Heterogeneities

We define a ”carrying fluid” phase, referred to as the bulk equivalent domain (BED, phase 1) and which may melt partially. We distinguish it from two other discrete fluid phases (2 and 3) that bracket the BEDs properties with extrema density and viscosity properties. These fluid phases 2 and 3 are inserted as circular inclusions throughout the model domain (Fig. 1), with phase 2 shown in white, being less dense and less viscous, and phase 3 shown in black, more dense and more viscous. With a VOF method, these three fluid phases of distinct compositions are defined by three volume fractions $0 \leq C_i \leq 1$ ($i = 1, 2, 3$) as :

- Fluid 1 = bulk equivalent domain (BED) ($C_1 = 1$, $C_2 = C_3 = 0$),
- Fluid 2 = light and low viscosity inclusions ($C_1 = 0$, $C_2 = 1$, $C_3 = 0$),
- Fluid 3 = heavy and stiff inclusions ($C_1 = C_2 = 0$, $C_3 = 1$).

When the system is unmolten ($M < M_S$), inclusions are mostly passive, i.e they behave like the bulk equivalent medium. Then, as the system is heated up and M increases up to $M \geq M_S$, the inclusions become active as their density and viscosity differ more and more from those of the BED.

As briefly described in the introduction, these two sets of inclusions (”material phases”) are supposed to represent a key heterogeneity scale of partially molten orogenic crust. This means that any kind of heterogeneous property arising at smaller scale is volume averaged into either one or the other of these two inclusions properties. Obviously, a multitude of processes occur at small scale and are related to thermo-chemical reactions, segregation and fluid percolation; while it is not our aim to account directly for these subscale processes in our study, we assume that their cumulated influence on mechanical properties (density and viscosity) characterises heterogeneities at the scale just above, e.g. that of our inclusions. Our choice of a several hundred meters size for these heterogeneities rises from various theoretical and field studies for orogenic felsic crust (e.g. Brown 2010; Edmonds et al. 2019). It allows to study the influence of characteristic size heterogeneities on the macroscale flow dynamics, without dealing with the complexities of sub-scale thermal, chemical and mechanical deformation mechanisms, nor a huge set of poorly constrained parameters.

2.2.3 *Viscosity*

Experimental studies have shown that the viscosity of felsic rocks at mid-crustal depths depends non-linearly on temperature and strain rate, and on composition (Kirby 1985; Kohlstedt et al. 1995; Ranalli 1995; Bürgmann & Dresen 2008). Since these rocks are composed of many minerals, several mechanisms of plastic deformation compete at a given time, such as cataclasis, grain boundary diffusion, Peierls locking mechanism, or dislocation creep. With no partial melting or less than a critical amount ($M < M_S$), the viscosity of crustal rocks μ_{UM}, is defined with a power-law relationship on the temperature and the second invariant of the deviatoric strain-rate $\dot{\varepsilon} = \sqrt{\left(tr(\dot{\epsilon}^2) - tr^2(\dot{\epsilon})/3\right)/2}$ with $\dot{\epsilon} = (\nabla \mathbf{U} + (\nabla \mathbf{U})^T)/2$ in s^{-1}), following Chen & Morgan (1990). Here, material incompressibility is assumed $\left(tr(\dot{\epsilon}) = \sum_{i=1}^{3} \dot{\epsilon}_{ii} = 0\right)$. While metamorphic and melting reactions do produce variations in volume, at first order these variations may be considered negligible at the several hundred meter scale of the inclusions considered here; their density contrast encompasses these related processes.

Experimental studies have also investigated the influence of partial melting on rock rheology (Arzi 1978; Van der Molen & Paterson 1979; Rutter et al. 2006; Rushmer 2001, and references therein). One of the consequences of partial melting is a sharp decrease in viscosity $\tilde{\mu}$ with melt fraction M. Studies report a first percolation threshold around 10% where the molten domain becomes interconnected within the solid matrix that maintains its coherency, and a second percolation threshold around 30% where the molten domain becomes a fluid continuum within which discontinuous fragments of the solid matrix float (Maaløe 1992; Vanderhaeghe 2009; Vigneresse 1995).

Here in our models, we approximate this transition with a single viscosity jump determined by an arbitrary volumetric melt fraction threshold, M_S. M_S for felsic rocks then stands in between 10% and 30%, and these two extreme values will be tested further below. At high melt fraction ($M > M_S$), the viscosity of partially molten felsic rock μ_{PM} becomes strongly dependent on M. Various laws have been proposed in the literature (Rosenberg & Handy 2005; Caricchi et al. 2007; Takei & Holtzman 2009; Rey et al. 2009; Rutter et al. 2011), and here we choose the formula provided by Bittner & Schmeling (1995). In summary, we adopt two viscosity laws that depend on the volumetric melt fraction M: if $M < M_S$, the viscosity is equal to μ_{UM} and if $M > M_S$, the viscosity is equal to

μ_{PM} :

$$\tilde{\mu} = \left| \begin{array}{ll} \mu_{UM} = 0.25 \times 10^6 \times (0.75A)^{-\frac{1}{n}} \left[\max(\dot{\varepsilon}_{min}, \dot{\varepsilon})\right]^{\frac{1}{n}-1} \exp(\frac{Q}{nRT}) & \text{if } M < M_S, \\ \mu_{PM} = \sum_{i=1}^{3} C_i \mu_i^0 \text{exp} \left[2.5 + \left(\frac{1-M}{M}\right)^{0.48} (1-M) \right] & \text{if } M \geq M_S, \end{array} \right. \tag{9}$$

where A is a pre-exponential factor ($\mathrm{Pa^{-n}.s^{-1}}$), Q is the activation energy ($\mathrm{J.mol^{-1}}$) and n is the power law exponent, all depending on rock composition. When not stated otherwise, we set $Q = 1.54 \times 10^5$ $\mathrm{J.mol^{-1}}$ and $n = 2.3$. R is the universal gas constant ($R = 8.314$ $\mathrm{J.mol^{-1}.K^{-1}}$), and μ_i^0 is a constant viscosity which also depends on rock composition. Note that, for $n > 1$, the viscosity increases with decreasing strain rate. Because μ_{UM} is unbounded in the limiting case of vanishing strain rate, stagnation points at very large viscosities may occur. Here, we fix a minimal value for the strain rate $\dot{\varepsilon}_{min} = 10^{-16}\mathrm{s^{-1}}$. We verified that this value does not change the results significantly within the range $10^{-16} \leq \dot{\varepsilon}_{min} \leq 10^{-14}$ $\mathrm{s^{-1}}$, in line with Patočka et al. (2019)'s discussion on the effect of an upper viscosity cut-off for Arrhenius type viscosity models using a rigid free-slip top boundary condition (Appendix 4.2).

2.2.4 *Density*

The density explicitly depends on rock composition, melt fraction and temperature. More specifically, the local effective density $\tilde{\rho}$ is defined as $\tilde{\rho} = \rho_{ref} \times [1 - \alpha(T - T_{ref})]$ while ρ_{ref} is computed as:

$$\rho_{ref} = \sum_{i=1}^{3} C_i \times [\rho_i^{S0}(1 - M) + \rho_i^{L0} M], \tag{10}$$

where ρ_i^{S0} and ρ_i^{L0} are the densities of the unmolten and molten rock in fluid i, respectively.

Note that density does not depend on M_S (in contrast to viscosity) and is only controlled by the melt fraction. Therefore, the inclusions may have a density different from that of the BED whatever the value of M, even below M_S. However this has no impact on the system's dynamics since when $M < M_S$, the BED's viscosity remains too high for the inclusions to move, whatever their density.

In the context of felsic orogenic crust, petrological information shows that metamorphism and melting change the bulk density of rock domains by only about 50 to 200 kg/m^3 at the several hundred meters scale encompassed by our heterogeneous inclusions; note that at smaller scale these matrix melt extraction processes are crucial for thermochemical models (e.g. Ganne et al. 2014; Toé et al.

2013). Furthermore, analyses from partially molten felsic rock on field outcrops also display moderate density variations (Bousquet et al. 1997; Hacker et al. 2003).

2.3 Dimensionless equations and dimensionless numbers

In this section, we make equations (1)-(4) dimensionless in order to highlight the three independent dimensionless numbers of the problem. Due to the complex rheology of the fluids considered here, we propose a generalization of the classical dimensionless numbers (e.g. Rayleigh, Prandtl, Archimedes, Rayleigh-Roberts numbers), used in Louis-Napoléon et al. (2020) for instance, to situations where the fluid obeys a non-Newtonian rheology of power-law type.

2.3.1 Dimensionless equations

The local viscosity defined in equation (9) depends on both the local strain rate and temperature (either directly or indirectly via the use of the local melt fraction M). Without loss of generality, viscosity can be thus written in a compact form as :

$$\tilde{\mu} = K_{eff}(T)\dot{\varepsilon}^{\frac{1}{n}-1}, \tag{11}$$

where n is the power-law factor, K_{eff} is a so-called consistency (in $kg/(m.s^{2-1/n})$) which is nothing but the dynamic viscosity when $n = 1$ and $\dot{\varepsilon} = \sqrt{\left(tr(\dot{\epsilon}^2) - tr^2(\dot{\epsilon})/3\right)/2}$ (where $\dot{\epsilon} = (\nabla\mathbf{U} + (\nabla\mathbf{U})^T)/2$ is the strain-rate tensor). Equations (1)-(4) are scaled using a time $\mathcal{T}$, a height $\mathcal{L}$, a velocity $\mathcal{U}$, a pressure $\mathcal{P}$ and a temperature $\mathfrak{T}$ defined as:

$$\mathcal{T} = q^{-1} = \left(\frac{2K_{eff}}{\Delta\rho g H}\right)^n, \quad \mathcal{L} = H, \quad \mathcal{U} = qH, \quad \mathcal{P} = \rho(qH)^2, \quad \mathfrak{T} = \Delta T, \tag{12}$$

where H is the depth of the considered domain, $\Delta\rho$ and ΔT are the characteristic density difference and temperature difference in the system. Note that with the units of K_{eff} in $\mathrm{kg/(m.s^{2-1/n})}$, the term in parenthesis in the expression of $\mathcal{T}$ has units of $\mathrm{s^{1/n}}$, so that $\mathcal{T}$ is in s, whatever the value of n. Here, we choose $\Delta\rho = \rho_1^{S0} - \rho_1^{L0}$ and $\Delta T = T_{liq} - T_{sol}$ since they can be defined *a priori*. Note that the state equation (5) allows us to write $|\Delta\rho/\rho| = |\alpha\Delta T|$, so that we can express the characteristic dimensionless time $\mathcal{T}$ as a function of the temperature difference:

$$\mathcal{T} = q^{-1} = \left(\frac{2K_{eff}}{\Delta\rho g H}\right)^n = \left(\frac{2K_{eff}}{\rho\alpha g\Delta T H}\right)^n. \tag{13}$$

Using the following dimensionless variables (denoted by an asterisk):

$$t^* = \frac{t}{\mathcal{T}}, \quad x_i^* = \frac{x_i}{H}, \quad U^* = \frac{U}{qH}, \quad P^* = \frac{P}{\rho(qH)^2}, \quad g^* = \frac{g}{q^2 H}, \tag{14}$$

equations (1)-(4) can finally be rewritten as:

$$\frac{\partial C_i}{\partial t^*} + \mathbf{U}^* \cdot \nabla^* C_i = -\nabla^* \cdot (\mathbf{U}_r^* C_r), \tag{15}$$

$$\nabla^* \cdot \mathbf{U}^* = 0, \tag{16}$$

$$\frac{\partial \mathbf{U}^*}{\partial t^*} + \mathbf{U}^* \cdot \nabla^* \mathbf{U}^* = -\nabla^* P^* + \mathbf{g}^* + \nabla^* \cdot \left[\frac{2}{Ar}(\nabla^* \mathbf{U}^* + (\nabla^* \mathbf{U}^*)^T)\right], \tag{17}$$

$$\frac{\partial T^*}{\partial t^*} + \mathbf{U}^* \cdot \nabla^* T^* = \frac{2}{Ra} \Delta^* T^* + \frac{2 Ra_H}{Ra^2}, \tag{18}$$

with

$$Ar = \frac{2\rho q^{2-\frac{1}{n}} H^2}{K_{eff}} \quad \text{(generalized Archimedes number)}, \tag{19}$$

$$Ra = \frac{2q}{\kappa / H^2} \quad \text{(generalized Rayleigh number)}, \tag{20}$$

$$Ra_H = \frac{2qH^4 H_r}{\kappa^2 C_p \Delta T} \quad \text{(generalized Rayleigh-Roberts number)}. \tag{21}$$

Note that the Prandtl number is absent from equations (15)-(18), however it can be shown that this number is a function of Ra and Ar, respectively, as:

$$Pr = \frac{Ra}{Ar} = \frac{K_{eff}}{\rho \kappa q^{1-\frac{1}{n}}} \quad \text{(generalized Prandtl number)}. \tag{22}$$

2.3.2 Range of parameters: Natural field versus simulations

Typical values of material properties for a hot orogenic crust are given in Table 1 (Ranalli 1995; Burov & Gerya 2014). These values allow to compute a range of possible $K_{eff} = [K_{eff}^{PM}, K_{eff}^{UM}]$, deduced from Eqs. (9). We estimate :

$$\left| \begin{aligned} K_{eff}^{UM} &= 0.25 \times 10^6 \times (0.75A)^{-\frac{1}{n}} \times exp(\frac{Q}{nRT_{UM}}), \\ K_{eff}^{PM} &= \mu_0 \times exp\left[2.5 + \left(\frac{1 - M_S}{M_S}\right)^{0.48} (1 - M_S)\right]. \end{aligned} \right. \tag{23}$$

where $\overline{T}_{UM}$ is the characteristic mean temperature in the unmolten layer, here computed as $\overline{T}_{UM} = (T_{M_s} + T_{0^o})/2 = (720 + 0)/2 = 360^o$C (as explained in more details in section 3.3).

In order to have a first order estimate of the dimensionless parameters introduced in the previous section, we further assume the characteristic length scale to be $H = 35$ km (the total thickness of the crustal domain is $H_T = H + 10 = 45$ km). This leads to the range of "natural field" parameters given in Table 2.

In the present work, most of the material properties used in the simulations are identical to those in nature, namely the acceleration due to gravity, material densities and their differences, temperatures and their differences, the coefficient of thermal expansion and the thermal diffusivity. In the end, only the height of the system H and the characteristic viscosity (K_{eff}, i.e A or μ_i^0) are different between the real world and the simulations. In particular, we set the value of H and (A, μ_i^0) so as to have $Ar \approx 1$ while being in similarity relative to Ra. This choice significantly reduces computational time. Indeed, Louis-Napoléon et al. (2020) showed that the dynamics of crustal diapirs is correctly reproduced as long as $Ar \lesssim 1$. To illustrate this, the results for various Archimède numbers for one of our main models described below are displayed in Appendix 4.3 . It is important to note that having a larger Ar in the simulations than in nature while keeping the same Ra implies having a smaller Pr in the simulations than in nature (see the last column in Table 2). Nevertheless we verified that Pr was still large enough to be representative of high-Prandtl flows (Krishnamurti 1970).

In practice, we first define the height of the simulation domain. For instance, the ratio between the height of the "natural field" crustal domain, denoted H^{field} and that of the simulation domain, denoted H^{sim} is set to 10^5. This leads to a mesh-element size of 100 m in a 2D mesh of 494×350 cells in total. Knowing the height, the viscosity can then be computed from the ratio between the field and the simulation Archimedes numbers, namely Ar^{field} (for example $Ar^{field} = 10^{-15}$) and $Ar^{sim} = 1$,

Table 1. Typical values of material properties in a hot orogenic crust (Ranalli 1995; Burov & Gerya 2014). The critical melt fraction value is chosen according to Dufek & Bergantz (2005).These values are used in our simulations and lead to the dimensionless parameters provided in Table 3.

Parameter	α	ρ_{S0}	ρ_{L0}	A	Q	n	H_r	μ_0	M_S	T_{sol}	$\kappa(T_{sol})$	$C_p(T_{sol})$
Units	K^{-1}	$\mathrm{kg.m}^{-3}$	$\mathrm{kg.m}^{-3}$	$\mathrm{Pa}^{-\mathrm{n}}.\mathrm{s}^{-1}$	$\mathrm{J.mol}^{-1}$		$\mu\mathrm{W.kg}^{-1}$	Pa.s		K	$\mathrm{m}^2.\mathrm{s}^{-1}$	$\mathrm{m.s}^{-2}.\mathrm{K}^{-1}$
Value	3×10^{-5}	2800	2700	3.2×10^{-4}	1.54×10^5	2.3	1.75	5×10^{15}	0.3	873	6×10^{-7}	1220

Table 2. Range of the dimensionless parameters controlling the present problem (field and simulation values), with input parameters provided in Table 1.

	Time scale	**Archimedes**	**Rayleigh**	**Rayleigh-Roberts**	**Prandtl**
	q^{-1} (years)	$Ar = \frac{2\rho q^{2-\frac{1}{n}} H^2}{K_{eff}}$	$Ra = \frac{2q}{\kappa/H^2}$	$Ra_H = \frac{2qH^4 H_r}{\kappa^2 C_p \Delta T}$	$Pr = \frac{Ra}{Ar}$
Natural field	642	$[10^{-22}; 10^{-15}]$	$[147; 10^5]$	$[10^3; 10^4]$	$[10^{20}; 10^{23}]$
Simulations	–	$[10^{-10}; 10^{-1}]$	$[147; 10^5]$	$[10^3; 10^4]$	$[10^5; 10^{10}]$

respectively:

$$\frac{K_{eff}^{field}}{K_{eff}^{sim}} = \left(\frac{Ar^{field}}{Ar^{sim}}\right)^{-\frac{1}{2n}} \left(\frac{H^{field}}{H^{sim}}\right)^{\frac{2n+1}{2n}} . \tag{24}$$

Using $n = 1$ in (24), we can write $\mu_0^{field}/\mu_0^{sim} = (Ar^{field}/Ar^{sim})^{-1/2}(H^{field}/H^{sim})^{3/2}$, which leads to $\mu_0^{sim} = \mu_0^{field}/10^{15}$. Knowing all the other parameters, we can now relate the time, length and velocity scales in the field to those in the numerical simulation using Eqs. (12).

3 Numerical implementation, method and setup

3.1 The VOF method

We employ the 3D code OpenFOAM (version 4.1 is used here), based on finite volumes with a VOF method, which ensures mass conservation. Domain decomposition and the Message Passing Interface (MPI) library are used to increase the computational speed. It was previously tested for a variety of crustal problems in both 2D and 3D by comparing several Rayleigh-Taylor and Rayleigh-Bénard model results with both analytical solutions and analogue experiments (Louis-Napoléon et al. 2020). The reader is referred to this paper for more details about the numerical code.

3.2 Model Setup

The general model description used for our calculations is illustrated in figure 2. The 50 km $\times 35$ km size model was designed to study fluid dynamics during the melting of an orogenic crust heated internally by radiogenic decay and from below, in a context of removal of the lithospheric mantle, but also perhaps in that of an Archean crust subjected to a higher geothermal gradient. The inclusions of radius 300 m occupy 6 cells, given our choice of grid cell sizes of 100 m as stated above. They are set in staggered rows of inter-distances of three radii (in between vertice centers). Crustal thickness is set constant and equal to 45 km, which might apply to a thickened Phanerozoic orogenic crust but also to the evolution of an Archean craton (Vanderhaeghe et al. 2019; Artemieva & Mooney 2001). The first 10 km are not simulated, because they are much more rigid than the rest of the modeled domain. Instead we assume a rigid free-slip boundary condition at depth 10 km (Fig. 2), a reasonable choice considering that convection below a stagnant lid is little affected by the lid's rather elastic deformation (e.g. Patočka et al. 2019). The initial thermal structure of the crust corresponds to a linear temperature profile of 300°C at 10 km depth and 600°C at 45 km depth (at the bottom of the crust). The velocity boundary conditions are set free slip at the upper boundary and no slip at the bottom boundary. Left and right velocity and thermal boundaries are set periodic. Note that as shown for instance by Patočka et al. (2019), the use of periodic lateral border boundary conditions allows to eliminate the locking of convection cells, which may appear if impermeable free-slip borders were used instead. At the onset of the model ($t = 0^+$), the temperature at the base of the crust is instantaneously increased from $T_H = 600$ °C to $T_{H+} = 1000$ °C and is kept constant to this latter value during all the computation; this simulates the effect of thinning of the lithospheric mantle as a result of either mantle delamination or slab retreat beneath the orogenic crust (Royden 1996; Vanderhaeghe & Duchêne 2010). No lateral motion is applied to the model (periodic slip along lateral boundaries). The rheology of the crust is assumed to be controled by a dominantly quartzitic composition, hence the power-law creep parameters of quartz are chosen (Ranalli 1995), as specified in Table A1.

In addition, the numerical models simulate partial melting by i) decreasing the density with increasing melt fraction, ii) decreasing the effective viscosity when the volumetric melt fraction $M > M_S$, and iii) accounting for variations in thermal diffusion and heat capacity according to equations (6) and (7) above. The volumetric melt fraction increases linearly with temperature according to (8). Density, viscosity and melting relationships are employed for all three fluid phases, with specific physical parameters for each phases. Other processes associated with partial melting such as sub-scale solid-melt segregation processes (porous scale modes of fluid percolation). However, note that the approximation of heterogeneous inclusions implicitly accounts for the fact that rocks with different compositions might have distinct density and viscosity evolutions with temperature, which induces heterogeneous behaviour in the system.

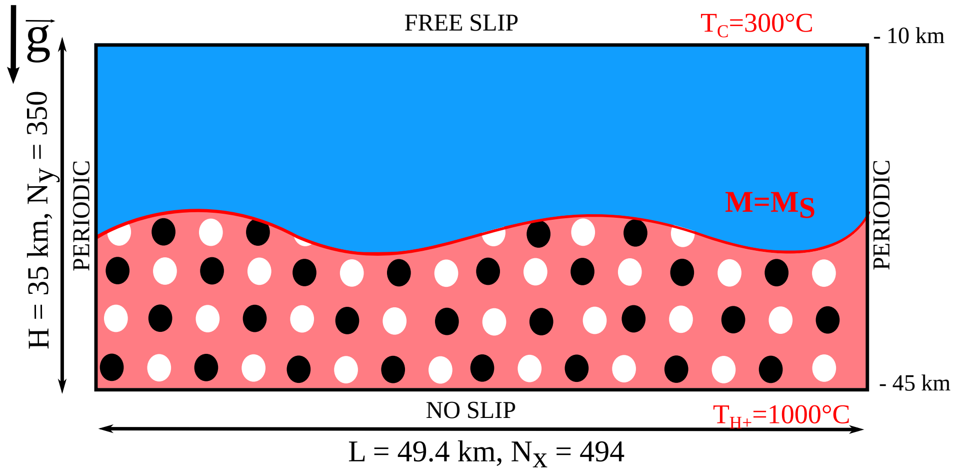

Figure 2. Numerical setup : domain size, grid size, and boundary conditions (see text for details). The melting front ($M = M_S$) forms initially at the base of the model domain due to the imposition of the thermal boundary condition, and it activates the black and white inclusions as it migrates progressively upwards over time.

Our model setting involves non-negligible density variations over the several tens of kilometers over which the inclusions travel. Whether they are submitted to significant local expansion and contraction due to hydrostatic pressure variations during motion is recalled in appendix 4.4.

3.3 Dimensional numbers in the unmolten and partially molten layer

In the presence of a melting front, the domain can be divided in two regions occupied by the unmolten and the partially molten media, respectively. Because of their different rheologies, it appears reasonable to define two Rayleigh numbers denoted Ra_{UM} and Ra_{PM} for these unmolten and partially molten domains, respectively. The choice of a representative thickness for each of these domains is not straight-forward given the fact that they evolve in space in a complementary way one with respect to the other. Hence, for both Rayleigh numbers we assume an equal value corresponding to half of the physical domain's total height ($H_T = 45$ km), $H_T/2$. Besides, one can estimate the characteristic variation in temperature for each of these domains, which are separated by the melting front temperature T_{M_s}. This temperature can be deduced from the choice of M_s and other values (cf. Table 1); here, $T_{(M_s=0.3)} = 720^o$C. Hence, we define for Ra_{UM}, $\Delta T_{UM} = T_{M_s} - T_{0^o}$, where temperature spans from the Earth's surface to that of the melting front. For Ra_{PM}, we define $\Delta T_{PM} = T_{1000^o} - T_{M_s}$ spanning from the melting front temperature to the maximum temperature at the base of the model domain. Consequently, using Eq. (13) and replacing H by $H_T/2$ and ΔT by either ΔT_{UM} or ΔT_{PM} in Eq. (20), Ra_{UM} and Ra_{PM} are defined as:

$$Ra_{UM} = \frac{H_T^2}{2\kappa_{UM}} \left(\frac{\rho\alpha g \Delta T_{UM} H_T}{4K_{eff}^{UM}} \right)^n, \qquad Ra_{PM} = \frac{\rho\alpha g \Delta T_{PM} (H_T/2)^3}{\kappa_{PM} K_{eff}^{PM}}, \tag{25}$$

where K_{eff}^{UM} and K_{eff}^{PM} are defined in Eq. (23) while κ_{UM} and κ_{PM} are the thermal diffusivities computed with the characteristic mean temperature in each layer, namely $\kappa_{UM} = \kappa((T_{M_s} + T_{0^o})/2)$ and $\kappa_{PM} = \kappa((T_{M_s} + T_{1000^o})/2)$, respectively. Note that for Ra_{PM}, $n = 1$ hence it no longer appears in its definition. Values of Ra_{UM} and Ra_{PM} are given for each model case in Tables A1 and 3.

4 Numerical Results

First we identify the behavior of the system with partial melting alone, without compositional heterogeneities. This allows to compare the evolution of the melting front with previous studies, and to describe the various regimes of the flow dynamics. When compositional heterogeneities are inserted in a second step, in the next section, our results reveal similar main flow regimes.

4.1 Convection with partial melting alone

First, a reference case is presented, with which the main flow characteristics are described. Then a flow regimes diagram is proposed. A complementary parametric study is provided in Appendix 1.

4.1.1 Reference case

The reference case is named $I_0 M_1 H_0$ and its input parameters are provided in Table A1. Figure 3 presents the temporal evolution of the system's main variables, e.g. horizontally averaged temperature and viscosity, position of the melting front and average vertical velocity . We observe at first a diffusive stage in Figure 3a between $t = 0$ and $t = 2.4$ Myr (red star). Then from 2.4 to 4.0 Myr, a first convective stage develops (blue star). The melting front deforms with a wavelength $\lambda_{conv} \sim 10$ km. Convection cells first lengthen in the vertical dimension but maintain a constant width, and then, they merge to form cells of wavelength $\lambda_{conv} \sim 25$ km (green star). From 10.1 Myr, the convection cells merge again to form a large convection cell with a height to width ratio of almost $1 : 1$ (purple star).

Finally, the melting front stabilizes around depth 15.5 km. Recall that the temperature at the top is imposed, which impedes further upward migration of the melting front.

Figure 3e shows the time evolution of the mean absolute vertical velocity $|Uy|$ of the system. Each change in thermal regime (or convective stage) is accompanied by a velocity jump until the last convective stage is reached. In this last stage, the mean vertical velocity becomes roughly constant and is denoted $|Uy|_f$. This mean velocity can be compared to the theoretical value estimated by Kraichnan (1962) and validated by Shibano et al. (2013) based on laboratory experiments. This prediction assumes constant kinematic viscosity (ν) and thermal diffusion (κ), and is expressed by:

$$|Uy|_{theo} = 2 \left(\frac{\alpha g \Delta T \kappa^2}{\nu} \right)^{1/3} . \tag{26}$$

We apply this formula to the stabilized system once the cells sizes reach a 1:1 ratio. The average temperature of the convective layer below the melting front is $T_{avg} \approx 884^o$C, which gives $\kappa(884^o\mathrm{C}) = 5.7 \times 10^{-7}\ \mathrm{m}^2.\mathrm{s}^{-1}$ and $\nu(884^o\mathrm{C}) = 2.9 \times 10^{13}\ m^2.s^{-1}$ (from Equations (6), (7) and (9)). With $\alpha = 3 \times 10^{-5}\ \mathrm{K}^{-1}$, $g = 9.81\ \mathrm{m.s}^{-2}$ and $\Delta T = T_H^+ - T_{avg}$, we obtain $|Uy_{theo}| \approx 4.7\ \mathrm{cm.yr}^{-1}$, which is relatively close to our numerically measured value $|Uy|_f \approx 5\ \mathrm{cm.yr}^{-1}$. This slight difference between the theoretical velocity and the modeled velocity might be due to our choice of the position of the melting front, as the upper bound of the thickness of the convective layer.

The melting front's average depth evolution is displayed Fig. 3a. It is found proportional to $\sim t^{0.5}$ in the diffusive stage, and proportional to $\sim t$ in the first and second convective stages. This characteristic behaviour is qualitatively consistent with the results of Favier et al. (2019); convection of the melting domain evolves in different stages accompanied by velocity jumps, until the flow stabilizes into a unique convection cell of ratio almost 1:1.

Vasil & Proctor (2011) showed that in a system with a moving melting front, the critical Rayleigh number Ra_c above which convection occurs is modified compared to the classical Rayleigh-Bénard problem ; a morphological mode grows as soon as $Ra_{PM}(1 - M_S) \left(\frac{h_c}{H} \right)^3 > Ra_c \sim 1295.78$. This relationship can be rewritten to express the theoretical thickness required for the onset of convection : $h_c = H \times \left(\frac{Ra_c}{Ra_{PM}(1 - M_S)} \right)^{1/3}$. Here $Ra^{PM} \approx 4 \times 10^5$, $M_S = 0.3$ and $H = 35$ km, which provides $h_c^{theo} \sim 6.6$ km. This value is close to the one observed in our simulations, where $h_c \approx 8$ km at the end of the diffusive stage (h_c is the distance over which the melting front traveled, Fig. 3).

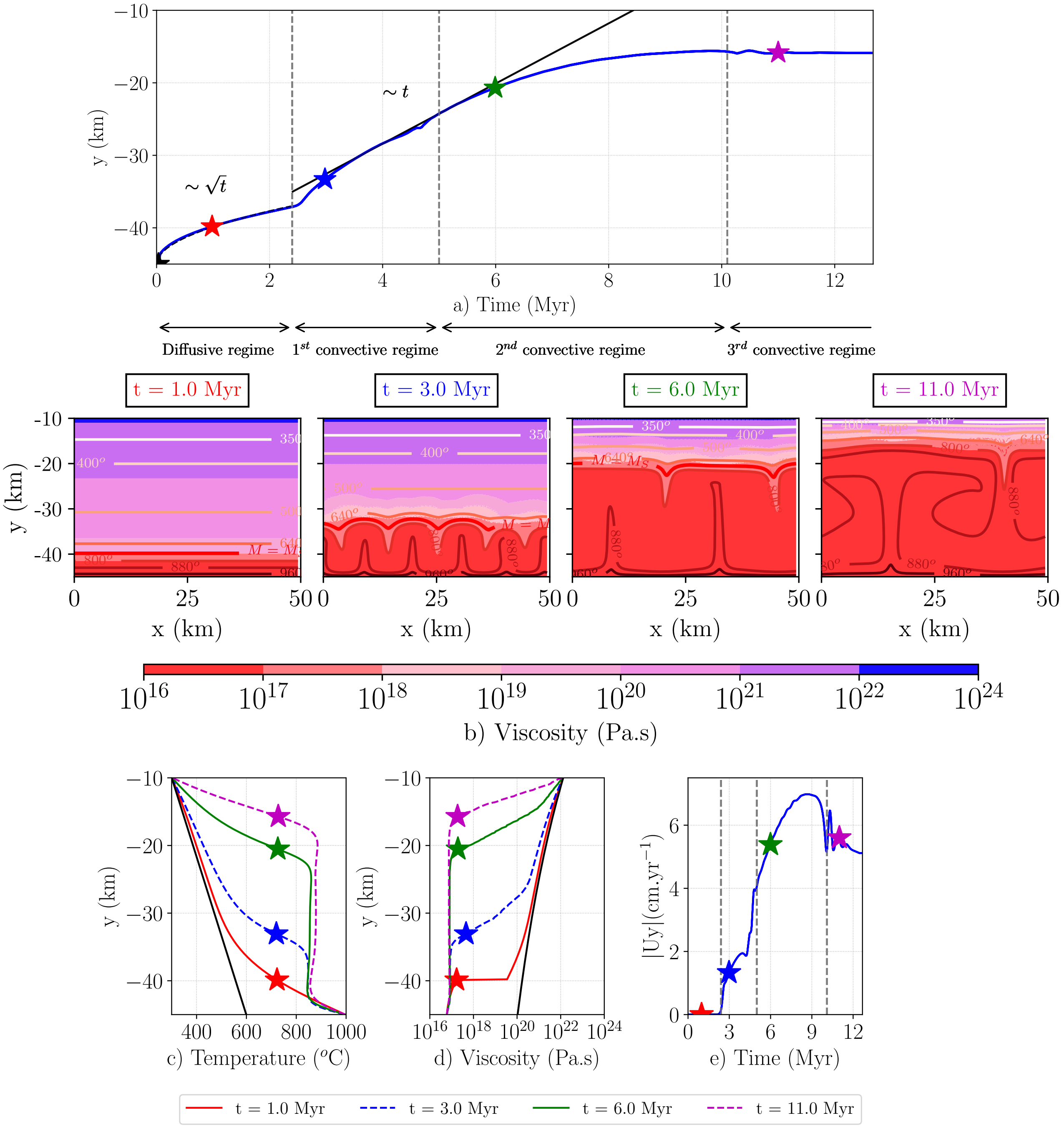

Figure 3. Case $I_0M_1H_0$ (cf. Table A2 for parameters). a) time evolution of the melting front. Stars locate the snapshots in b). b) snapshots at different times: distribution of viscosity, isotherms (in Celsius degree) and melting front (thick red line). c-d) vertical profile of the horizontally-averaged temperature and viscosity, respectively (stars indicate melting front location). e) time evolution of the mean vertical velocity.

Now we analyze this configuration in terms of the temporal evolution of cycles and convection cells. Therefore, three passive markers are placed in the model and record local characteristics over time (Fig. 4). These markers might be assimilated to the zircons studied by Vanderhaeghe et al. (2018) in Naxos's migmatite domes, and constitute a key argument for crustal scale convection (a more detailed comparison will be developed in paper part II). The markers periods (τ) associated to the convective cycles range between 0.2 and 0.5 Myr for the three markers on display. The markers velocity norm over time (Fig. 4a) displays four plateaus corresponding to the four flow stages described above with the mean velocity $|Uy|$. The markers positions (Fig. 4b, upper panel) illustrate the change in convective regime with time, from rather elongated convective cells of size $l \times h \approx 5 \times 15$ km during the first convective stage (blue curve), to 5×26 km during the second stage (purple curve), and large cells of size 25×20 km (cyan curve) in the last stage. Within one convective stage, low velocities correspond to horizontal displacements occurring at the upper and lower limits of the convective cells, whereas high velocities correspond to vertical displacements at the lateral borders of the convective cells. Note also that the red marker records lower velocities than the blue marker, because of its location nearer to the center of a cell than at its edges.

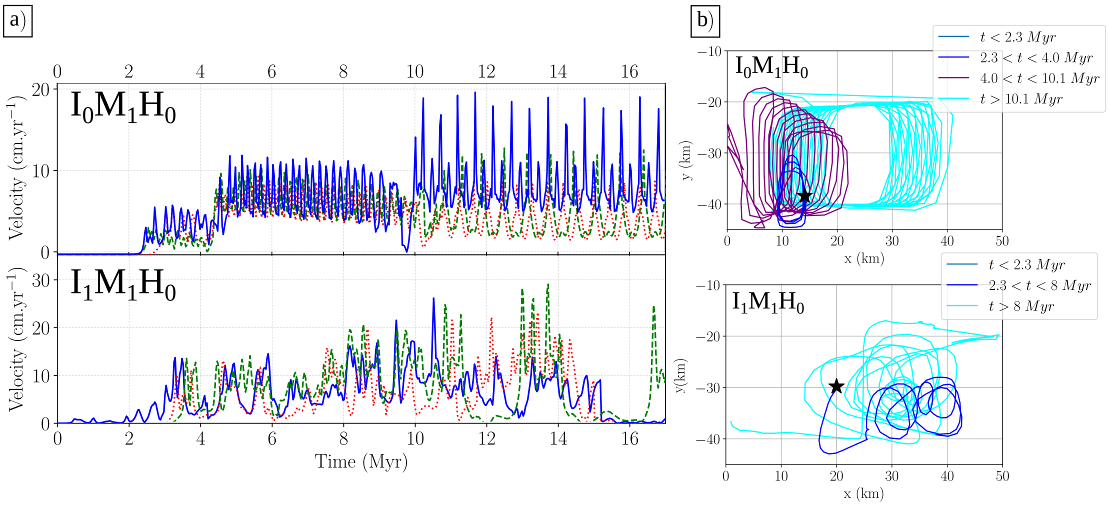

Figure 4. a) Temporal evolution of the position and velocity of markers for two model cases. In case $I_0M_1H_0$ (upper panel), they are initially located at $(x,y) = (14.1,-38.4)$, $(31.2,-34.8)$, $(34.4,-42)$ km, respectively for the blue, red and green curves. In case $I_1M_1H_0$ (lower panel), they are initially located at $(x,y) = (34.4,-42)$, $(31.2,-34.8)$, $(20.0,-29.8)$ km, respectively for the blue, red and green curves. b) Location of a marker over time. The star locates its initial position at $(x,y) = (14.1,-38.4)$ km (in case $I_0M_1H_0$) and $(x,y) = (20.0,-29.8)$ km (in case $I_1M_1H_0$).

4.1.2 Flow regimes with melting alone and without heterogeneities

In the reference model described above, we obtained four stages of flow evolution that evolve during the chosen 20 Myr of total model time. Recall that this time window is defined arbitrarily considering that, except for a few examples, the duration of Phanerozoic orogenies is on the order of a few tens of Myr. Accordingly, this choice of 20 Myr allows to capture the time scale over which gravitational instabilities may dominate over other forcing boundary conditions associated to plate tectonics. When modifying various input parameters, model cases evolve towards a variety of flow regimes that we describe below. Figure 5 summarizes these three flow regimes in the parameter space (Ra_{UM}, Ra_{PM}) (computed *a priori* using Eq. 25), with melting alone (i.e. without heterogeneities) :

- **a) No convection :** $Ra_{PM} \lesssim 2.10^3$ **-** The Rayleigh number of the partially molten layer Ra_{PM} is too low to allow for convection, and the thermal regime remains diffusive.

- **b) Global convection :** $Ra_{PM} \gtrsim 2.10^3$ **and** $Ra_{UM} \gtrsim 10$ **-** Here, both the Rayleigh numbers of the unmolten medium and partially molten medium are sufficiently high to allow for the medium to convect at depths greater than the melting front. In the final convection stage, the thickness of the partially molten layer reaches a constant value equal to the entire domain thickness (from depth 45 km) minus the thickness of the upper cold and unmolten lid (at depth 15 km, approximately). Although after 20 Myr the final convection stage is identical for all model cases in this regime, during the first convection regime the cell sizes may differ.

- **c) 'Confined' convection :** $Ra_{PM} \gtrsim 2.10^3$ **and** $Ra_{UM} \lesssim 10$ **-** When the Rayleigh number of the partially molten domain is high and that of the unmolten domain is low, the melting front stagnates at a deeper depth. Thus, the thickness of the partially molten zone is smaller and the convection cells still cannot merge after 20 Myr. They eventually would after a much longer time, since this regime tends to evolve towards the global convection regime. This point is further discussed in section **5**. Note that the model's aspect ratio does not influence these cells width (illustrated in Appendix 4.1). It is useful to distinguish this regime here, because the development and duration of either narrow or broad convection cells appears a key control on the formation of migmatite domes at the base of the upper crust.

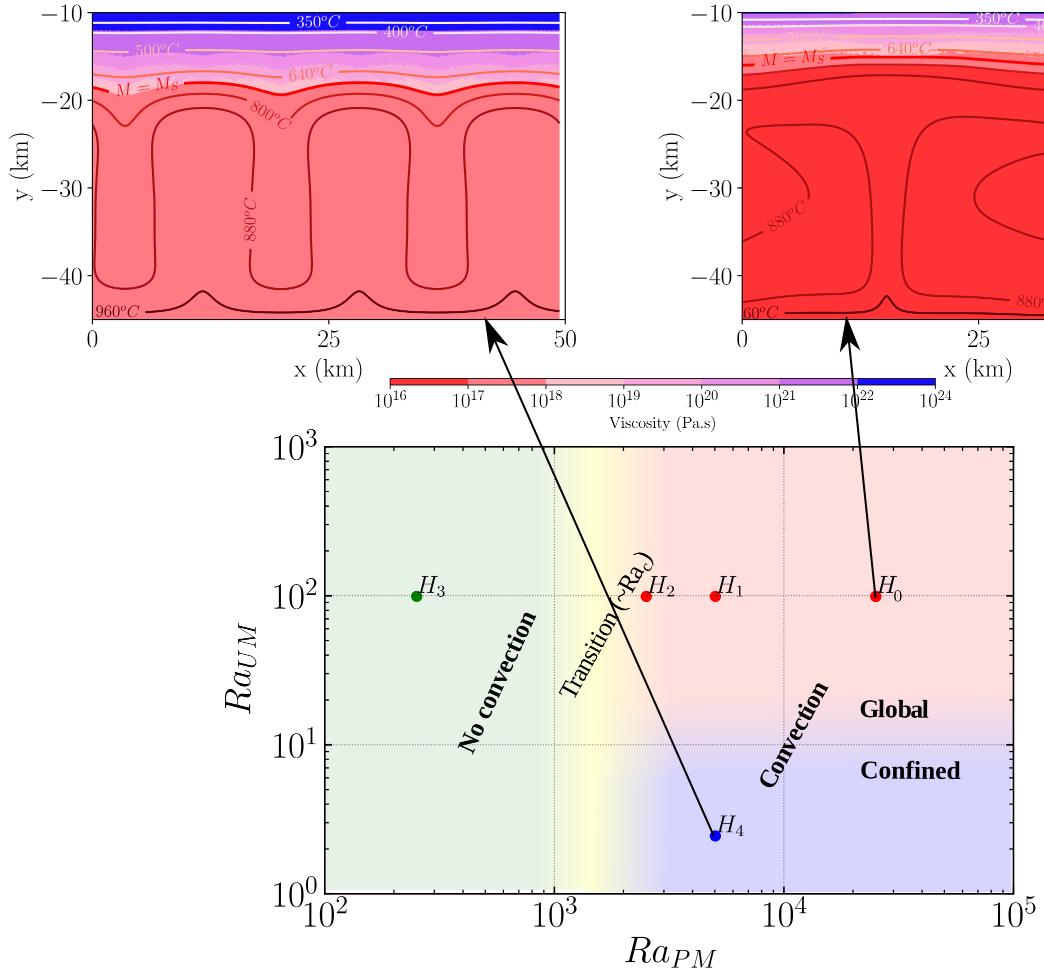

Figure 5. Convective regimes diagram with melting alone, as a function of the Rayleigh numbers Ra_{UM} and Ra_{PM} defined in the layers above and below the melting front, respectively (see text for details). Three regimes are identified, after 20 Myr of applied basal heating: the diffusive regime (no convection) at small Ra_{PM} ($< 2 \times 10^3$), the global convective regime at high Ra_{PM} ($> 2 \times 10^3$) and high Ra_{UM} (> 10), in which a single convective cell reaches the maximum size of about 30 km, and the local convective regime, at small Ra_{UM} (< 10), in which the convective regime stabilizes into several vertically elongated cells of width 15 km and height 25 km. These two convection regimes are illustrated with their viscosity and isotherms distributions.

4.2 Convection with partial melting and heterogeneities

In this section, we study the influence of rheological heterogeneities in a model setting that is otherwise similar to the setting described above without heterogeneities. As in the previous section, we first describe a reference model, with various evolution stages. Then we illustrate the influence of a range of parameters on the observed flow regimes.

4.2.1 Reference case

The reference model $I_1M_1H_0$ has the same initial and rheological parameters as those of the reference model without heterogeneities (section 4.1, $I_0M_1H_0$) except that it contains inclusions. These inclusions are distributed throughout the domain as shown Fig. 2, section 3.2 (see Table 3 for details).

The different flow stages with time are illustrated in Fig. 6. First at $t \leq 2.3$ Myr, the diffusive stage occurs (the average velocity is zero). It is characterized by the upward propagation of the melting front as a straight line, at a speed proportional to the square root of time. Meanwhile, the inclusions that are located under the melting front segregate: the light inclusions rise while the heavy ones sink. However, note that they are also entrained within the convective flow. While some heavy inclusions settle onto the domain's base as soon as 2.1 Myr, the light inclusions still 'mix' in the flow at 20 Myr.

From $2.3 \leq t \leq 8$ Myr, a first convective stage develops to form convection cells of size ~ 15 km, between 45 and 30 km depth (the position of the melting front evolves linearly with time). After $t \geq 8$ Myr, these cells merge to form convective cells 50 km wide (second convective stage), between 45 and 15 km depth. Note that the transition between convective stages (or regimes) is not marked by a sharp jump in the mean velocity, which contrasts with the reference model without heterogeneities (Fig. 3e).

Let us make a brief comparison between the two reference cases of partial melting without and with inclusions, respectively named $I_0M_1H_0$ (Fig. 3) and $I_1M_1H_0$ (Fig. 6). The diffusive stage is identical in both cases: the presence of inclusions does not impact heat diffusion. The transition between the diffusive and the convective stages occurs in both cases around $\sim 2.5 - 3$ Myr, although it is less abrupt in the case with inclusions. This means that the critical Rayleigh number is the same in both cases. In the first convective stage ($t \lesssim 5$ Myr), five cells form in the case without inclusions whereas three form in the case with inclusions. In the last convection stage ($t \gtrsim 10$ Myr), the melting front stabilizes at a depth of 19 km in the case with inclusions, against 15.5 km in the case without inclusions. In addition, the convective layer thickness is smaller in the case with inclusions because the black inclusions have formed a viscous layer between depths 45 and 40 km. Note that the heavy inclusions settle preferentially below upwellings (Fig. 6b, from 10 Myr), in line with the findings of Patočka et al. (2020).

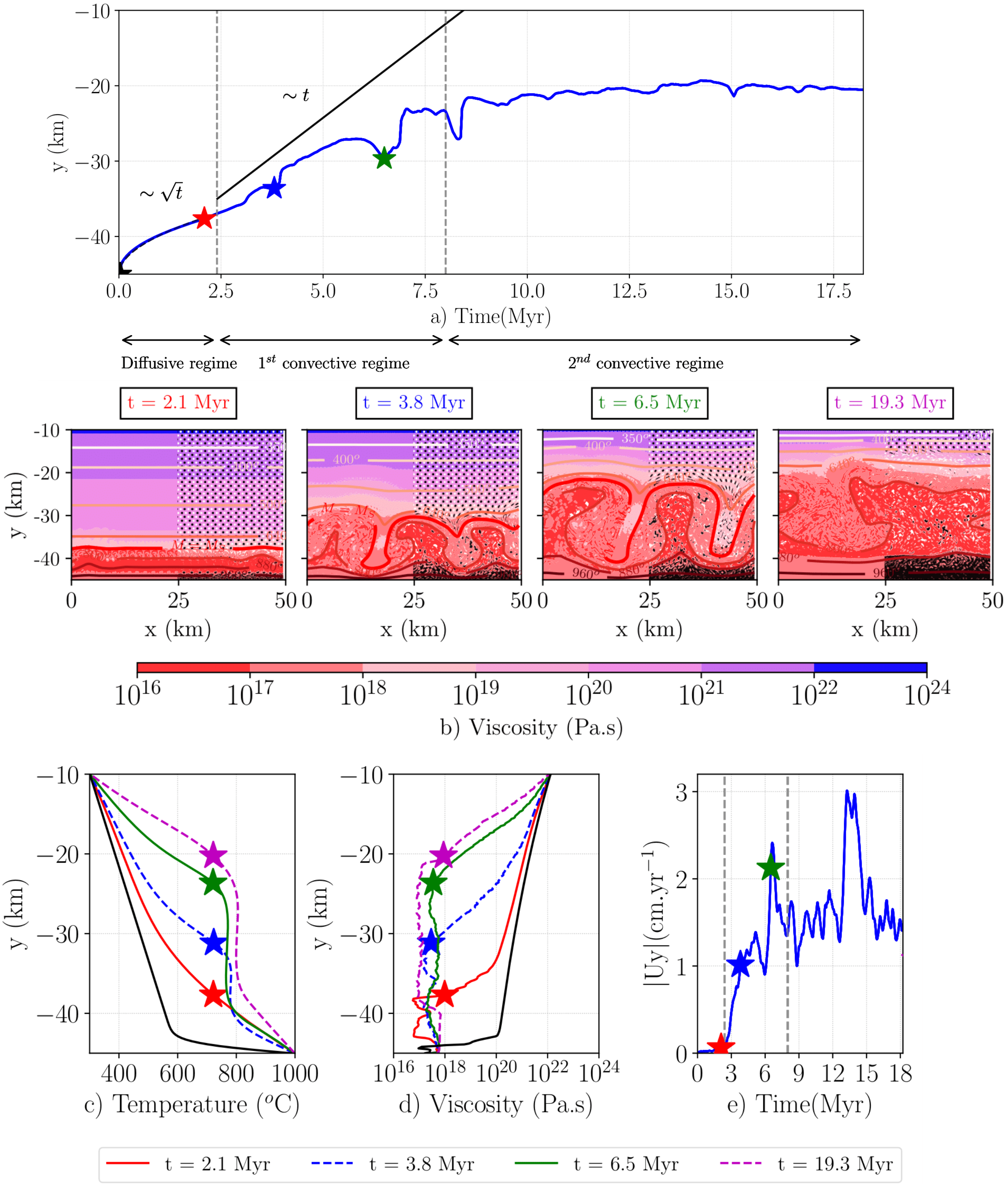

Figure 6. Case $I_1M_1H_0$ (cf. Table 3 for parameters). a) time evolution of the melting front. Stars locate the snapshots in b). b) snapshots at different times: distribution of viscosity, isotherms (in Celsius degrees) and melting front (thick red line). On the right half of the model domain, light and heavy inclusions are plotted in white and black, respectively. c-d) vertical profile of the horizontally-averaged temperature and viscosity, respectively (stars indicate melting front location). e) time evolution of the mean vertical velocity.

The mean vertical velocities are two to three times lower in the case with inclusions ($1.8\ \mathrm{cm.yr}^{-1}$ against $5\ \mathrm{cm.yr}^{-1}$) which shows that their presence has the consequence of reducing the average convection velocity (and its maximum and minimum values). In addition, the inclusions presence slightly increases the period of the convective cycles (1 Myr against 0.5 Myr without inclusions). These observations are illustrated in Fig. 4 which presents the dynamics of three markers initially placed at depth $y < -30\ \mathrm{km}$. They display a convective period of the order of a million years, with ascent rates of the order of $1 - 5\ \mathrm{cm.yr}^{-1}$.

4.2.2 Flow regimes in a crust with compositional heterogeneities

Various simulations with partial melting and heterogeneities were performed to identify flow regimes in the parameter space (Ra_{UM}, Ra_{PM}), defined in Eq. (25). The obtained flow regimes are summarized in Table 3 and displayed Fig. 7.

In most cases, we can describe these flow regimes with respect to three typical domains: i) a floating lid of lighter inclusions located at the top of the convection cells, ii) a bulk fluid domain (the BED) containing suspending inclusions in the core of the convection cells, and iii) a layer of heavier inclusions deposited at the base of the convection cells. More specifically, the fate of the inclusions varies with the flow regimes, dividing the parameter space in four regions:

a) No motion - When $Ra_{PM} \lesssim 2 \times 10^2$, convection is absent (purely diffusive regime) and the viscosity in the unmolten and partially molten media is so high that no significant motion occurs within the simulated time window of 20 Myr.

b) Diapirism - When $2 \times 10^2 \lesssim Ra_{PM} \lesssim 4 \times 10^3$ and $Ra_{UM} \lesssim 10$, convection is still absent, however, the viscosity in the BED domain is low enough so that the inclusions can move by more than one radius during the 20 Myr period considered here, thanks to Archimedes's buoyancy force. This basic segregation mode leads to upward motion of the light inclusions, which end up floating at the top of the partially molten layer and form a layer (layer i). At the same time, the heavy inclusions sink on to the domain's base (layer iii). In between these layers, the BED domain becomes empty of inclusions and remains in a diffusive thermal regime (layer ii).

Table 3. Physical parameters of the runs performed with partial melting and inclusions. Note that v_s is the Stokes velocity of the inclusions, here defined as $v_s = \frac{2}{9}\frac{|\rho_{i\neq 1}-\rho_1|gr^2}{K_{eff}^{PM}}$ with $K_{eff}^{PM} \approx 35\mu_1^0$ (see eq. 23). Some of the simulations names are associated with a link to the corresponding movie.

Case	i	Viscosity μ_i^0 Pa.s	Density ρ_i^{L0} kg.m^{-3}	Heat source H_r μW.kg^{-1}	Incl. radius r m	Incl. thickness h km	Prefactor A Pa^{-n}.s^{-1}	Ra_{UM}	Ra_{PM}	v_s mm.yr^{-1}
$I_1M_1H_0$	1	5×10^{15}	2700	1.75	300	35	3.2×10^{-4}	100	3×10^{4}	
	2	5×10^{14}	2600	2						3.6
(reference)	3	5×10^{16}	2900	0.9						7.2
$I_1M_1H_1$	1	2.5×10^{16}	2700	1.75	300	35	3.2×10^{-4}	100	6×10^{3}	
	2	2.5×10^{15}	2600	2						0.7
	3	2.5×10^{17}	2900	0.9						1.4
$I_1M_1H_2$	1	5×10^{16}	2700	1.75	300	35	3.2×10^{-4}	100	3×10^{3}	
	2	5×10^{15}	2600	2						0.35
	3	5×10^{17}	2900	0.9						0.7
$I_1M_1H_3$	1	2.5×10^{16}	2700	1.75	300	35	3.2×10^{-4}	100	6×10^{3}	
	2	2.5×10^{15}	2500	2						1.4
	3	2.5×10^{17}	2900	0.9						1.4
$I_1M_1H_4$	1	2.5×10^{16}	2700	1.75	300	35	3.2×10^{-4}	100	6×10^{3}	
	2	2.5×10^{15}	2500	10						1.4
	3	2.5×10^{17}	2900	0.9						1.4
$I_1M_1H_5$	1	2.5×10^{16}	2700	1.75	300	7	3.2×10^{-4}	100	6×10^{3}	
	2	2.5×10^{15}	2500	10						1.4
	3	2.5×10^{17}	2900	0.9						1.4
$I_1M_1H_6$	1	2.5×10^{16}	2700	1.75	600	35	3.2×10^{-4}	100	6×10^{3}	
	2	2.5×10^{15}	2500	10						5.6
	3	2.5×10^{17}	2900	0.9						5.6
$I_1M_1H_7$	1	2.5×10^{16}	2700	1.75	300	35	7.8×10^{-6}	2.4	6×10^{3}	
	2	2.5×10^{15}	2500	10						1.4
	3	2.5×10^{17}	2900	0.9						1.4
$I_1M_1H_8$	1	2.5×10^{16}	2700	1.75	300	35	3.2×10^{-4}	100	6×10^{3}	
	2	2.5×10^{14}	2600	10						0.7
	3	2.5×10^{18}	2900	0.9						1.4
$I_1M_1H_9$	1	2.5×10^{16}	2700	1.75	300	35	3.2×10^{-4}	100	6×10^{3}	
	2	2.5×10^{13}	2600	10						0.7
	3	2.5×10^{19}	2900	0.9						1.4
$I_1M_1H_{10}$	1	2.5×10^{16}	2700	1.75	300	50	3.2×10^{-4}	100	6×10^{3}	
	2	2.5×10^{15}	2500	10						1.4
	3	2.5×10^{17}	2900	0.9						1.4
$I_1M_1H_{11}$	1	2.5×10^{16}	2700	1.75	900	35	3.2×10^{-4}	100	6×10^{3}	
	2	2.5×10^{15}	2500	10						12.6
	3	2.5×10^{17}	2900	0.9						12.6
$I_1M_1H_{12}$	1	2.5×10^{16}	2700	1.75	150	35	3.2×10^{-4}	100	6×10^{3}	
	2	2.5×10^{15}	2500	10						0.35
	3	2.5×10^{17}	2900	0.9						0.35
$I_1M_1H_{13}$	1	2.5×10^{16}	2700	1.75	$300 \leq r \leq 1800$	35	3.2×10^{-4}	100	6×10^{3}	
	2	2.5×10^{15}	2500	10						-
	3	2.5×10^{17}	2900	0.9						-
$I_1M_1H_{15}$	1	2.5×10^{16}	2700	1.75	Layer 7	35	3.2×10^{-4}	100	6×10^{3}	
	2	2.5×10^{15}	2500	10						-
	3	2.5×10^{17}	2900	0.9						-
$I_1M_1H_{16}$	1	2.5×10^{16}	2700	1.75	1200	35	3.2×10^{-4}	100	6×10^{3}	
	2	2.5×10^{15}	2500	10						22.4
	3	2.5×10^{17}	2900	0.9						22.4
$I_1M_1H_{17}$	1	2.5×10^{16}	2700	1.75	300	35	1.6×10^{-4}	50	6×10^{3}	
	2	2.5×10^{15}	2500	10						1.4
	3	2.5×10^{17}	2900	0.9						1.4
$I_1M_1H_{18}$	1	2.5×10^{16}	2700	1.75	300	35	3.2×10^{-6}	1	6×10^{3}	
	2	2.5×10^{15}	2500	10						1.4
	3	2.5×10^{17}	2900	0.9						1.4
$I_1M_1H_{19}$	1	5×10^{16}	2700	1.75	300	35	7.8×10^{-6}	2.4	3×10^{3}	
	2	5×10^{15}	2500	10						0.7
	3	5×10^{17}	2900	0.9						0.7

Case	i	Viscosity μ_i^0 $Pa.s$	Density ρ_i^{L0} $kg.m^{-3}$	Heat source H_r $\mu W.kg^{-1}$	Incl. radius r m	Incl. thickness h km	Prefactor A $Pa^{-n}.s^{-1}$	Ra_{UM}	Ra_{PM}	v_s $mm.yr^{-1}$
$I_1M_1H_{20}$	1	2.5×10^{17}	2700	1.75	300	35	7.8×10^{-6}	2.4	6×10^{2}	
	2	2.5×10^{16}	2500	10						0.14
	3	2.5×10^{18}	2900	0.9						0.14
$I_1M_1H_{21}$	1	2.5×10^{16}	2700	1.75	300	35	7.9×10^{-5}	25	6×10^{3}	
	2	2.5×10^{15}	2500	10						1.4
	3	2.5×10^{17}	2900	0.9						1.4
$I_1M_1H_{22}$	1	5×10^{18}	2700	1.75	300	35	3.2×10^{-4}	100	30	
	2	5×10^{17}	2500	10						0.007
	3	5×10^{18}	2900	0.9						0.007
$I_1M_1H_{23}$	1	2.5×10^{17}	2700	1.75	300	35	3.2×10^{-4}	100	6×10^{2}	
	2	2.5×10^{16}	2500	10						0.14
	3	2.5×10^{18}	2900	0.9						0.14
$I_1M_1H_{24}$	1	5×10^{17}	2700	1.75	300	35	3.2×10^{-4}	100	3×10^{2}	
	2	5×10^{16}	2500	10						0.073
	3	5×10^{18}	2900	0.9						0.073
$I_1M_1H_{26}$	1	2.7×10^{18}	2700	1.75	300	35	3.2×10^{-4}	100	55	
	2	2.7×10^{17}	2500	10						0.013
	3	2.7×10^{19}	2900	0.9						0.013
$I_1M_1H_{27}$	1	1.6×10^{18}	2700	1.75	300	35	3.2×10^{-4}	100	95	
	2	1.6×10^{17}	2500	10						0.022
	3	1.6×10^{19}	2900	0.9						0.022
$I_1M_1H_{28}$	1	2.5×10^{16}	2700	1.75	300	35	4.2×10^{-5}	13	6×10^{3}	
	2	2.5×10^{15}	2500	10						1.4
	3	2.5×10^{17}	2900	0.9						1.4
$I_1M_1H_{29}$	1	2.5×10^{16}	2700	1.75	300	35	2.5×10^{-5}	7.8	6×10^{3}	
	2	2.5×10^{15}	2500	10						1.4
	3	2.5×10^{17}	2900	0.9						1.4
$I_1M_1H_{30}$	1	2.5×10^{17}	2700	1.75	300	35	4.2×10^{-5}	13	6×10^{2}	
	2	2.5×10^{16}	2500	10						0.14
	3	2.5×10^{18}	2900	0.9						0.14

c) Convection and layering - Here, $Ra_{PM} \gtrsim 4\times10^3$ and $Ra_{UM} \lesssim 10$. In the same way as in the case without inclusions, a small Ra_{UM} describes a medium of moderate viscosity in which convection occurs but is not vigorous. In this regime, the light inclusions can extract from the convection cells and segregate; they stack below the rigid upper lid so as to form a thicklayer (layer i). The heavy inclusions in turn sink on the domain's base (layer iii) as in the previous regime.

d) Convection and suspension - Here, $Ra_{PM} \gtrsim 2\times10^2$ and $Ra_{UM} \gtrsim 10$. This regime behaves similar to the reference case $I_1M_1H_0$. The intermediate BED layer (ii) convects vigorously and hosts the majority of the light and heavy inclusions. The activated light inclusions are dragged into the convecting BED layer (ii) after some time (which varies depending on parameters). They cannot aggregate below the rigid upper crust (absence of layer i). Some heavy inclusions are dragged into the convection but the majority still settle down on the domain's base (layer iii), in a proportion that depends on parameters, further discussed section **5**.

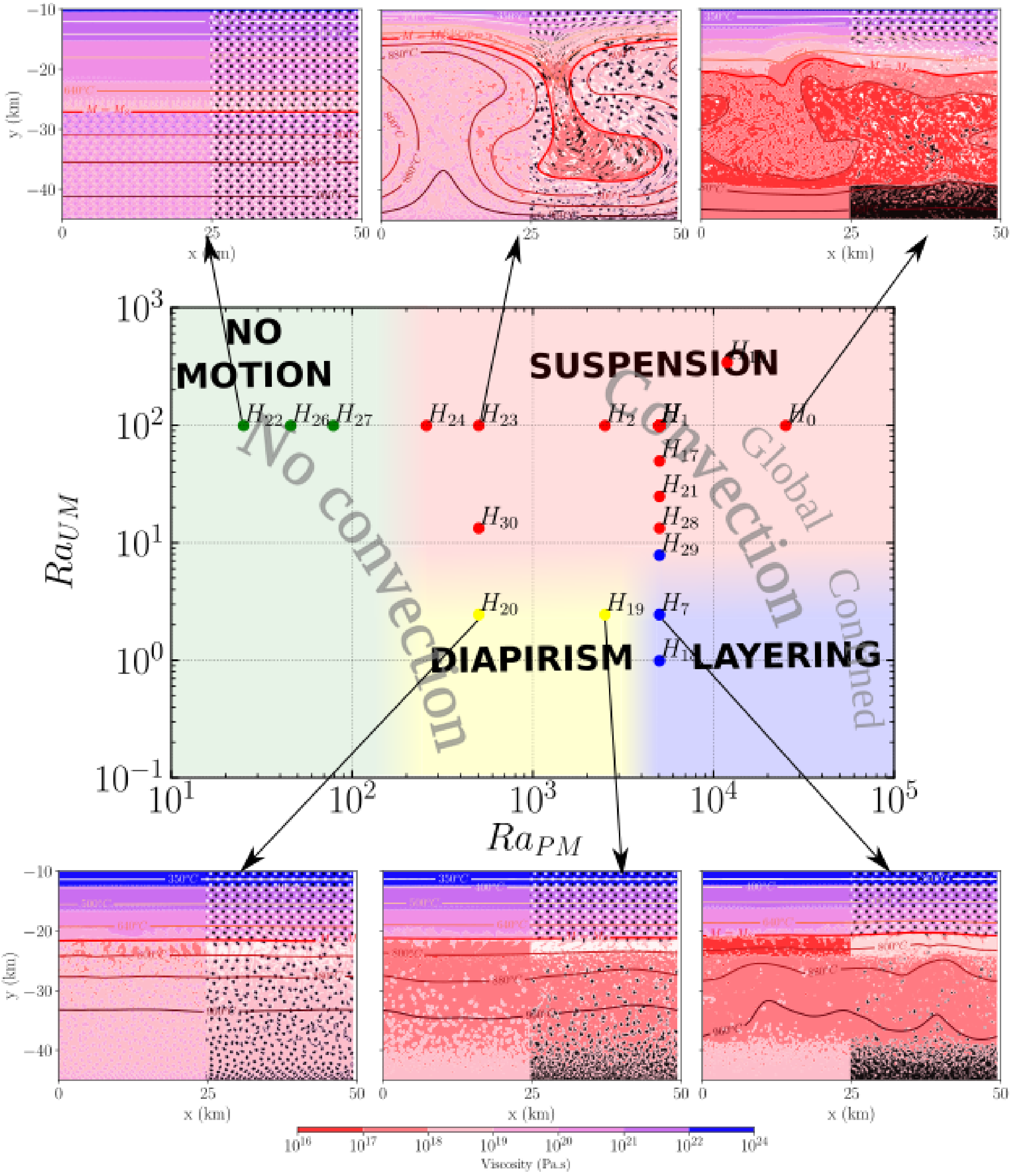

Figure 7. Flow regimes diagram for a hot orogenic crust that is melting and contains heterogeneous inclusions, as a function of Rayleigh numbers Ra_{UM} and Ra_{PM} above and below the melting front, respectively. Here, $Ra_{UM} = \frac{2H_T^2}{4\kappa}\left(\frac{\rho\alpha g\Delta T_{UM}H_T}{4K_{eff}^{UM}}\right)^n$ and $Ra_{PM} = \frac{\rho\alpha g\Delta T_{PM}(H_T/2)^3}{\kappa K_{eff}^{PM}}$ with K_{eff}^{UM} and K_{eff}^{PM} defined in (23). Each regime is illustrated with a snapshot at time $t \sim 20$ Myr presenting the isotherms, the viscosity distribution in the left half of the model domain, and the light (white) and heavy (black) inclusions in its right half.

Let us describe the tests from the regimes diagram depicted Fig. 7. For these model cases and for the case $I_1M_1H_1$, Fig. 8 displays snapshots of the material properties and Fig. 9 displays the mean velocity of the material phases (the BED, the light and heavy inclusions). The mean vertical velocity of phase i is computed as $|Uy|(t) = \int_\vartheta C_i(\mathbf{x},t)|u_y(\mathbf{x},t)|d\vartheta / \int_\vartheta C_i(\mathbf{x},t)d\vartheta$, where ϑ is the volume of the computational domain, C_i is the volume fraction of phase i and u_y is the local vertical velocity.

The three top cases of Fig. 8 are located in the ”suspension” region of the regimes diagram. Next cases illustrate the ”no motion” and the ”diapirism” regions, and the last case, the ”layering” region:

- Case $I_1M_1H_0$ (red curve) has the greatest convection vigor. Here, the light inclusions display similar velocities to those of the BED (greater than 1.5 cm.yr^{-1} at long times) as they are entrained in the convective flow. In turn, the heavy inclusions deposit early on, before convection initiates time $t \leq 2.5$ Myr and at a vertical velocity ≈ 7 mm.yr^{-1}, of the same order of magnitude as their Stokes velocity (see Table 3 and the corresponding animation). Then, they keep depositing as indicated by their slow but persistent decrease in velocity $|Uy|$. This is in line with the fact that all our models lie in the so-called ’dust-like’ regime defined by Patočka et al. (2020), where an increasing portion of the inclusions settle while the other portion remains in suspension (see Appendix 5 for a comparison of our models with others considering the settling of rigid particles in Rayleigh-Bénard convection).
- The same behaviour is observed for cases $I_1M_1H_1$ and $I_1M_1H_{23}$ (purple and pink curves, respectively). The main difference is that since the viscosity in the BED is increased in these cases, the settling velocity of both the light and heavy inclusions is reduced (see e.g. their v_s in Table 3). Consequently, at a similar moment, the thickness of the heavy inclusions layer is smaller when Ra_{PM} is decreased, as clearly observed in Fig. 8. Overall, cases $I_1M_1H_{0,1,2,23}$ belong to the same regime, here named *suspension* (Verhoeven & Schmalzl (2009) named it the C-regime) despite the fact that an increasing number of heavy inclusions deposit while some remain in suspension. The difference seen in the snapshots of Fig. 8 for different model cases relates to identical time moments being illustrated whereas the inclusions Stokes velocity and the convection vigor differ. In fact, Fig. 8 qualitatively shows that at a given moment, the sediment layer thickness is larger when Ra_{PM} is increased.
- A striking difference between case $I_1M_1H_7$ (blue curve) and those mentioned above ($I_1M_1H_{0,1,23}$) is that two sediment layers of heavy and light inclusions develop, whereas only one layer of heavy inclusions was observed before. This is confirmed by the mean vertical velocity of the light material approaching 0 after ca. 15 Myr. Note that convection remains active in case $I_1M_1H_7$ since the mean vertical velocity of the BED never reaches zero during the simulation, which justifies to define a *layering* regime that differs from the *suspension* and *diapirism* regimes. The fact that layering of the

light inclusions is not observed in case $I_1M_1H_0$ even though both cases have a similar Ra_{PM} calls for another criterion that distinguishes these behaviors. The main difference between these two cases then appears in the viscosity of the unmolten region being much larger in case $I_1M_1H_7$ than in case $I_1M_1H_0$. Also, the density difference between the light inclusions and the BED is two times larger in case $I_1M_1H_7$ than in case $I_1M_1H_0$, hence their Stokes velocity is larger in case $I_1M_1H_7$. Both differences favor the accumulation of light inclusions below the upper crust lid.

The main difference between our *suspension* regime and our *layering* regime can be summarized as follows. While convection occurs in both cases, the light inclusions in the *suspension* regime cannot form a stagnant layer because the local velocity remains large in the region *near* the melting front where they could stack, in contrast with the situation of the heavy inclusions, where the bottom boundary is fixed and remains a low-velocity boundary layer. In this *suspension* regime, the actual low-velocity region (i.e. the boundary layer) is located *above* the melting front, as seen in the upper right panel in Fig. 7 (the light pink region above the melting front of thickness c.a. 4 km - with a viscosity in the range $10^{18} - 10^{19}$ Pa.s - hosts strongly deformed light inclusions). This result is coherent with a relatively small viscosity of the unmolten ambient rock (corresponding to a larger Ra_{UM}). In contrast, in the *layering* regime, the viscosity of the unmolten layer above the melting front is large enough to mimic a rigid lid: the viscosity gradient above the melting front is sharper (cf. bottom right panel in Fig. 7, the light purple region where the $10^{19} - 10^{20}$ Pa.s viscosity range lies just above the melting front and is only 1 km thick), and the low-velocity boundary layer remains *below* the melting front (indicated by the undeformed inclusions located above the melting front). Thus, the layering of light inclusions is favored, in a way similar to the heavy inclusions.

- As for cases $I_1M_1H_{19}$, $I_1M_1H_{20}$ and $I_1M_1H_{22}$ (orange, yellow and green curves, respectively), no convection is observed and the mean velocity in the BED is less than 1 mm.yr^{-1}. However, the inclusions Stokes velocity is quite different in between cases $I_1M_1H_{19,20}$ ($v_s = 0.14 - 0.7$ mm.y^{-1}) and case $I_1M_1H_{22}$ ($v_s = 0.007$ mm.y^{-1}). In the first cases, the distance traveled by the inclusions during 20 Myr is of the order of 5 to 15 km (i.e. several tens of the inclusions radius), while in the second case the traveled distance is less than 150 m (i.e. half an inclusion radius). Consequently, a criterion allowing to distinguish between the *no motion* regime and the *diapirism* regime could be the ratio of the distance covered by the inclusions during the modeled time (here 20 My) to the size of the inclusions. When this ratio is less than one, we may reasonably consider that there is no motion.

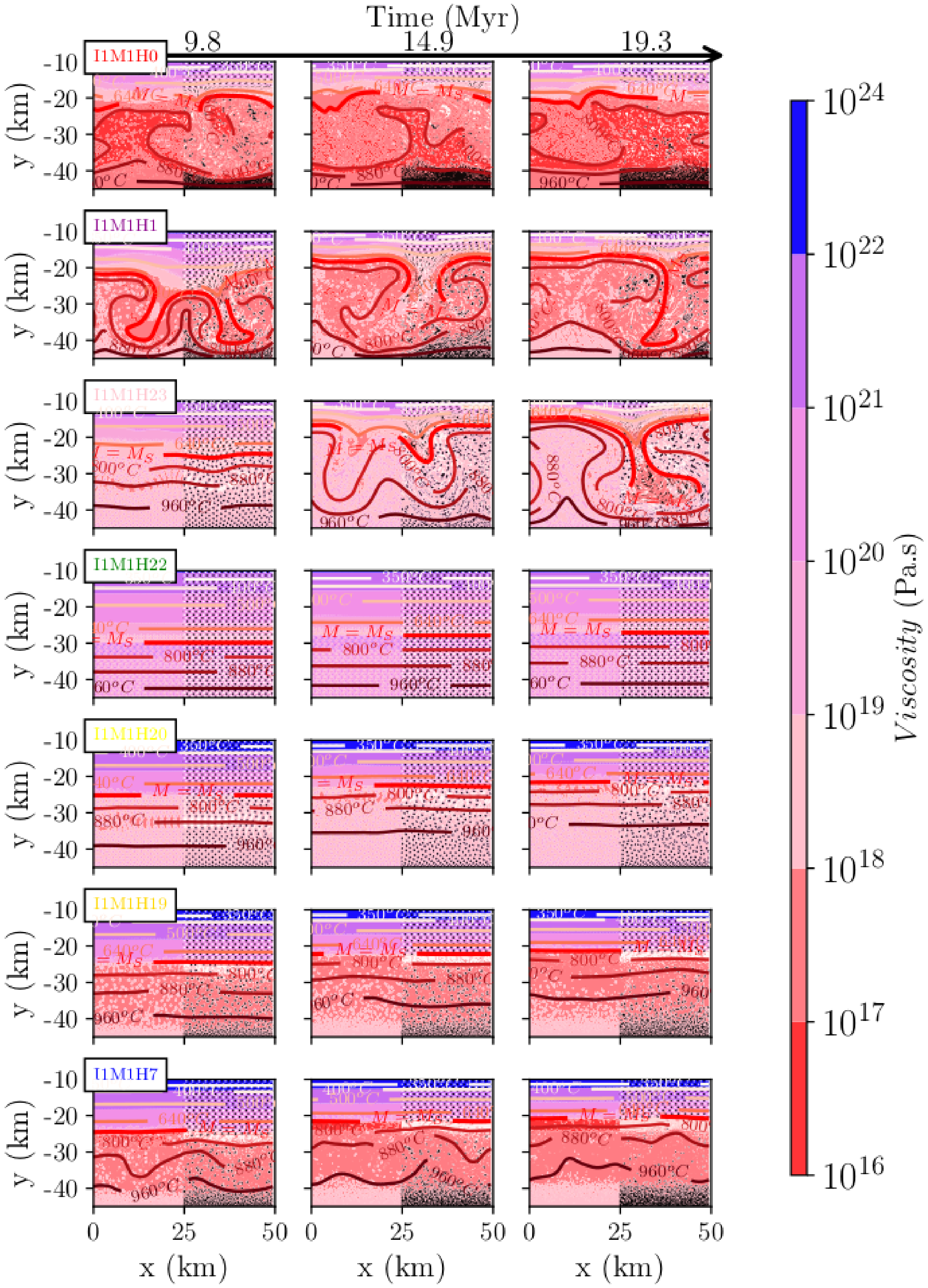

Figure 8. Snapshots at three moments for the cases displayed in Fig. 7 (plus case $I_1M_1H_1$): to the left half of the model domain, the viscosity distribution, temperature isocontours and, to the right, the light and heavy inclusions in white and black. Note that the distributions for the last two moments are roughly similar.

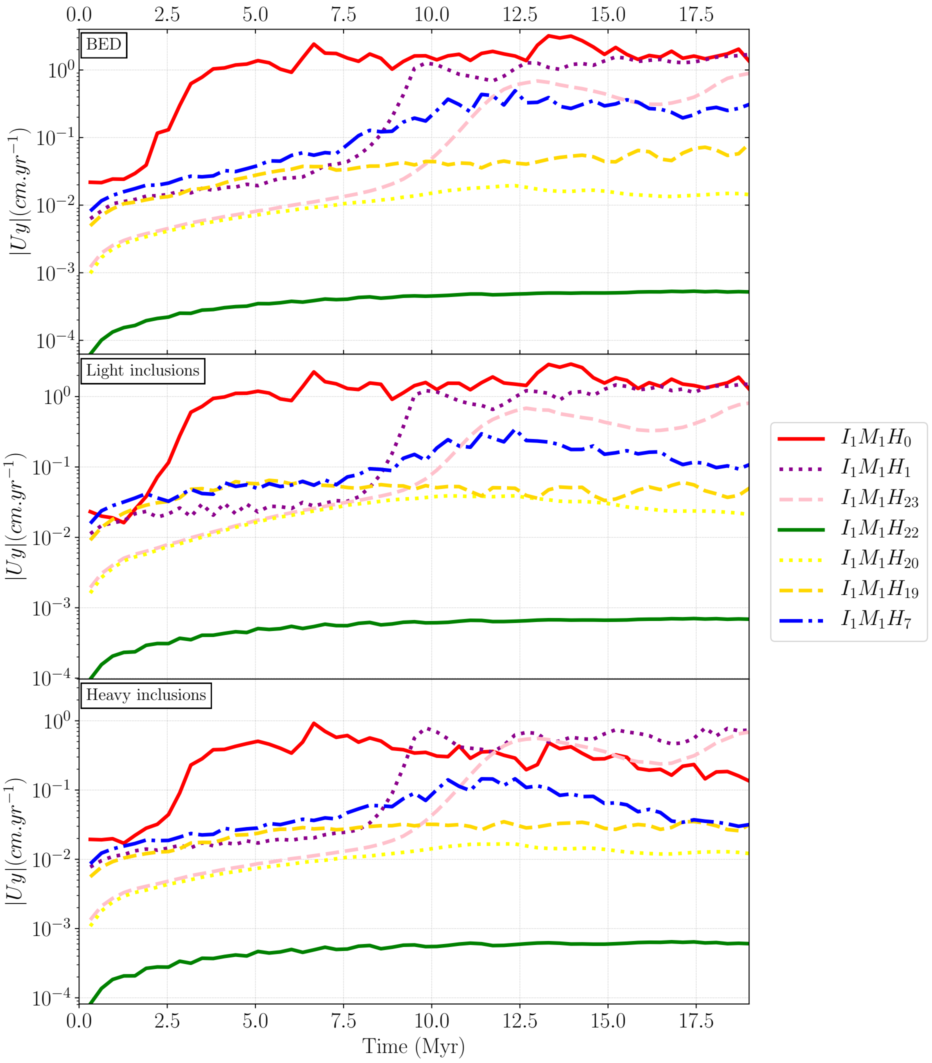

Figure 9. Temporal evolution of the mean vertical velocities for each material phases for the cases shown in Fig. 7 (each in a different color and with the addition of case $I_1M_1H_1$): from top to bottom, $|U_y|$ for the BED, the light inclusions and the heavy inclusions.

In Fig. 10, we evaluate the settling rate of the heavy and light inclusions, by tracking the evolution of their relative concentration over time. More specifically, we compute the depth at which these inclusions have a concentration Φ_i of more than 60 or 70% ($\sim$ 2 times their initial concentration) with $\Phi_i(y,t) = \int_{x=0}^{x=L_x} C_i(\mathbf{x},t)dx$ and $i = 2$ and 3 for the light and heavy inclusions, respectively. For high Ra_{PM} at least, the settling rate does not reach a steady state after 20 Myr, a result in agreement with the characteristically long residence time of our inclusions with respect to the simulation time duration, as commented in Appendix 5. In addition, the rate of sedimentation decreases as Ra_{PM}

decreases, in agreement with Martin & Nokes (1988)'s theory. Indeed, these authors found that it is proportional to the Stokes velocity v_s, which decreases with decreasing Ra_{PM} (see frame c). Finally, this figure shows that a layer of light inclusions can form and be maintained in the layering regime ($Ra_{UM} = 99$), in contrast to the suspension regime ($Ra_{UM} = 0.16$, frames a and b).

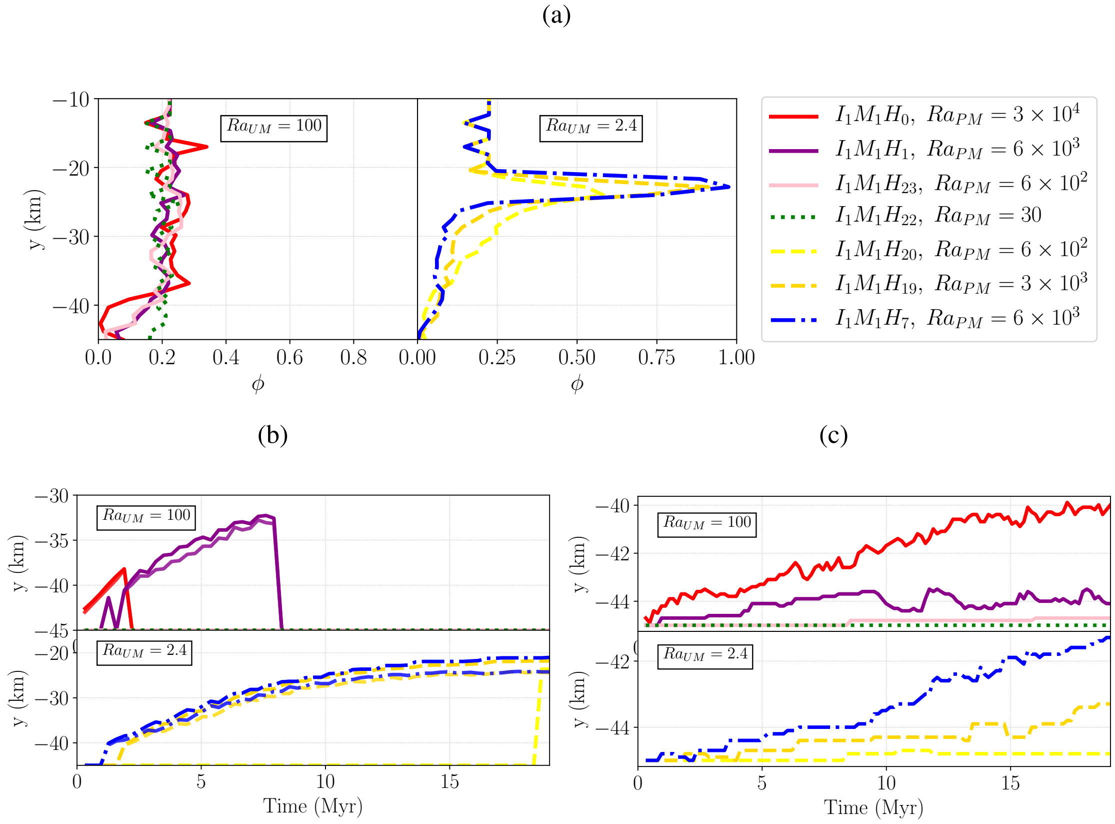
(a)

(b)

(c)

Figure 10. (a) Vertical profile of the horizontally-averaged concentration Φ_2 of the light inclusions at time $\sim$ 20 Myr for various cases in the 'suspension' and in the 'diapirism/layering' regimes ($Ra_{UM} = 100$ vs. $Ra_{UM} = 0.16$) with $\Phi_2(y,t) = \int_{x=0}^{x=L_x} C_2(\mathbf{x},t)dx$. With initial $\Phi_2 = 0.17$, models belonging to the suspension regime on the left, display values lower than 0.3. The models belonging to the 'layering' regime in turn, on the right, display values greater than 0.3 over a thickness of about 5 km located below depth 20 km. (b-c) Temporal evolution of the vertical location of the layer of *light* inclusions (b) and *heavy* inclusions (c), defined as the depth at which these inclusions have a concentration $\Phi_2 > 60\%$ and $\Phi_3 > 70\%$, respectively.

The phenomenological results described above remain valid for the following range of parameters, as shown in (Louis-Napoléon 2020, PhD thesis) :

- the partially molten BED viscosity (Eq. 9): $5 \times 10^{15} \leq \mu_1^0 \leq 5 \times 10^{17}$ Pa.s,
- the unmolten BED viscosity A (Eq. 9) : $1.6 \times 10^{-6} \leq A \leq 3.2 \times 10^{-4}$ Pa$^{-2.3}$.s^{-1},

- the light inclusions density : $2500 \leq \rho_2^{L0} \leq 2600$ kg.m^{-3},
- the radioactive heat rate : $0 \leq H_r \leq 10$ μW.kg^{-1}.

Overall, the flow dynamics of the inclusions can be schematized according to the diagram depicted Fig. 11, as a function of Ra_{UM} and Ra_{PM}. This supports the idea that these dimensionless numbers are key controlling parameters of the dynamics of crustal systems.

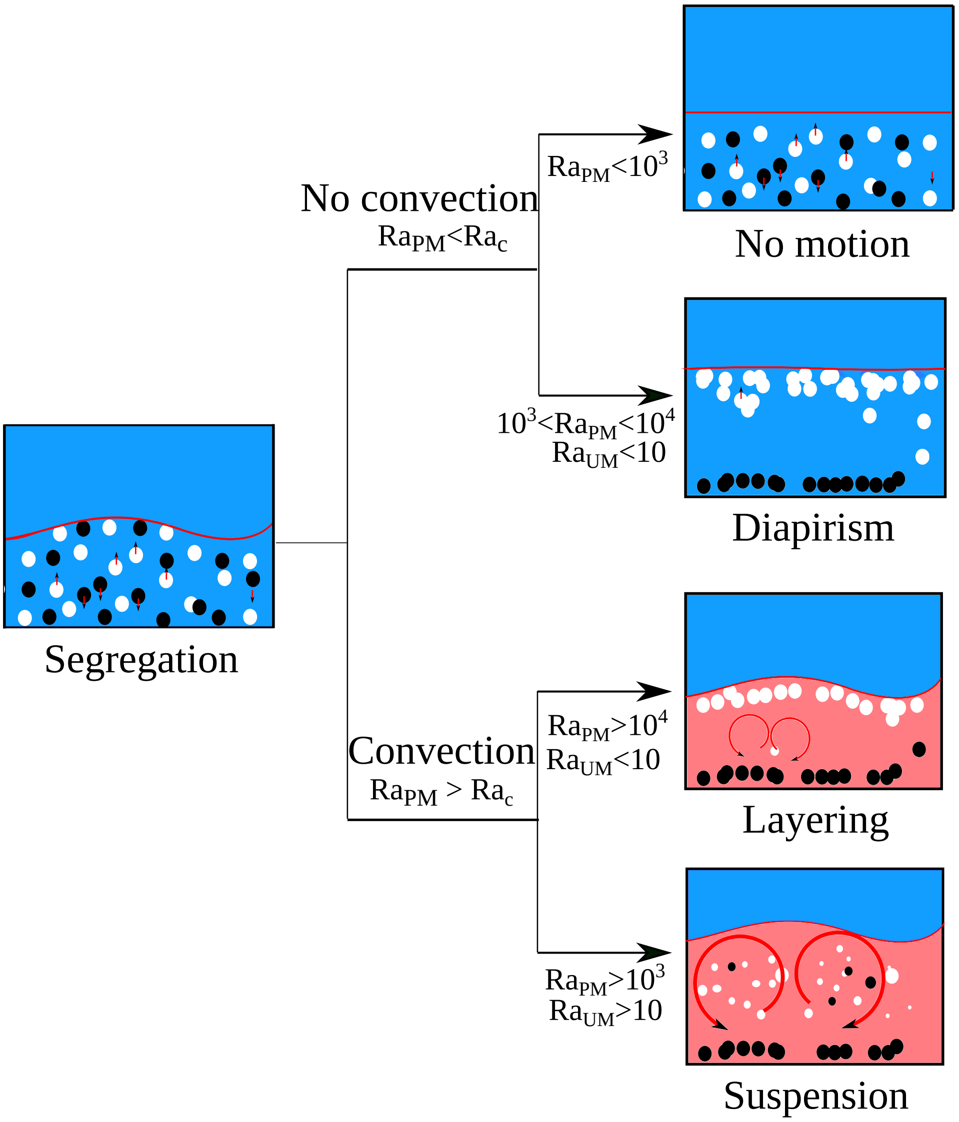

Figure 11. Synthesis of the various flow regimes which can be observed in a crust at steady state, heated from below and containing heterogeneous inclusions, as a function of the Rayleigh numbers Ra_{UM} of the unmolten layer and Ra_{PM} of the partially molten layer (Eqs. (25)). Ra_c is the critical value above which convection starts (see text for details).

4.2.3 Influence of the size and arrangement of the inclusions in the suspension regime

Now, we illustrate the influence of variations in the radius of the inclusions, in the range $150 \leq r \leq 1200$ m (five cases $I_1M_1H_{4;6;11;12;16}$). Other parameters are those of the reference case ($I_1M_1H_0$, belonging to the *suspension* regime). We also test a case in which the inclusions radius is set randomly between $150 \leq r \leq 1800$ m, and another one in which the initial arrangement is set random ($I_1M_1H_{13}$). In the last test case ($I_1M_1H_{15}$), the compositional heterogeneities are initially set in a horizontal layer 7 km thick, and the light layer is located under the heavy layer (similar to case 2 of Weinberg & Schmeling 1992).

The results are displayed in Fig. 12 and reveal interesting distinct behaviours depending on the size of the inclusions. When r is increased, the inclusions have a larger buoyancy and are able to rise and deform in a region located *above* the melting front, in contrast with the smaller inclusions. Such a behavior is visible for $r \geq 600$ m at time $t = 2.7$ Myr in the layer located in between isotherms $T = 640^o$C and $T = 720^o$C (for which $M = M_S$). The rise of the large inclusions above the melting front induces a decrease in the local viscosity (down to ca. $\sim 10^{18}$ Pa.s), due to a thermal strain–softening effect (Graham & England 1976; Kincaid & Silver 1996; Molnar & England 1990). As viscosity is decreased, convection is enhanced, as shown by the isotherms displayed at time $t = 5.1$ Myr and which are more 'wavy' when the size of the inclusions is increased.

We also remark that for small inclusions ($r \leq 600$ m), the inclusions tend to coalesce, forming pockets of maximum size 2 km which are entrained into the convective cells. In turn when $r \geq 600$ m, the inclusions deform and disintegrate into smaller size structures as they are dragged into the convective cells. Overall, thermal convection is triggered before the light structures manage to reach a shallow depth and freeze. In other words, in the suspension regime, convection always ends up destroying any kind of aggregation (or clustering) of light inclusions, regardless of their size. This reorganisation of the inclusions sizes independantly from their initial size will be further studied in paper part II for the other flow regimes.

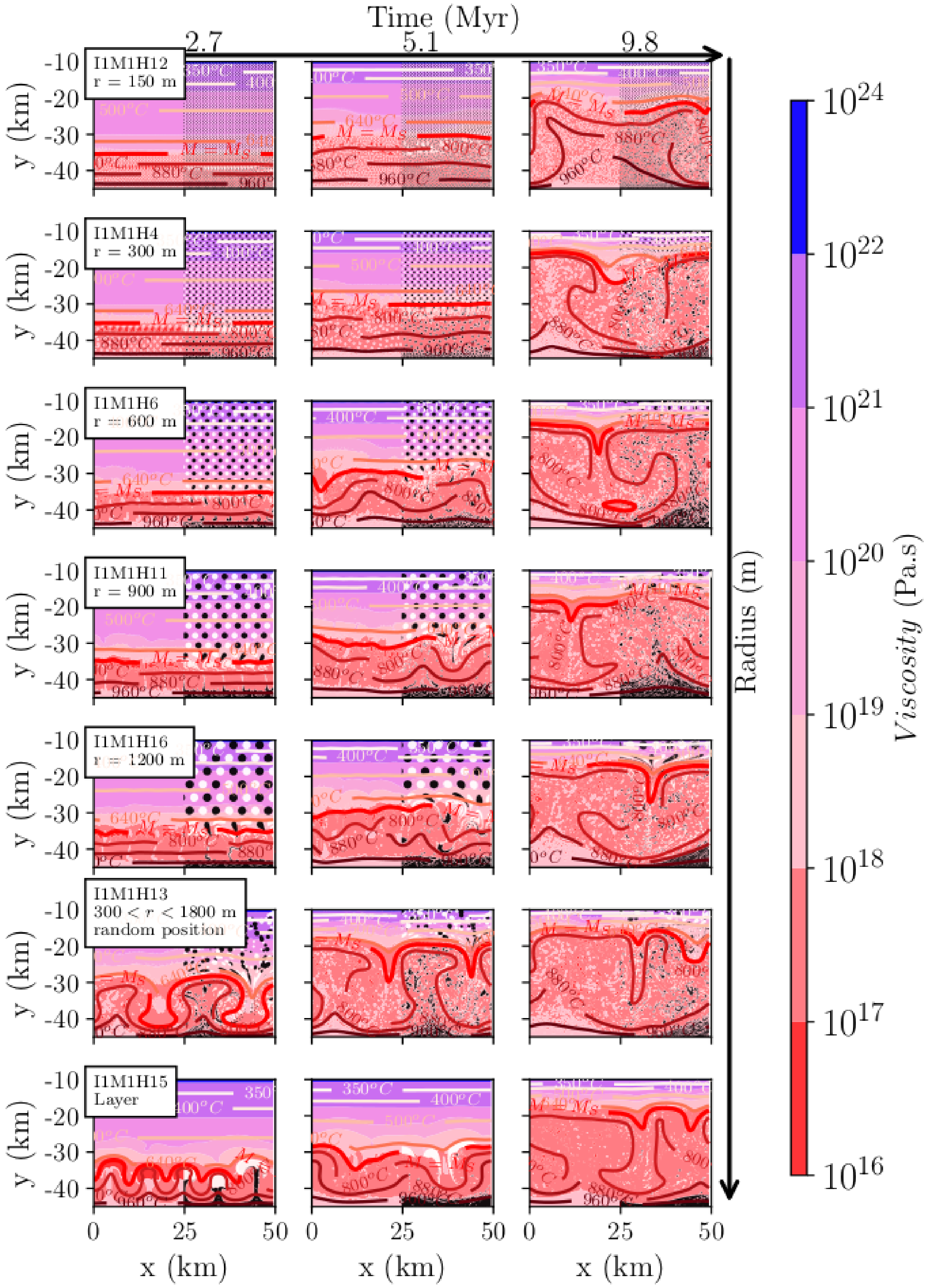

Figure 12. Influence of the size and the distribution of inclusions on the flow regime, for seven test cases (details in Table 3). For each case, snapshots present the viscosity distribution, temperature isocontours in ^{o} Celsius and, in the right half, the light and heavy inclusions in white and black, respectively.

Furthermore, the initial arrangement of the inclusions throughout the spatial domain also influences the shape of the structures that develop with time (Fig. 12):

- When the inclusions are initially arranged as horizontal layers over the base of the model domain (case $I_1M_1H_{15}$), diapirism develops with the light layer forming ascending domes. The typical size of these domes is proportional to the layers thickness ratio, as shown by Weinberg (1992) and Louis-Napoléon et al. (2020). The isotherms follow the doming, destabilize the system and ends up triggering convection after about 5 Myr. Ultimately, convection destroys the diapirs.
- When the inclusions are arranged randomly and have a random size (case $I_1M_1H_{13}$), the largest light inclusions rise faster than the smaller ones. Such a random arrangement is found to provide more space than in the ordered case, hence, the isotherms deform faster, which triggers convection earlier than in the ordered case (after about 2.5 Myr instead of 5 Myr in case $I_1M_1H_6$).
- The inclusions were also set to occupy only a portion of the system's height (cf. illustration in Appendix 2a) over thicknesses of $7 \leq h \leq 35$ km. This thinning of the inclusions layer mainly reduces their impact on the main flow dynamics, hence, they are more easily dragged into the convective flow.

Note also that here, we only compared the last convection stage between different test cases, because the earlier convective stages are difficult to distinguish one from the other systematically.

For all cases, the onset of convection occurs between $2.5 < t_{conv} < 12.5$ Myr. The more viscous the fluids, the more convection is delayed, but it is facilitated when the light inclusions have a lower density, are larger, or have a higher rate of heat production. The periods of the convective cycles range between $0.75 < \tau < 2$ Myr. The maximum velocities range between $2.8 < v_{max} < 20$ cm.yr^{-1} and the average vertical velocity is around $\approx 1.5\ cm.yr^{-1}$. The case that displays the lowest velocities (average and maximum) has a high viscosity of unmolten rocks, μ_{UM} ($I_1M_1H_7$). The case that displays the highest velocities has the lowest viscosity of the partially molten domains ($I_1M_1H_0$, $\mu_1^0 = 5 \times 10^{15}$ Pa.s).

These conclusions apply to cases belonging to the *suspension* regime; a more exhaustive study deserves to be carried out to assess in greater detail the influence of heterogeneities sizes on structures characterising the other flow regimes (e.g. Appendix 2b). This information is important since combined with field data, it should return constraints on characteristic sub-scale structures and processes. This point will be further addressed in paper part II (in prep.).

5 Discussion

5.1 Significance of our results compared to previous studies

We assume in the present study that heterogeneities resulting from partial melting in the crust may be represented by inclusions of sizes of several hundred meters and of contrasted densities and viscosities with respect to the surrounding environment. This size of heterogeneous inclusions corresponds to evaluations from previous studies for i) the typical size at which such heterogeneities may significantly influence crustal scale convective flow (Harada et al. 2012), and ii) the typical size achieved by melt pockets resulting from the subscale dynamics of melt propagation via porous flow in felsic crust (Weinberg 1999; Brown 2010; Edmonds et al. 2019). This simplification encompassing multiple chemical reactions and fluid propagation processes at the subscale may also apply to some degree to systems involving particles and convective flow in magma chambers or planetary mantle dynamics.

Our synthesis diagrams (Figures 7 and 11) highlight the mutual interaction between the motion of such heterogeneous inclusions and the dynamics of convection, depending on the physical properties of both the unmolten and the partially molten fluid phases. To our knowledge, this is the first time that a regime map is proposed describing the suspension, diapirism and layering of deformable heterogeneities in felsic crust, where these heterogeneities can break-up or coalesce in a system with a non linear rheology. We are not aware of other studies that consider heterogeneities of similarly complex behaviour.

In comparison with previous works, several theoretical and experimental studies have investigated the dynamics of sinking heavy rigid inclusions (Harada et al. 2012); the particles have either, a ”collective fluid-like” behavior, with falling pockets of particles forming diapirs, or an individual behavior (”particle-like” behavior). The higher the concentration of particles, the closer they are to each other and the more they behave like a “collective” fluid. Then, their behavior follows the Rayleigh-Taylor linear stability theory (Chandrasekhar 2013; Deubelbeiss & Kaus 2008; Harada et al. 2012). In contrast when particles behave individually, they settle at their Stokes velocity (Martin & Nokes 1988; Harada et al. 2012).

The specific evolution of heavy particles in convective systems has been studied both experimentally (Lavorel & Le Bars 2009; Shibano et al. 2012, 2013) and numerically (Höink et al. 2005; Patočka et al. 2020). While density contrasts exert a strong influence on both convection and particles deposition rates (e.g. Martin & Nokes 1988; Tackley 1993; Patočka et al. 2020), here we considered only a moderate range of density contrasts ($\sim 10\%$), specific to felsic crustal systems. Within that range, their impact was found marginal.

Shibano et al. (2013) studied segregation in magma chambers with heavy glass beads in heated wax; they obtained sinking beads velocities higher than ours, most likely because their density differences are of the order of 50% (ca. 1100 vs 2500 $\mathrm{kg.m^{-3}}$), a situation not applicable to our crustal scale systems. They also studied the influence of particles of different sizes, and obtained alternating layers of small and large particles, which nicely illustrates segregation-related processes. Here instead, we studied the segregation of light *and* heavy inclusions, and we also obtained a range of conditions in which layering occurs. Although we illustrated several cases displaying the influence of inclusions sizes (cases $I_1M_1H_{11,12,13}$, Fig. 12), additional numerical experiments should further investigate this.

Most studies focus on the impact of convection on the particles rather than on the impact of particles on convection (Koyaguchi et al. 1990). Here, we illustrated that the main convective flow velocity is impacted when compared with a system without particles (see e.g. the comparison with Favier et al. 2019), but a more specific study would be required to precise the dependence on particles concentration. Note that here we considered high heterogeneities concentrations, $\phi = dv/v = 0.35$ whereas usually, $\phi < 0.3$ (v is volume, e.g. Lavorel & Le Bars 2009; Verhoeven & Schmalzl 2009). Nonetheless, the regimes that we obtain with such high concentrations and our moderate density contrasts deserve to be discussed in comparison to the criterion determined previously to separate the suspension and the deposition regimes of heavy particles (Lavorel & Le Bars 2009; Martin & Nokes 1988). To characterize this criteria, authors use a chemical Rayleigh number (Verhoeven & Schmalzl 2009) and/or the Stokes number (Patočka et al. 2020), especially at high Rayleigh numbers. The chemical Rayleigh number is nothing but the product of the Rayleigh number and a buoyancy number (B). In Appendix 5, we plot the dimensionless representation of Verhoeven & Schmalzl (2009) for few rigid inclusions ($\phi < 0.3$), separating the so-called T-regime, which is dominated by thermal convection, and the C-regime, characterized by the coexistence of a sediment layer and a suspension layer. The results of Verhoeven & Schmalzl (2009) and Höink et al. (2005) display a similar trend, and our results are plotted in this diagram by assimilating our Ra_{PM} to these studies Rayleigh number. It is then difficult to conclude about whether our simulations lie in the T-regime or in the C-regime since (i) our plotted values with largest Ra_{PM} appear close to the transition identified by Höink et al. (2005), and (ii) the time duration of our runs is smaller than the typical residence time of the inclusions (Appendix 5). Numerical simulation times larger than this characteristic residence time would thus be required to further clarify where our flow regimes stand, which is out of the scope of the present study. Indeed, the time window considered here (20 Myr, when gravitational instabilities are likely to be hindered by tectonic instabilities in orogenic crust) is significantly smaller than the theoretical deposition time (88 Myr) deduced from the formula first proposed by Martin & Nokes (1988) to describe the settling rate of heavy particles. Nevertheless and for information, all our cases fall in the so-called 'dust-like' suspension regime described by Patočka et al. (2020) (Appendix 5).

Another comment regarding our work is that we could not precisely determine the values of the critical dimensionless numbers ($Ra_{UM}$and Ra_{PM}) that characterize the conditions for suspension, diapirism or layering of the inclusions, because of the temperature and strain-rate viscosity dependency of our deformable inclusions. This complex rheology may also partly explain second order differences with the above mentioned studies that assumed instead rigid heavy particles.

Our study was originally motivated by the question of the controlling parameters on the shape and size of the segregated layer of light inclusions below the rigid upper crust (layer 2) described in section 4.2.2. This layer develops in the "*diapiric*" and in the "*layering*" transitional regimes; its shape evolves over time, rendering it more difficult to characterize the conditions for its development. Future work should investigate more systematically the influence of the inclusions' distribution and size, their rheological properties, as well as the influence of evolving kinematic and thermal boundary conditions. While a more systematic parametric study ought to be conducted, we recognise that information provided by geological data remains essential, in terms of matching the shapes, sizes, timing, and pressure-temperature-compositions of partially molten crustal domains. This is discussed below.

5.2 Gravitational instabilities in partially molten continental crust

The different flow regimes investigated in this paper might apply to various geological contexts if the conditions for partial melting are met, namely if the composition of the crust is fertile and the thermal setting is favorable within a relatively high geothermal gradient, owing to radiogenic decay and/or high mantle heat flux (England & Thompson 1984; Vanderhaeghe et al. 2003; Henk et al. 2000). Significant partial melting of the continental crust is favored by a felsic rather than a mafic composition

(Thompson & Connolly 1995). On the other hand, the Earth has been marked by secular cooling since its accretion (Labrosse & Jaupart 2007), which is expressed in particular by a decrease in the mantle potential temperature (Herzberg et al. 2010) and in radioactive isotopes content (Arevalo Jr et al. 2009). Accordingly, the continental crust was more prone to be affected by partial melting during the Archean period (Vanderhaeghe et al. 2019) and the geothermal gradient recorded by metamorphic mineral assemblages has decreased since then (Brown, 2018). In compensation to the decreasing contribution of radioactive isotopes since Archean times, partial melting of the continental crust now requires either crustal thickening and/or thinning of the lithospheric mantle (England & Thompson 1986; Houseman et al. 1981; Henk et al. 2000). The most favorable setting for crustal partial melting nowadays is provided along convergent plate boundaries marked by tectonic accretion coeval with slab retreat, resulting in both an increased radioactive heat production in the crust and a basal heat flux from the mantle (Vanderhaeghe & Duchêne 2010; Ueda et al. 2012).

On the other hand, geological data of migmatitic terranes provide insights on the types of gravitational instabilities at play, and on the flow regime that can affect a partially molten crust. The presence of dome shapes points to the imprint of diapirism and/or convection at a scale that is comparable to the diameter of the domes. The most famous examples of crustal scale domes, with a diameter of more than 20 km, are displayed in the Pilbara and Barberton Archean cratons (Van Kranendonk et al. 2004, 2007). More recent examples are exposed in thermally matured Phanerozoic orogenic belts such as the Variscan belt (Burg & Vanderhaeghe 1993; Ledru et al. 2001; Charles et al. 2009; Trap et al. 2017; Van Den Driessche & Brun 1992), the Canadian Cordillera (Amato et al. 1994; Vanderhaeghe et al. 2003; Kruckenberg et al. 2008), or the Alpine-Himalayan belt (Vanderhaeghe & Whitney 2004; Kruckenberg

Table 4. Range of viscosity properties of a hot orogenic crust of thickness $H = 45$ km expected to behave according to the four regimes displayed in Fig. 7, with properties reported in Table 1. An equivalent figure function of crustal viscosities is provided in Appendix 6. A and μ_0 are the exponential prefactors in Eqs. 9.

Regime		Rheology	
Convection	Heterogeneities	Unmolten rock	Partially molten rock
none	no motion	$0 < A < \infty$	$\mu_0 \gtrsim 10^{18}$ Pa.s
none	diapirism	$A \lesssim 3 \times 10^{-5}$ Pa^{-n}.s^{-1}	$4 \times 10^{16} \lesssim \mu_0 \lesssim 10^{18}$ Pa.s
local convection	layering	$A \lesssim 3 \times 10^{-5}$ Pa^{-n}.s^{-1}	$\mu_0 \lesssim 4 \times 10^{16}$ Pa.s
global convection	suspension	$A \gtrsim 3 \times 10^{-5}$ Pa^{-n}.s^{-1}	$\mu_0 \lesssim 10^{18}$ Pa.s

et al. 2011; Mahéo et al. 2002; Whitney et al. 2004). Furthermore, on Naxos in the Aegean domain, U-Pb geochronological data on zircons record cyclic crystallization in the $700 - 900^{o}C$ critical range of temperature close to the granitic solidus, and were interpreted to witness convective motion (Vanderhaeghe et al. 2018). The heterogeneity of migmatitic terranes might provide insights on the efficiency of melt/solid segregation and whether the flow regime was dominated by layering or suspension. The ubiquitous compositional layering character of the continental crust (Rudnick et al. 2003; Mooney et al. 2002) testifies of both the efficiency and the diversity of crustal differentiation modes (Brown 1995; Sawyer et al. 1999; Weinberg 1999; Cagnard et al. 2011; Saha-Fouotsa et al. 2019; Toé et al. 2013).

Hence while melt/solid segregation layering processes in mid-crustal migmatite terranes at ± decametric scales are attributable to dominating porous-media compaction processes, layering and dome formation at ± kilometric scales may result from dominating bulk-media suspension and segregation processes such as those modeled here.

Finally, the range of application of the different regimes modeled here might be evaluated from values of Ra_{UM} and Ra_{PM} based on the geological characteristics of a specific field target. For example, a partially molten crust with a thickness of 25 km and a temperature gradient of 300°C, increasing from 600 to 900 °C, requires a viscosity of the partially molten rock of less than 4×10^{16} Pa.s and a rheology of the unmolten rock such that $A \lesssim 3 \times 10^{-5}$ $\mathrm{Pa^{-n}.s^{-1}}$ to achieve a "*layering*" regime (see Table 4). Increasing the thickness of the partially molten layer, or increasing the temperature gradient, favors the transition of this regime towards a convection regime with suspension. Our first order evaluation of the physical parameters required for the development of gravitational instabilities in a heterogeneous, partially molten crust, and their comparison with geological data indicate that these processes are potentially active in a large number of settings, from Archean to Phanerozoic times.

6 Conclusion

We studied numerically, using a VOF approach, the conditions for convection in a partially molten, hot orogenic crust, with consideration of heterogeneous inclusions of typical sizes of a few hundred meters. These inclusions at the onset of our models represent clusters of light or heavy, less or more viscous material with respect to the averaged equivalent medium, and were assumed to have resulted from sub-scale melting processes, not modeled here. These inclusions impact the convection regime and decrease the velocity of the convection cells in comparison to cases without inclusions.

The main result of this work is that various flow regimes are obtained depending on the properties of the unmolten and partially molten rocks. We describe these regimes using two Rayleigh numbers denoted Ra_{UM} and Ra_{PM}, for the unmolten and partially molten domains, respectively :

- *No convection + diapirism*: When both Rayleigh numbers are small ($2 \times 10^2 \lesssim Ra_{PM} \lesssim 4 \times 10^3$ and $Ra_{UM} \lesssim 10$), the thermal regime is diffusive and associated with a basic segregation regime in which i) the heavy inclusions sink onto the base of the modeled domain and ii) the light inclusions float up and stack below the rigid and cold upper crustal lid. Hence each group of inclusions ends up forming a horizontal layer about 5 km thick, at 45 km and at 15 km depth, respectively. This regime allows for the aggregation (or clustering) of various light inclusions, which forms diapiric domes at the top of the partially molten layer and deforms the base of the upper crust.

- *Global convection + suspension*: Conversely, when both Rayleigh numbers are large enough ($Ra_{PM} \gtrsim 2 \times 10^2$ and $Ra_{UM} \gtrsim 10$), we observe a *suspension* regime where convective flow and inclusions interact. Convection drags the inclusions into cyclic revolutions and prevents the clustering of the light inclusions below the rigid upper crust, whereas some of the heavy inclusions settle and form a sediment layer. In turn, the inclusions tend to reduce the convection intensity.

- *'Confined' convection + layering*: This intermediate regime corresponds to large Ra_{PM} and low Ra_{UM} ($Ra_{PM} \gtrsim 4 \times 10^3$ and $Ra_{UM} \lesssim 10$). There, the unmolten layer is much more viscous than in the suspension regime and it acts as a rigid lid. As the light inclusions migrate upwards, they merge as "floating" clusters stuck in the low-velocity boundary layer under the rigid upper crust (in the same way in which the heavy inclusions settle at the bottom of the domain and form a sediment layer). These clusters can form domes, that might be preserved if ultimately the thermal and kinematic conditions change and let them exhume to shallower depths. Such a situation will be further investigated in the companion paper part II (in prep).

When the melting front rises up to the base of the upper crust and the convective vigor is weak, light inclusions may form a horizontal layer at the top of the convective cells, in the *diapiric* or in the *layering* regime. The *layering* regime is controled by the sharpness of the viscosity gradient with depth at this strength "boundary" (which may also be refered as the crust's brittle ductile transition):

only if the viscosity gradient is sharp enough and in the appropriate range of magnitude, can the light inclusions stack and remain stuck there without being reentrained in the convective cells.

This *layering* process indicates that crustal-scale domes cored by migmatites and granites, typical of Archean cratons and of thermally mature orogenic belts, potentially reflect the development of specific regimes of crustal-scale gravitational instabilities owing to partial melting. Hence, crustal differentiation is controlled by potentially distinct gravitationally driven flow regimes (*diapirism*, convection with *layering*, convection with *suspension*) and thus by the viscosity and density contrasts between the various fluid phases. Note that both *diapirism* and convection with *layering* lead to marked crustal-scale differentiation whereas convection with *suspension* tends to redistribute heterogeneities and thus homogeneize the composition of the crust.

Given these trends, the question remains of the narrow parametric range that allows for the formation of narrow diapirs at shallow crustal depths. This question will be addressed in a companion paper dedicated to the physical conditions required for the development of domes and subdomes on Naxos Island (Greece).

ACKNOWLEDGMENT

We are grateful to the Institut National Polytechnique de Toulouse (INPT) which supported this work. Complementary financial support by INSU-Syster is acknowledged. Part of the computational time was provided by the super computing center CALMIP (Toulouse, project P1525). This paper is part of the PhD thesis of the first author. We warmly thank V. Patočka, an anonymous reviewer and editor G. Choblet for their constructive remarks which greatly helped improving this study. We also thank Nathan Maury for his careful check of the parameters values in Table 3.

Data availability

Our numerical models are performed with our own solver called *multiMeltInterFoam*, which is available here: `https://gitlab.com/AurelieLN/MultiMeltInterFoam.git`.

REFERENCES

Amato, J. M., Wright, J. E., Gans, P. B., & Miller, E. L., 1994. Magmatically induced metamorphism and deformation in the kigluaik gneiss dome, seward peninsula, alaska, *Tectonics*, **13**(3), 515–527.

Arevalo Jr, R., McDonough, W. F., & Luong, M., 2009. The k/u ratio of the silicate earth: Insights into mantle composition, structure and thermal evolution, *Earth and Planetary Science Letters*, **278**(3-4), 361–369.

Artemieva, I. M. & Mooney, W. D., 2001. Thermal thickness and evolution of precambrian lithosphere: A global study, *Journal of Geophysical Research: Solid Earth*, **106**(B8), 16387–16414.

Arzi, A. A., 1978. Critical phenomena in the rheology of partially melted rocks, *Tectonophysics*, **44**(1-4), 173–184.

Babeyko, A., Sobolev, S., Trumbull, R., Oncken, O., & Lavier, L., 2002. Numerical models of crustal scale convection and partial melting beneath the altiplano–puna plateau, *Earth and Planetary Science Letters*, **199**(3), 373 – 388.

Berberović, E., van Hinsberg, N. P., Jakirlić, S., Roisman, I. V., & Tropea, C., 2009. Drop impact onto a liquid layer of finite thickness: Dynamics of the cavity evolution, *Physical Review E*, **79**, 036306.

Bittner, D. & Schmeling, H., 1995. Numerical modelling of melting processes and induced diapirism in the lower crust, *Geophysical Journal International*, **123**(1), 59–70.

Bousquet, R., Goffé, B., Henry, P., Le Pichon, X., & Chopin, C., 1997. Kinematic, thermal and petrological model of the central alps: Lepontine metamorphism in the upper crust and eclogitisation of the lower crust, *Tectonophysics*, **273**(1-2), 105–127.

Brown, M., 1995. Mechanisms and consequence of melt segregation from crustal protolith, *Journal of Geophysical Research*, **100**, 15655–15679.

Brown, M., 2010. Melting of the continental crust during orogenesis: the thermal, rheological, and compositional consequences of melt transport from lower to upper continental crust, *Canadian Journal of Earth Sciences*, **47**(5), 655–694.

Burg, J.-P. & Gerya, T., 2005. The role of viscous heating in Barrovian metamorphism of collisional orogens: thermomechanical models and application to the Lepontine Dome in the Central Alps, *Journal of Metamorphic Geology*, **23**(2), 75–95.

Burg, J.-P. & Vanderhaeghe, O., 1993. Structures and way-up criteria in migmatites, with application to the Velay dome (French Massif Central), *Journal of Structural Geology*, **15**(11), 1293–1301.

Burg, J.-P. & Vigneresse, J.-L., 2002. Non-linear feedback loops in the rheology of cooling-crystallizing felsic magma and heating-melting felsic rock, *Geological Society, London, Special Publications*, **200**(1), 275–292.

Bürgmann, R. & Dresen, G., 2008. Rheology of the lower crust and upper mantle: Evidence from rock mechanics, geodesy, and field observations, *Annual Review of Earth and Planetary Sciences*, **36**, 531–567.

Burov, E. & Gerya, T., 2014. Asymmetric three-dimensional topography over mantle plumes, *Nature*, **513**(7516), 85—89.

Cagnard, F., Barbey, P., & Gapais, D., 2011. Transition between "archaean-type" and "modern-type" tectonics: Insights from the finnish lapland granulite belt, *Precambrian Research*, **187**(1-2), 127–142.

Cao, W., Kaus, B., & Paterson, S., 2016. Intrusion of granitic magma into the continental crust facilitated by magma pulsing and dike-diapir interactions: Numerical simulations, *Tectonics*, **35**(6), 1575–1594, 2015TC004076.

Caricchi, L., Burlini, L., Ulmer, P., Gerya, T., Vassalli, M., & Papale, P., 2007. Non-newtonian rheology of crystal-bearing magmas and implications for magma ascent dynamics, *Earth and Planetary Science Letters*, **264**(3-4), 402–419.

Chandrasekhar, S., 2013. *Hydrodynamic and hydromagnetic stability*, Courier Corporation.

Charles, N., Faure, M., & Chen, Y., 2009. The montagne noire migmatitic dome emplacement (french massif central): new insights from petrofabric and ams studies, *Journal of structural geology*, **31**(11), 1423–1440.

Chen, Y. & Morgan, W. J., 1990. A nonlinear rheology model for mid-ocean ridge axis topography, *Journal of Geophysical Research: Solid Earth*, **95**(B11), 17583–17604.

Connolly, J. A. & Podladchikov, Y. Y., 2015. An analytical solution for solitary porosity waves: dynamic permeability and fluidization of nonlinear viscous and viscoplastic rock, *Geofluids*, **15**(1-2), 269–292.

Cruden, A., Koyi, H., & Schmeling, H., 1995. Diapiric basal entrainment of mafic into felsic magma, *Earth and Planetary Science Letters*, **131**(3-4), 321–340.

Culha, C., Suckale, J., Keller, T., & Qin, Z., 2020. Crystal fractionation by crystal-driven convection, *Earth and Space Science Open Archive*.

Davis, S. H., Müller, U., & Dietsche, C., 1984. Pattern selection in single-component systems coupling bénard convection and solidification, *Journal of Fluid Mechanics*, **144**, 133–151.

Deubelbeiss, Y. & Kaus, B., 2008. Comparison of Eulerian and Lagrangian numerical techniques for the stokes equations in the presence of strongly varying viscosity, *Physics of the Earth and Planetary Interiors*, **171**(1), 92 – 111, Recent Advances in Computational Geodynamics: Theory, Numerics and Applications.

Dewey, J., 1986. Diversity in the lower continental crust, *Geological Society, London, Special Publications*, **24**(1), 71–78.

Dufek, J. & Bergantz, G., 2005. Lower crustal magma genesis and preservation: a stochastic framework for the evaluation of basalt–crust interaction, *Journal of Petrology*, **46**(11), 2167–2195.

Edmonds, M., Cashman, K. V., Holness, M., & Jackson, M., 2019. Architecture and dynamics of magma reservoirs.

England, P. C. & Thompson, A., 1986. Some thermal and tectonic models for crustal melting in continental collision zones, *Geological Society, London, Special Publications*, **19**(1), 83–94.

England, P. C. & Thompson, A. B., 1984. Pressure—temperature—time paths of regional metamorphism i. heat transfer during the evolution of regions of thickened continental crust, *Journal of Petrology*, **25**(4), 894–928.

Esfahani, B. R., Hirata, S. C., Berti, S., & Calzavarini, E., 2018. Basal melting driven by turbulent thermal convection, *Physical Review Fluids*, **3**(5), 053501.

Favier, B., Purseed, J., & Duchemin, L., 2019. Rayleigh–Bénard convection with a melting boundary, *Journal of Fluid Mechanics*, **858**, 437–473.

Fedkiw, R. P., Aslam, T., Merriman, B., & Osher, S., 1999. A non-oscillatory eulerian approach to interfaces in multimaterial flows (the ghost fluid method), *Journal of computational physics*, **152**(2), 457–492.

Ganne, J., Gerbault, M., & Block, S., 2014. Thermo-mechanical modeling of lower crust exhumation—constraints from the metamorphic record of the palaeoproterozoic eburnean orogeny, west african craton, *Precambrian Research*, **243**, 88–109.

Gerbault, M., Schneider, J., Reverso-Peila, A., & Corsini, M., 2018. Crustal exhumation during ongoing compression in the Variscan Maures-Tanneron Massif, France-Geological and thermo-mechanical aspects, *Tectonophysics*, **746**, 439–458.

Gerya, T. V. & Burg, J.-P., 2007. Intrusion of ultramafic magmatic bodies into the continental crust: Numerical simulation, *Physics of the Earth and Planetary Interiors*, **160**(2), 124 – 142.

Gerya, T. V. & Yuen, D. A., 2003. Rayleigh–Taylor instabilities from hydration and melting propel 'cold plumes' at subduction zones, *Earth and Planetary Science Letters*, **212**(1-2), 47–62.

Graham, C. M. & England, P. C., 1976. Thermal regimes and regional metamorphism in the vicinity of overthrust faults: an example of shear heating and inverted metamorphic zonation from southern california, *Earth and Planetary Science Letters*, **31**(1), 142–152.

Hacker, B., Abers, G., & Peacock, S., 2003. Subduction factory 1. theoretical mineralogy, densities, seismic wave speeds, and h2o contents: Journal of geophysical research, *B, Solid Earth and Planets*, **108**.

Harada, S., Mitsui, T., & Sato, K., 2012. Particle-like and fluid-like settling of a stratified suspension, *The European Physical Journal E*, **35**(1), 1–6.

Heister, T., Dannberg, J., Gassmöller, R., & Bangerth, W., 2017. High accuracy mantle convection simulation through modern numerical methods–ii: realistic models and problems, *Geophysical Journal International*, **210**(2), 833–851.

Henk, A., von Blanckenburg, F., Finger, F., Schaltegger, U., & Zulauf, G., 2000. Syn-convergent high-temperature metamorphism and magmatism in the variscides: a discussion of potential heat sources, *Geo-*

logical Society, London, Special Publications, **179**(1), 387–399.

Herzberg, C., Condie, K., & Korenaga, J., 2010. Thermal history of the earth and its petrological expression, *Earth and Planetary Science Letters*, **292**(1-2), 79–88.

Hillebrand, B., Thieulot, C., Geenen, T., van den Berg, A. P., & Spakman, W., 2014. Using the level set method in geodynamical modeling of multi-material flows and earth's free surface, *Solid Earth*, **5**(2), 1087–1098.

Houseman, G. A., McKenzie, D. P., & Molnar, P., 1981. Convective instability of a thickened boundary layer and its relevance for the thermal evolution of continental convergent belts, *Journal of Geophysical Research: Solid Earth*, **86**(B7), 6115–6132.

Howard, L. N., 1966. Convection at high Rayleigh number, in Applied Mechanics, pp. 1109–1115, Springer Berlin Heidelberg, Berlin, Heidelberg.

Höink, T., Schmalzl, J., & Hansen, U., 2005. Formation of compositional structures by sedimentation in vigorous convection, *Physics of the Earth and Planetary Interiors*, **153**(1), 11 – 20, Studies of the Earth's Deep Interior.

Katz, R. F. & Weatherley, S. M., 2012. Consequences of mantle heterogeneity for melt extraction at mid-ocean ridges, *Earth and Planetary Science Letters*, **335**, 226–237.

Keller, T., May, D. A., & Kaus, B. J. P., 2013. Numerical modelling of magma dynamics coupled to tectonic deformation of lithosphere and crust, *Geophysical Journal International*, **195**(3), 1406–1442.

Kincaid, C. & Silver, P., 1996. The role of viscous dissipation in the orogenic process, *Earth and Planetary Science Letters*, **142**(3-4), 271–288.

Kirby, S. H., 1985. Rock mechanics observations pertinent to the rheology of the continental lithosphere and the localization of strain along shear zones, *Tectonophysics*, **119**(1-4), 1–27.

Kisters, A., Ward, R., Anthonissen, C., & Vietze, M., 2009. Melt segregation and far-field melt transfer in the mid-crust, *Journal of the Geological Society*, **166**(5), 905–918.

Kohlstedt, D., Evans, B., & Mackwell, S., 1995. Strength of the lithosphere: Constraints imposed by laboratory experiments, *Journal of Geophysical Research: Solid Earth*, **100**(B9), 17587–17602.

Koyaguchi, T., Hallworth, M. A., Huppert, H. E., & Sparks, R. S. J., 1990. Sedimentation of particles from a convecting fluid, *Nature*, **343**(6257), 447.

Kraichnan, R. H., 1962. Turbulent thermal convection at arbitrary Prandtl number, *The Physics of Fluids*, **5**(11), 1374–1389.

Krishnamurti, R., 1970. On the transition to turbulent convection. part 1. the transition from two- to three-dimensional flow, *Journal Of Fluid Mechanics*, **42**(2), 295–307.

Kruckenberg, S., Vanderhaeghe, O., Ferré, E., Teyssier, C., , & Whitney, D., 2011. Flow of partially molten crust and the internal dynamics of a migmatite dome, Naxos, Greece, *Tectonics*, **30**(3).

Kruckenberg, S. C., Whitney, D. L., Teyssier, C., Fanning, C. M., & Dunlap, W. J., 2008. Paleocene-eocene migmatite crystallization, extension, and exhumation in the hinterland of the northern cordillera: Okanogan dome, washington, usa, *Geological Society of America Bulletin*, **120**(7-8), 912–929.

Labrosse, S. & Jaupart, C., 2007. Thermal evolution of the earth: Secular changes and fluctuations of plate characteristics, *Earth and Planetary Science Letters*, **260**(3-4), 465–481.

Lavorel, G. & Le Bars, M., 2009. Sedimentation of particles in a vigorously convecting fluid, *Physical Review E*, **80**(4), 046324.

Ledru, P., Courrioux, G., Dallain, C., Lardeaux, J., Montel, J., Vanderhaeghe, O., & Vitel, G., 2001. The Velay dome (French Massif Central): melt generation and granite emplacement during orogenic evolution, *Tectonophysics*, **342**(3-4), 207–237.

Leitch, A. & Weinberg, R. F., 2002. Modelling granite migration by mesoscale pervasive flow, *Earth and Planetary Science Letters*, **200**(1-2), 131–146.

Louis-Napoléon, A., Gerbault, M., Bonometti, T., Thieulot, C., Martin, R., & Vanderhaeghe, O., 2020. 3-d numerical modelling of crustal polydiapirs with Volume-Of-Fluid methods, *Geophysical Journal International*, **222**(1), 474–506.

Louis-Napoléon, A., 2020. *Modélisation d'instabilités gravitaires au sein de la croûte partiellementfondue par une méthode de Volume-Of-Fluid*, Ph.D. thesis, University Paul Sabatier, Institut National Polytechnique de Toulouse.

Maaløe, S., 1992. Melting and diffusion processes in closed-system migmatization, *Journal of Metamorphic Geology*, **10**(4), 503–516.

Mahéo, G., Guillot, S., Blichert-Toft, J., Rolland, Y., & Pêcher, A., 2002. A slab breakoff model for the neogene thermal evolution of south karakorum and south tibet, *Earth and Planetary Science Letters*, **195**(1-2), 45–58.

Martin, D. & Nokes, R., 1988. Crystal settling in a vigorously convecting magma chamber, *Nature*, **332**(6164), 534–536.

Molnar, P. & England, P., 1990. Temperatures, heat flux, and frictional stress near major thrust faults, *Journal of Geophysical Research: Solid Earth*, **95**(B4), 4833–4856.

Mooney, W. D., Prodehl, C., & Pavlenkova, N. I., 2002. Seismic velocity structure of the continental lithosphere from controlled source data, *INTERNATIONAL GEOPHYSICS SERIES*, **81**(A), 887–910.

Osher, S. & Sethian, J. A., 1988. Fronts propagating with curvature-dependent speed: algorithms based on Hamilton-Jacobi formulations, *Journal of computational physics*, **79**(1), 12–49.

Patočka, V., Čížková, H., & Tackley, P., 2019. Do elasticity and a free surface affect lithospheric stresses caused by upper-mantle convection?, *Geophysical Journal International*, **216**(3), 1740–1760.

Patočka, V., Calzavarini, E., & Tosi, N., 2020. Settling of inertial particles in turbulent Rayleigh-Bénard convection, *Physical Review Fluids*, **5**(11), 114304.

Perchuk, L., Podladchikov, Y. Y., & Polyakov, A., 1992. Hydrodynamic modelling of some metamorphic processes, *Journal of Metamorphic Geology*, **10**(3), 311–319.

Puckett, E., Turcotte, D. L., He, Y., Lokavarapu, H., Robey, J. M., & Kellogg, L. H., 2018. New numerical approaches for modeling thermochemical convection in a compositionally stratified fluid, *Physics of the Earth and Planetary Interiors*, **276**, 10 – 35, Special Issue:15th SEDI conference.

Purseed, J., Favier, B., Duchemin, L., & Hester, E. W., 2020. Bistability in Rayleigh-Bénard convection with a melting boundary, *Physical Review Fluids*, **5**(2), 023501.

Pusok, A. E., Kaus, B. J., & Popov, A. A., 2017. On the quality of velocity interpolation schemes for marker-in-cell method and staggered grids, *Geophysics*, **174**(3), 1071–1089.

Rabinowicz, M. & Ceuleneer, G., 2005. The effect of sloped isotherms on melt migration in the shallow mantle: a physical and numerical model based on observations in the oman ophiolite, *Earth and Planetary Science Letters*, **229**(3-4), 231–246.

Ramberg, H., 1967. Gravity, deformation and the earth's crust, as studied by centrifuged models, *L.: Academic Press.–1967.–217 P.*

Ranalli, G., 1995. *Rheology of the Earth*, Springer Science & Business Media.

Rey, P., Teyssier, C., & Whitney, D. L., 2009. The role of partial melting and extensional strain rates in the development of metamorphic core complexes, *Tectonophysics*, **477**(3-4), 135–144.

Riel, N., Mercier, J., & Weinberg, R., 2016. Convection in a partially molten metasedimentary crust? Insights from the El Oro complex (Ecuador), *Geolology*, **44**(1), 31–34.

Robey, J. M. & Puckett, E. G., 2019. Implementation of a volume-of-fluid method in a finite element code with applications to thermochemical convection in a density stratified fluid in the earth's mantle, *Computers & Fluids*, **190**, 217–253.

Rosenberg, C. & Handy, M., 2005. Experimental deformation of partially melted granite revisited: implications for the continental crust, *Journal of metamorphic Geology*, **23**(1), 19–28.

Royden, L., 1996. Coupling and decoupling of crust and mantle in convergent orogens: Implications for strain partitioning in the crust, *Journal of Geophysical Research*, **101**(B8), 17679–17705.

Rudnick, R., Gao, S., Holland, H., Turekian, K., et al., 2003. Composition of the continental crust, *The crust*, **3**, 1–64.

Rudnick, R. L. & Fountain, D. M., 1995. Nature and composition of the continental crust: a lower crustal perspective, *Reviews of geophysics*, **33**(3), 267–309.

Rushmer, T., 2001. Volume change during partial melting reactions: implications for melt extraction, melt geochemistry and crustal rheology, *Tectonophysics*, **342**(3-4), 389–405.

Rutter, E., Brodie, K., & Irving, D., 2006. Flow of synthetic, wet, partially molten "granite" under undrained conditions: an experimental study, *Journal of Geophysical Research: Solid Earth*, **111**(B6).

Rutter, E., Mecklenburgh, J., & Brodie, K., 2011. Rock mechanics constraints on mid-crustal low-viscosity flow beneath tibet, *Geological Society, London, Special Publications*, **360**(1), 329–336.

Saha-Fouotsa, A. N., Vanderhaeghe, O., Barbey, P., Eglinger, A., Tchameni, R., Zeh, A., Tchunte, P. F., & Nomo, E. N., 2019. The geologic record of the exhumed root of the central african orogenic belt in the central cameroon domain (mbé–sassa-mbersi region), *Journal of African Earth Sciences*, **151**, 286–314.

Sawyer, E., 1994. Melt segregation in the continental crust, *Geology*, **22**(11), 1019–1022.

Sawyer, E., 2010. Migmatites formed by water-fluxed partial melting of a leucogranodiorite protolith: Microstructures in the residual rocks and source of the fluid, *Lithos*, **116**(3-4), 273–286.

Sawyer, E., Dombrowski, C., & Collins, W., 1999. Movement of melt during synchronous regional deformation and granulite-facies anatexis, an example from the wuluma hills, central australia, *Geol. Soc. London, Spec. Pub.*, **168**(1), 221–237.

Schenker, Filippo, L., Gerya, T., & Burg, J.-P., 2012. Bimodal behavior of extended continental lithosphere: Modeling insight and application to thermal history of migmatitic core complexes, *Tectonophysics*, **579**, 88–103.

Schmeling, H., Babeyko, A., Enns, A., Faccenna, C., Funiciello, F., Gerya, T., Golabek, G., Grigull, S., Kaus, B., Morra, G., Schmalholz, S., & van Hunen, J., 2008. A benchmark comparison of spontaneous subduction models—towards a free surface, *Physics of the Earth and Planetary Interiors*, **171**(1), 198 – 223.

Schmeling, H., Marquart, G., Weinberg, R., & Wallner, H., 2019. Modelling melting and melt segregation by two-phase flow: new insights into the dynamics of magmatic systems in the continental crust, *Geophysical Journal International*, **217**(1), 422–450.

Sethian, J. A. & Smereka, P., 2003. Level set methods for fluid interfaces, *Annual review of fluid mechanics*, **35**(1), 341–372.

Shibano, Y., Namiki, A., & Sumita, I., 2012. Experiments on upward migration of a liquid-rich layer in a granular medium: Implications for a crystalline magma chamber, *Geochemistry, Geophysics, Geosystems*, **13**(3).

Shibano, Y., Sumita, I., & Namiki, A., 2013. A laboratory model for melting erosion of a magma chamber roof and the generation of a rhythmic layering, *Journal of Geophysical Research: Solid Earth*, **118**(8), 4101–4116.

Sparks, R. S. J., Huppert, H. E., & Turner, J. S., 1984. The fluid dynamics of evolving magma chambers, *Philosophical Transactions of the Royal Society of London. Series A, Mathematical and Physical Sciences*, **310**(1514), 511–534.

Sturtz, C., Kaminski, E., Limare, A., & Tait, S., 2021. The fate of particles in a volumetrically heated convective fluid at high prandtl number, *arXiv preprint arXiv:2101.06706*.

Suckale, J., Nave, J.-C., & Hager, B. H., 2010. It takes three to tango: 1. simulating buoyancy-driven flow in the presence of large viscosity contrasts, *Journal of Geophysical Research*, **115**(B7).

Suckale, J., Elkins-Tanton, L. T., & Sethian, J. A., 2012. Crystals stirred up: 2. numerical insights into the formation of the earliest crust on the moon, *Journal of Geophysical Research: Planets*, **117**(E8).

Tackley, P. J., 1993. Effects of strongly temperature-dependent viscosity on time-dependent, three-dimensional models of mantle convection, *Geophysical Research Letters*, **20**(20), 2187–2190.

Takei, Y. & Holtzman, B. K., 2009. Viscous constitutive relations of solid-liquid composites in terms of grain boundary contiguity: 1. grain boundary diffusion control model, *Journal of Geophysical Research: Solid Earth*, **114**(B6).

Thompson, A. B. & Connolly, J. A., 1995. Melting of the continental crust: some thermal and petrological constraints on anatexis in continental collision zones and other tectonic settings, *Journal of Geophysical Research: Solid Earth*, **100**(B8), 15565–15579.

Toé, W., Vanderhaeghe, O., André-Mayer, A.-S., Feybesse, J.-L., & Milési, J.-P., 2013. From migmatites to granites in the Pan-African Damara orogenic belt, Namibia, *Journal of African Earth Sciences*, **85**, 62–74.

Trap, P., Roger, F., Cenki-Tok, B., & Paquette, J.-L., 2017. Timing and duration of partial melting and magmatism in the variscan montagne noire gneiss dome (french massif central), *International Journal of Earth Sciences*, **106**(2), 453–476.

Ueda, K., Gerya, T. V., & Burg, J., 2012. Delamination in collisional orogens: Thermomechanical modeling, *Journal of Geophysical Research: Solid Earth*, **117**(B8).

Ulvrová, M., Labrosse, S., Coltice, N., Råback, P., & Tackley, P., 2012. Numerical modelling of convection interacting with a melting and solidification front: Application to the thermal evolution of the basal magma ocean, *Physics of the Earth and Planetary Interiors*, **206**, 51–66.

Van Den Driessche, J. & Brun, J.-P., 1992. Tectonic evolution of the montagne noire (french massif central): a model of extensional gneiss dome, *Geodinamica Acta*, **5**(1-2), 85–97.

Van der Molen, I. & Paterson, M., 1979. Experimental deformation of partially-melted granite, *Contributions to Mineralogy and Petrology*, **70**(3), 299–318.

Van Kranendonk, M. J., Collins, W., Hickman, A., & Pawley, M. J., 2004. Critical tests of vertical vs. horizontal tectonic models for the Archaean East Pilbara granite–greenstone terrane, Pilbara craton, western Australia, *Precambrian Research*, **131**(3-4), 173–211.

Van Kranendonk, M. J., Hugh Smithies, R., Hickman, A. H., & Champion, D., 2007. secular tectonic evolution of archean continental crust: interplay between horizontal and vertical processes in the formation of the pilbara craton, australia, *Terra Nova*, **19**(1), 1–38.

Vanderhaeghe, O., 2009. Migmatites, granites and orogeny: Flow modes of partially-molten rocks and magmas associated with melt/solid segregation in orogenic belts, *Tectonophysics*, **477**(3–4), 119 – 134.

Vanderhaeghe, O. & Duchêne, S., 2010. Crustal-scale mass transfer, geotherm and topography at convergent plate boundaries, *Terra Nova*, **22**(5), 315–323.

Vanderhaeghe, O. & Teyssier, C., 2001. Partial melting and flow of orogens, *Tectonophysics*, **342**(3-4), 451–472.

Vanderhaeghe, O. & Whitney, D., 2004. Structural development of the naxos migmatite dome, *Special paper - Geological Society of America*, pp. 211–228.

Vanderhaeghe, O., Teyssier, C., McDougall, I., & Dunlap, W. J., 2003. Cooling and exhumation of the shuswap metamorphic core complex constrained by 40ar/39ar thermochronology, *Geological Society of America Bulletin*, **115**(2), 200–216.

Vanderhaeghe, O., Kruckenberg, S., Gerbault, M., Martin, L., Duchêne, S., & Deloule, E., 2018. Crustal-scale convection and diapiric upwelling of a partially molten orogenic root (Naxos dome, Greece), *Tectonophysics*, **746**, 459–469.

Vanderhaeghe, O., Guergouz, C., Fabre, C., Duchêne, S., & Baratoux, D., 2019. Secular cooling and crystallization of partially molten Archaean continental crust over 1 Ga, *Comptes Rendus Geoscience*, **351**(8), 562 – 573, New aspects of magma storage and transfer.

Vasil, G. & Proctor, M., 2011. Dynamic bifurcations and pattern formation in melting-boundary convection, *Journal of Fluid Mechanics*, **686**, 77.

Verhoeven, J. & Schmalzl, J., 2009. A numerical method for investigating crystal settling in convecting magma chambers, *Geochemistry, Geophysics, Geosystems*, **10**(12).

Vigneresse, J.-L., 1995. Crustal regime of deformation and ascent of granitic magma, *Tectonophysics*, **249**(3), 187 – 202.

Wedepohl, K. H., 1995. The composition of the continental crust, *Geochimica et cosmochimica Acta*, **59**(7), 1217–1232.

Weinberg, F. R. & Schmeling, H., 1992. Polydiapirs : multiwavelength gravity structures, *Journal of Structural Geology.*, **14**(4), 425–436.

Weinberg, R. & Podladchikov, Y., 1994. Diapiric ascent of magmas through power law crust and mantle, *Journal of Geophysical Research*, **99**(B5), 9543–9559.

Weinberg, R. F., 1992. Internal circulation in a buoyant two-fluid newtonian sphere: implications for composed magmatic diapirs, *Earth Planet. Sci. Lett.*, **110**(1), 77 – 94.

Weinberg, R. F., 1999. Mesoscale pervasive felsic magma migration: alternatives to dyking, *Lithos*, **46**(3), 393 – 410.

Whitney, D. L., Teyssier, C., & Vanderhaeghe, O., 2004. Gneiss domes and crustal flow, *Gneiss domes in orogeny*, **380**, 15.

Whittington, A. G., Hofmeister, A. M., & Nabelek, P. I., 2009. Temperature-dependent thermal diffusivity of the Earth's crust and implications for magmatism, *Nature*, **458**(7236), 319–321.

Yamato, P., Duretz, T., May, D. A., & Tartese, R., 2015. Quantifying magma segregation in dykes, *Tectonophysics*, **660**, 132–147.

Appendix

1 Parametric study for system configurations with partial melting alone

We describe here the influence on the flow characteristics when changing the melting threshold, the viscosity of the unmolten medium or that of the partially molten media. Tables A1 and A2 provide the input and output parameters, respectively, for the reference case displayed in the main text ($I_0M_1H_0$) and for the complementary cases described below.

Here, we characterize the melting front dynamics and the different convective stages by quantitative indicators (Table A2):

- the final position of the melting front once the convection stabilizes: y_f,
- the horizontal average of the mean vertical velocity of the melting front: $|Uy|$,
- the convection wavelength at onset of convection: λ_{conv},
- the onset time of convection: t_{onset},
- the maximum period of convective cycles: τ,
- the maximum convection cell size: length × height ($l \times h$),
- the maximum temperature difference recorded by a marker: ΔT_{max},
- the minimum and maximum velocities recorded by a marker: v_{min}, v_{max}.

Table A1. Physical parameters for cases with partial melting only.

Case	μ^0	M_S	A	Ra_{UM}	Ra_{PM}
	$Pa.s$		$Pa^{-2.3}.s^{-1}$		
$I_0M_1H_0$	5×10^{15}	0.3	3.2×10^{-4}	100	2.4×10^4
$I_0M_1H_1$	2.5×10^{15}	0.3	3.2×10^{-4}	100	4.8×10^3
$I_0M_1H_2$	5×10^{16}	0.3	3.2×10^{-4}	100	2.4×10^3
$I_0M_1H_3$	5×10^{17}	0.3	3.2×10^{-4}	100	2.4×10^2
$I_0M_1H_4$	2.5×10^{15}	0.3	7.9×10^{-6}	0.15	4.8×10^3
$I_0M_1H_5$	5×10^{15}	0.1	3.2×10^{-4}	100	2.4×10^4

Table A2. Melting front and flow dynamics characteristics for the runs performed with partial melting only. The reference case $I_0M_1H_0$ and the other cases differ by one parameter (table A1). Cases names provide a link to the associated movie. y_f indicates the final depth of the melting front; $|U_y|_f$, the mean vertical velocity; λ, the wavelength at convection onset; t_{onset}, onset convection time; τ, maximum period of cycles; $l \times h$, maximum length $\times$ height cell size; ΔT_{max}, maximum temperature difference recorded by a marker; v_{min}-v_{max}, minimum and maximum vertical velocities recorded by a marker.

	Melt front	Convection							
Case	y_f	$\|Uy\|_f$	regime	λ	t_{onset}	τ	$l \times h$	ΔT_{max}	v_{min}-v_{max}
	(km)	$(cm.yr^{-1})$		(km)	(Myr)	(Myr)	(km)	(K)	(cm/yr)
$I_0M_1H_0$ (reference)	-15.5	5	1	10	2.4	0.5	5×15	150	1-10
			2	25	4	0.4	5×26	50	7-21
			3	50	10.1	0.5	25×20	50	3-35
$I_0M_1H_1$	-15	3.1	1	16.7	7.5	< 1.75	5×27	150	0.25-6
			2	50	17	1.25	20×20	200	2-16
$I_0M_1H_2$	-15	2.4	1	25	12	< 1.5	10×25	175	1-8
$I_0M_1H_3$	No convection								
$I_0M_1H_4$	-18	1.8	1	25	7.5	< 2.5	7.5×25	200	0.5-5.5
$I_0M_1H_5$	-13.5	5.2	1	12.5	2	0.4	5×25	100	1-15
			2	50	8	0.9	22×22	50	5-30

a) Melt threshold M_S - The value of the melt fraction threshold M_S for which the viscosity of crustal rocks is reduced depends on many factors in reality, and occurs over a certain range, as mentioned above, section 2.2.3. In the present models where the melt fraction depends linearly on temperature and where a single melt fraction threshold M_S is assumed, M_S directly determines the depth of the melting front. Since different authors argue for key processes at values of M_S of either 0.1 or 0.4 (Burg & Vigneresse 2002; Arzi 1978; Van der Molen & Paterson 1979; Vanderhaeghe & Teyssier 2001; Dufek & Bergantz 2005; Vigneresse 1995), here we compare models with $M_S = 0.1$ and $M_S = 0.3$. A lower value of M_S means that the melting front temperature is lower (720^oC for $M_S = 0.3$ and 640^oC for $M_S = 0.1$). Thus, the thickness of the molten zone is greater for $M_S = 0.1$

than for $M_S = 0.3$ at a given time. The thickness required for the onset of convection is then reached earlier, hence convection starts earlier. However, the vertical velocities and the periods of the convective regimes display the same orders of magnitude in both cases. We conclude that the effect of M_S on the results is secondary.

b) Viscosity of the unmolten domain μ_{UM} - An increase of the "unmolten" viscosity μ_{UM} implies a greater thickness of the unmolten medium in the final convection regime and a slower velocity of convection. We compare $I_0M_1H_1$ and $I_0M_1H_4$.

Modifying μ_{UM} directly impacts Ra_{UM}, thus its increase may lead the system to shift from the global convection regime to the local convection regime (figure 5).

c) Viscosity of the partially molten domain μ_{PM} - An increase of the "partially molten" reference viscosity μ_0 produces flow regimes that approach the regimes with unmolten viscosity μ_{UM}. We illustrate this effect with the test cases $I_0M_1H_0$, $I_0M_1H_1$, $I_0M_1H_2$, $I_0M_1H_3$, where μ_0 is increased from 5×10^{15} $Pa.s$ to 5×10^{17} $Pa.s$. The main consequences of increasing μ_0 are (the values given below are for cases H_0 and H_2 where $\mu_0 = 5 \times 10^{15}$ and 5×10^{16} $Pa.s$, respectively):

- An increase in the cells wavelength λ_{conv} in the first convection regime, from 10 to 25 km,
- An increase in the onset time of convection, t_{conv}, from 2.4 to 12 Myr, in agreement with Howard (1966) who showed that t_{conv} scales as $\mu_0^{2/3}$,
- A decrease in the mean vertical velocity, from 5 to 2.4 $cm.yr^{-1}$, in line with the fact that this velocity scales as $\mu_0^{-1/3}$ (see e.g. eq. (26)),
- An increase in the convection cycle period, τ, from 0.5 to 1.75 Myr,
- A decrease in the number of observed convection regimes (until their disappearance for high μ_0).

2 Parametric study for system configurations with partial melting and heterogeneities

a) The influence of the initial depth distribution of heterogeneities - We illustrate here complementary tests in which the inclusions are initially located in the lower half of the model domain instead of occupying the entire model domain. This could represent a crust where subscale compositional clustering occurs only at these depths. We use parameters from case $I_1M_1H_7$.

The case (Fig. A1) basically shows that the lid of light inclusions is even more easily destroyed as inclusions are dragged into the convection cells. This illustrates that the representation of heterogeneous inclusions is rather a key feature of the middle and upper part of the molten crust, whereas below these depths, the whole medium tends to mix and homogenize. This redistribution of light and heavy inclusions is rather consistent with the layered composition of the crust with a more mafic lower crust and a felsic upper crust (Rudnick et al. 2003; Vanderhaeghe 2009). Exposed migmatitic terranes of various ages, are typically made of alternations of mafic and felsic layers at centimeter to the hundred meter scales (Brown 1995; Sawyer 2010; Saha-Fouotsa et al. 2019), and these structures might represent a significant portion of the mid to lower crust.

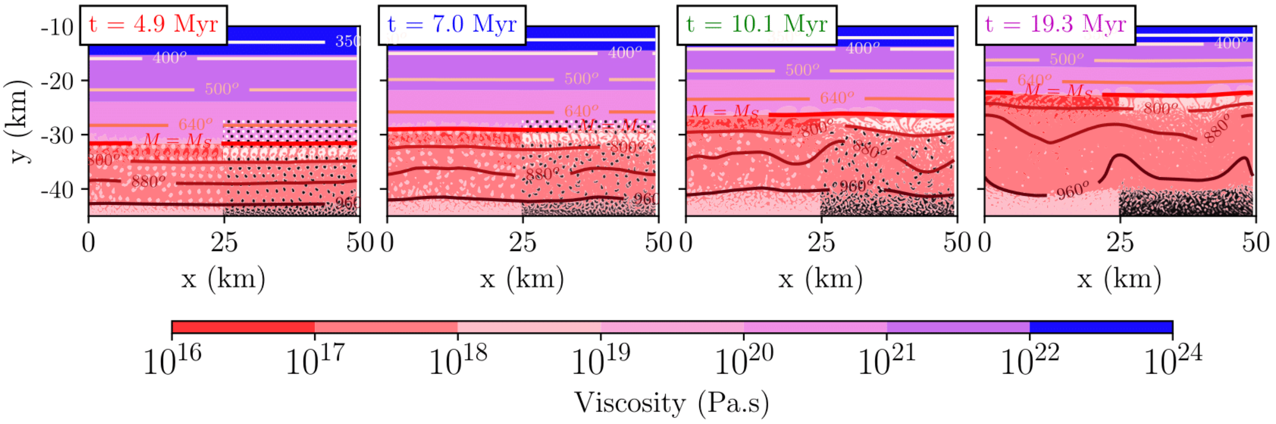

Figure A1. Case $I_1M_1H_7$ with half height inclusions. Snapshots at different times: distribution of viscosity, isotherms and melting front (thick red line). On the right half of the model domain, light and heavy inclusions are shown in white and black, respectively.

b) The influence of heterogeneities size in the layering regime - We illustrate here complementary tests in which the inclusions have a radius of 150 m instead of 300 m, for case $I_1M_1H_7$ representative of the *layering* regime. The light inclusions form clusters that remain sensitive to the convective flow instead of stabilising as a single layer at ca. 20 km depth. Nevertheless at 23 My this layer is apparent. A more detailed study is in preparation (paper part II Louis-Napoleon et al.) to identify the critical size of the inclusions for their layering to occur.

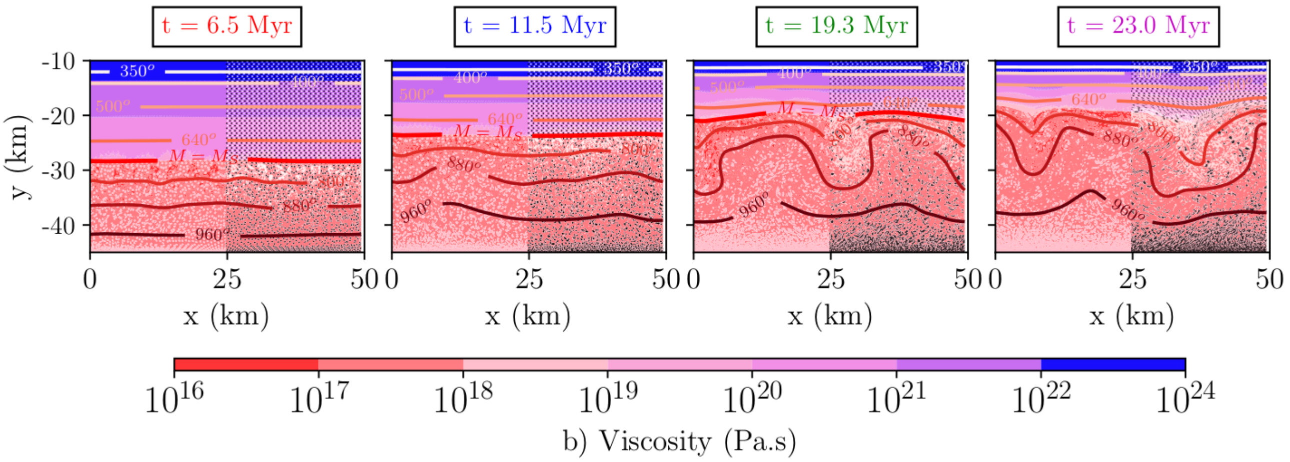

Figure A2. Case $I_1M_1H_7$ with inclusions of radius $r = 150$ m. Snapshots at different times: distribution of viscosity, isotherms and melting front (thick red line). On the right half of the model domain, light and heavy inclusions are shown in white and black, respectively.

3 The influence of latent heat

In this appendix, we assess the influence of explicitly considering latent heat in the governing equations (15)-(18). Ulvrová et al. (2012) showed that for fixed grid methods where the unmolten and the partially molten phases can be regarded as one domain, it is possible to circumvent the need of explicitly satisfying the thermal conditions between the two phases. To this end, they introduce the so-called liquid fraction, denoted f_L, as a function of temperature:

$$f_L\left(T^*\right) = \frac{1}{2}\left[1 - tanh\left(\frac{T_M^* - T^*}{\psi^*}\right)\right], \tag{.1}$$

where $T^* = T/(T_{liq} - T_{sol})$ is the local dimensionless temperature, $T_M^* = T_M/(T_{liq} - T_{sol})$ is that at the location of the melting front and $\psi^* = \psi/H$ can be viewed as a characteristic width of the mushy region. The liquid fraction f_L tends to zero (unity) at low (large) temperatures and is equal to $1/2$ at the location of the melting front.

Using the energy conservation equation written in terms of the enthalpy variable and expressing enthalpy as a function of temperature and liquid fraction, Ulvrová et al. (2012) showed that (18) can be modified as follows:

$$\frac{\partial T^*}{\partial t^*} + \mathbf{U}^* \cdot \nabla^* T^* = \frac{1}{\mathcal{C}^A}\left[\nabla^* \cdot \left(\frac{2}{Ra}\nabla^* T^*\right) + \frac{2Ra_H}{Ra^2}\right], \tag{.2}$$

with

$$\mathcal{C}^A = 1 + St\frac{\partial f_L}{\partial T^*} = 1 + \frac{St}{2\psi^*}\left[1 - tanh^2\left(\frac{T^*_M - T^*}{\psi^*}\right)\right], \tag{.3}$$

where $St = \frac{\mathcal{L}}{Cp\Delta T}$ is the Stefan number, $\mathcal{L}$ is the latent heat of melting, C_p is the heat capacity and $\Delta T = T_{liq} - T_{sol}$. As shown in (.2), the right hand side of (18) is now multiplied by the factor $1/\mathcal{C}^A$. This factor is unity far from the melting front, i.e. when $T^* \gg T^*_M$ or $T^* \ll T^*_M$, and it may becomes very small at the melting front especially if the width of the mushy region is small compared to the system size and/or the Stefan number is large. In dimensional form, the heat equation now reads,

$$\frac{\partial T}{\partial t} + \mathbf{U} \cdot \nabla T = \frac{1}{\mathcal{C}^A}\left[\nabla \cdot (\kappa(T)\nabla T) + \frac{H_r}{C_p(T)}\right]. \tag{.4}$$

In the present work, $St \sim 1$ since $\mathcal{L} \approx 4 \times 10^5$ $J.kg^{-1}$, $C_p \approx 1000$ $J.kg^{-1}.K^{-1}$ and $\Delta T = T_{liq} - T_{sol} = 400^oC$. In order to assess the influence of latent heat in our problem we performed three simulations with identical parameters except for ψ^*. The physical parameters are those of case $I_1M_1H_6$. In the following, it is more convenient to define the characteristic width of the mushy region ψ as a function of the grid size Δx instead of the system size H. More specifically, we performed three simulations with, namely, $\psi \approx \Delta x/17$, $\psi \approx 6\Delta x$ and $\psi = \infty$ (i.e. no latent heat). Note that here $\Delta x = 100$ m and $H = 35$ km, therefore $\psi \approx \Delta x/17$ corresponds to $\psi^* = (\psi/\Delta x) \times (\Delta x/H)$ $= (1/17) \times (100/35000) \approx 2 \times 10^{-4}$.

Figure A3 below presents the time evolution of the melting front location y and the mean vertical velocity $|U_y|$ for all three cases. All curves are superimposed at early times ($t \leq 3$) Myr during the diffusive stage. For $3 \leq t \leq 6$ Myr, the first convective stage appears and the vertical velocity increases at a similar rate for all cases but not at the same time instant. For $t \geq 6$ Myr, convection is fully developed and the evolution of the three cases is roughly similar as the melting front location and the vertical velocity oscillate around an identical mean value at a roughly similar frequency. From figure A3, we conclude that the influence of explicitly taking into account the latent heat does not influence much the dynamics of the system considered in the present work.

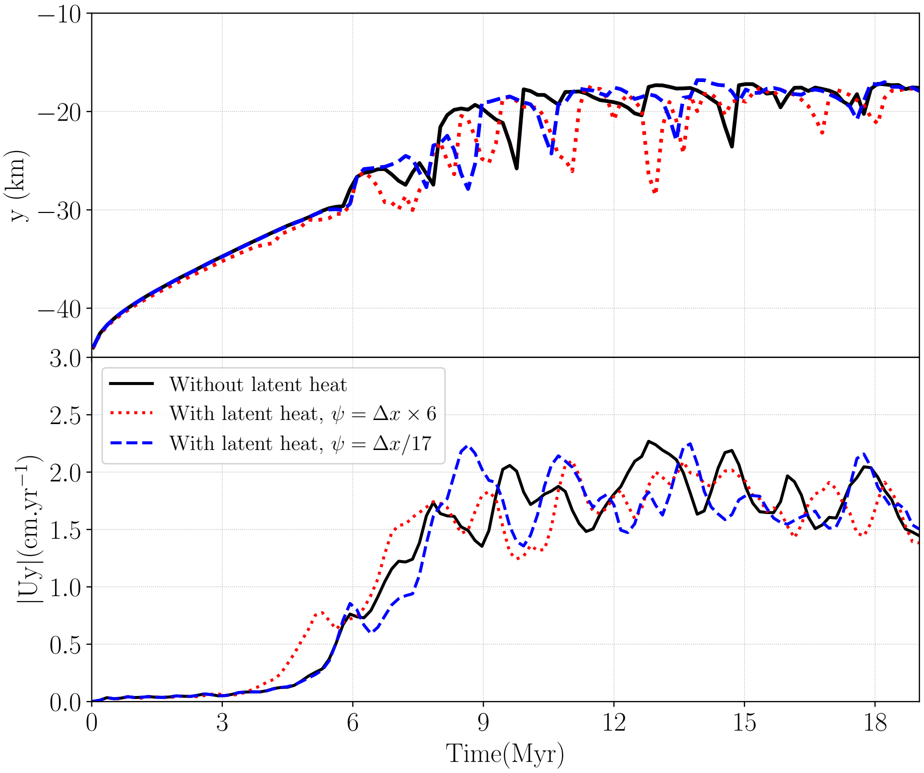

Figure A3. Temporal evolution of the melting front depth and of the mean vertical velocity for a case without latent heat ($I_1M_1H_6$) (black line), and two cases with latent heat controlled by the characteristic width $\psi \approx 6 \times \Delta x$ (red dotted line), and $\psi \approx \Delta x/17$ (blue dashed line).

4 Influence of some numerical parameters and physical assumptions

4.1 Influence of the domain's length L

Figure A4 presents a run similar to case $I_0M_1H_4$ with an extended domain length $L = 90$ km (i.e. twice as large), after 20 Myr. Convection cells are observed to be of the same size as in case $I_0M_1H_4$.

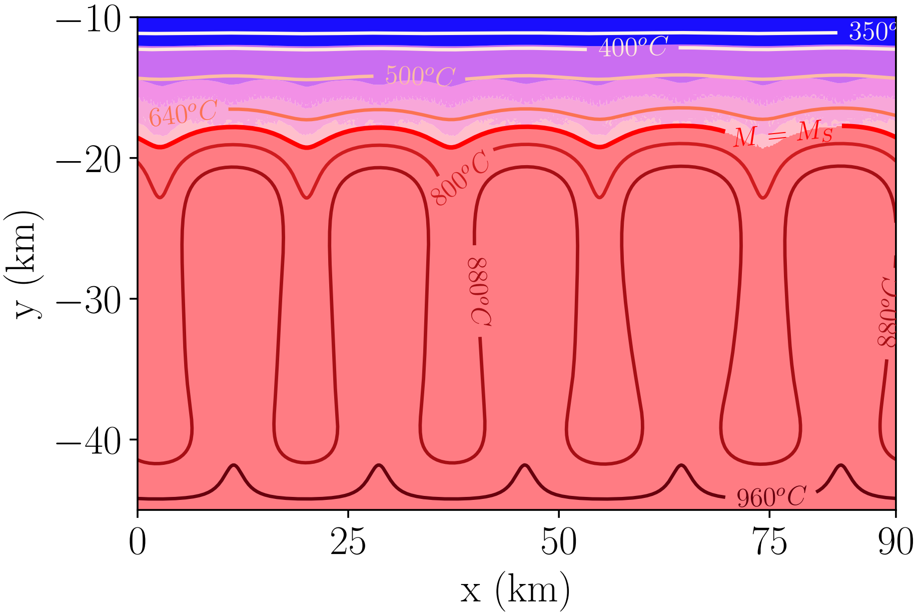

Figure A4. Same case as $I_0M_1H_4$ with a broader domain length $L = 90$km, after 20 Myr. Convection cells have the same size as in case $I_0M_1H_4$.

4.2 Influence of the choice of $\dot{\varepsilon}_{min}$

In this section, we assess the sensitivity of the threshold strain-rate $\dot{\varepsilon}_{min}$ chosen *a priori* for the unmolten fluid rheology. Figure A5 presents the temporal evolution of the mean vertical velocity and the viscosity - temperature - inclusions distribution at various times of three cases corresponding to three values of $\dot{\varepsilon}_{min} = 10^{-16}$, 10^{-15} and 10^{-14} s^{-1}. It is shown that the results are not significantly influenced by the specific value of $\dot{\varepsilon}_{min}$.

(a)

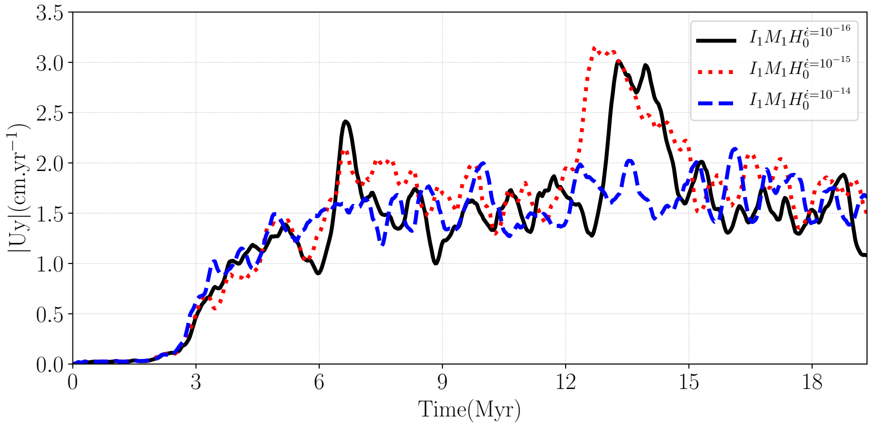

(b) $\epsilon_{min} = 10^{-14}$ s^{-1}

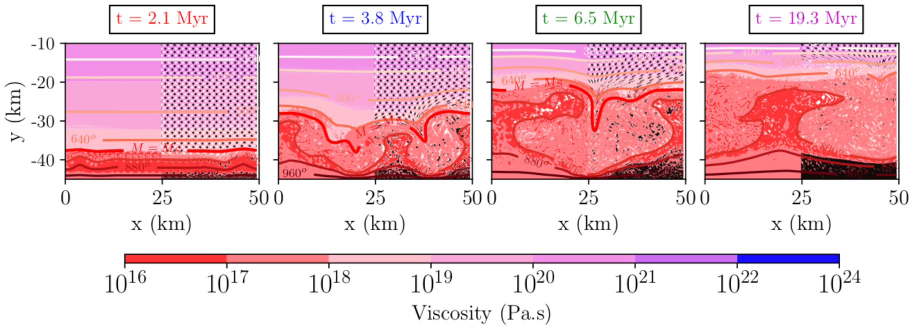

(c) $\epsilon_{min} = 10^{-15}$ s^{-1}

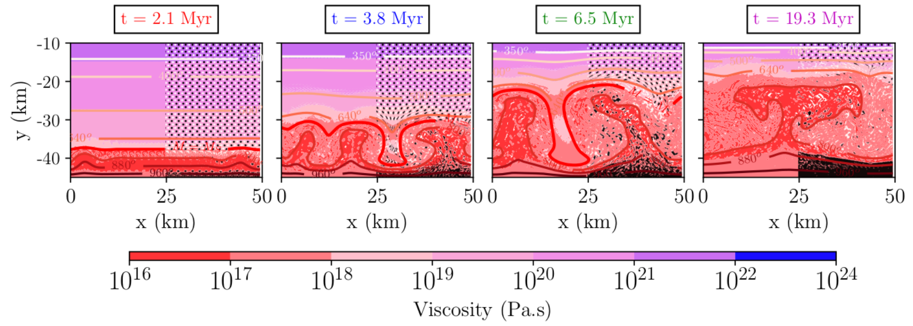

(d) $\epsilon_{min} = 10^{-16}$ s^{-1}

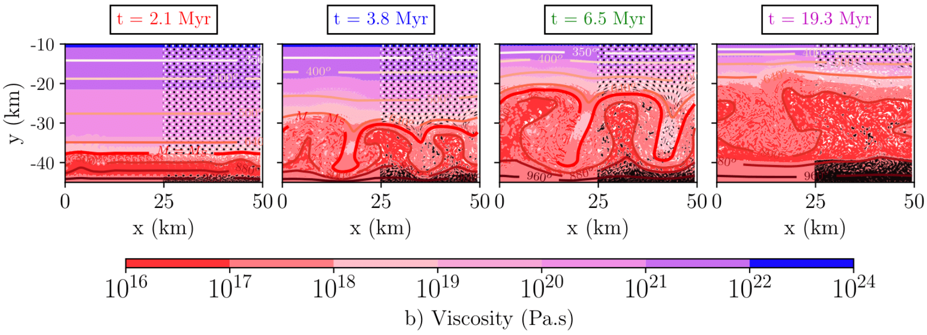

Figure A5. a) Time evolution of the mean vertical velocity for three cases with different values of the initial strain-rate ϵ_{min}. **b) c)** Snapshots of the viscosity, temperature and inclusions distribution in these three cases.

4.3 Influence of Archimedes number

The sensitivity of simulations results on Archimedes number Ar is ilustrated here, while complementary details can be found in Louis-Napoléon et al. (2020). Figure A6 presents the temporal evolution of the melting front and the distributions of viscosity - temperature - phases for case $I_1M_1H_0$ and three values $Ar = 0.02$, 0.2 and 2. In this case, convection dominates over diapirism. The results are not significantly influenced by the specific value of Ar in terms of the melting front propagation rate and of the spatial distribution of convective cells and inclusions. Note that these flow characteristics become slightly distinct (e.g. somewhat slower) at the highest value $Ar = 2$, which is consistent with the condition $Ar < 1$ (cf. Louis-Napoléon et al. 2020).

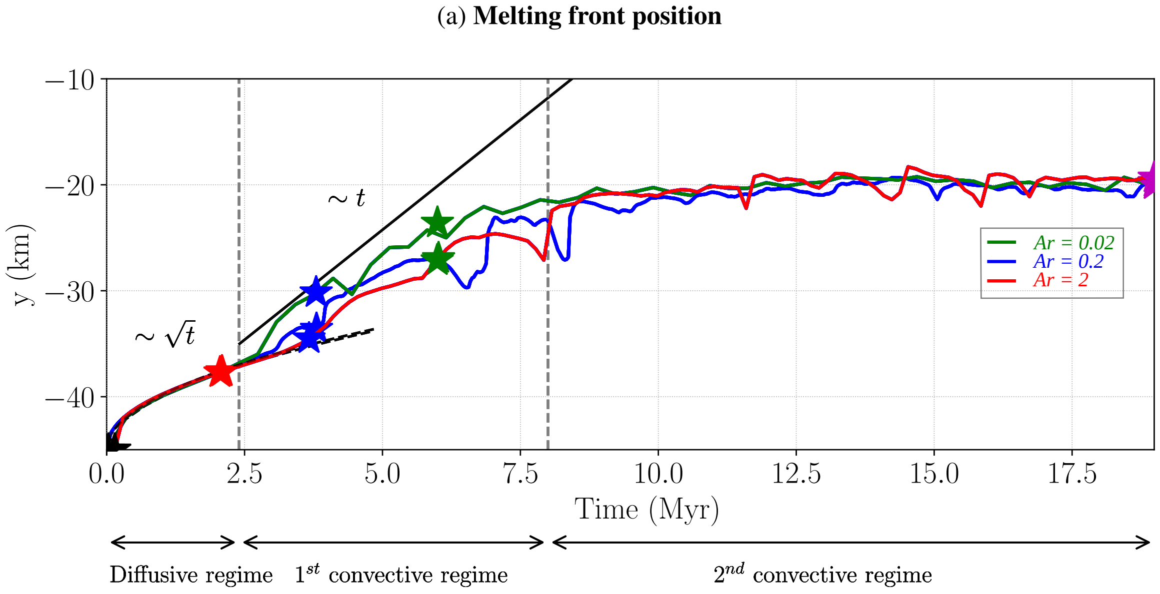

(b) $Ar = 0.02$

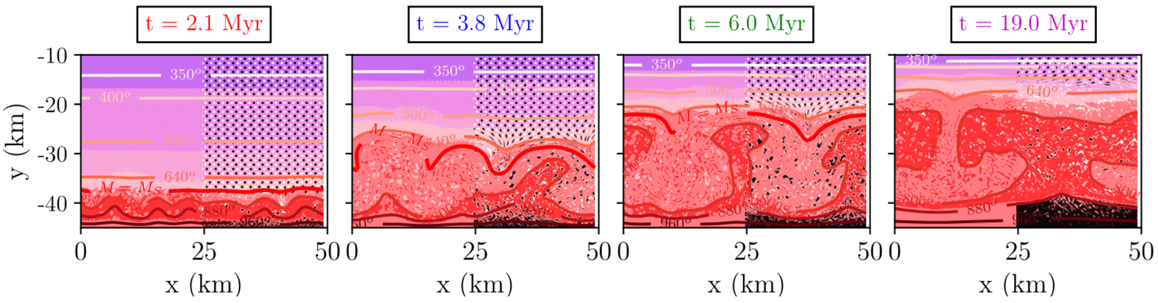

(c) $Ar = 0.2$

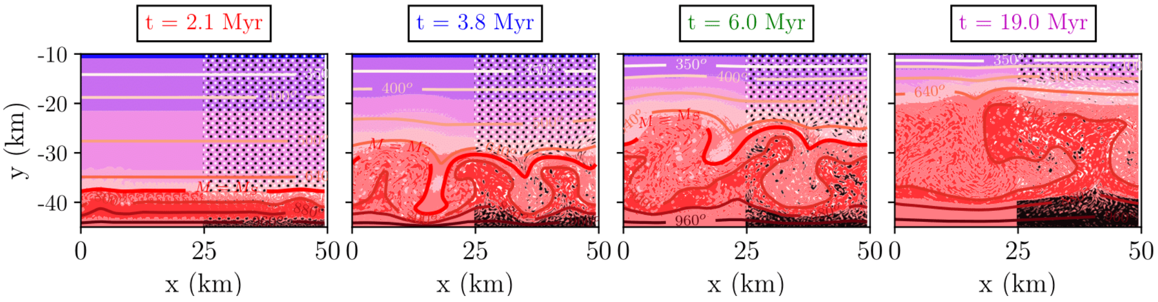

(d) $Ar = 2$

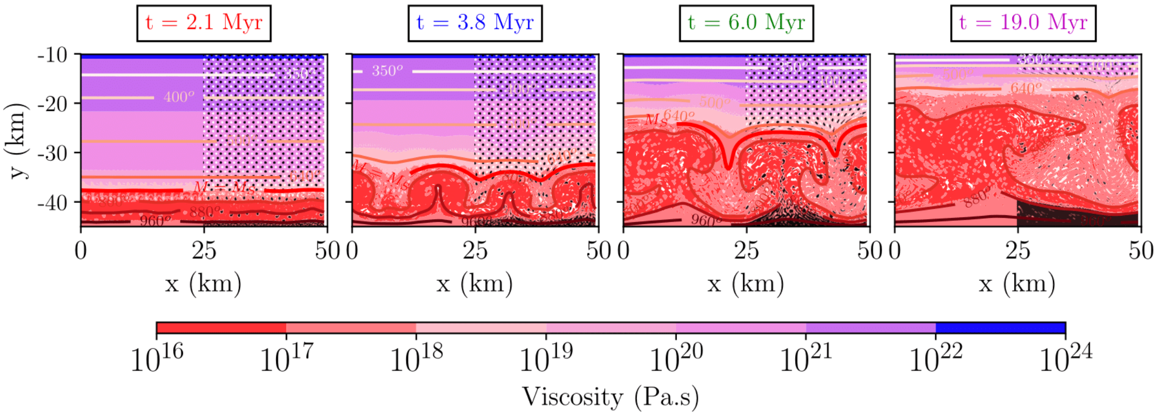

(e) $Ar = 0.02$

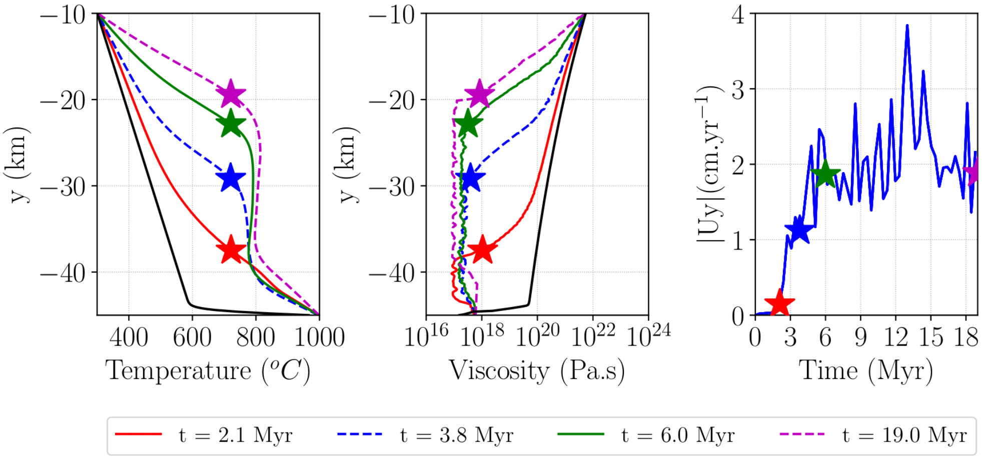

(f) $Ar = 0.2$

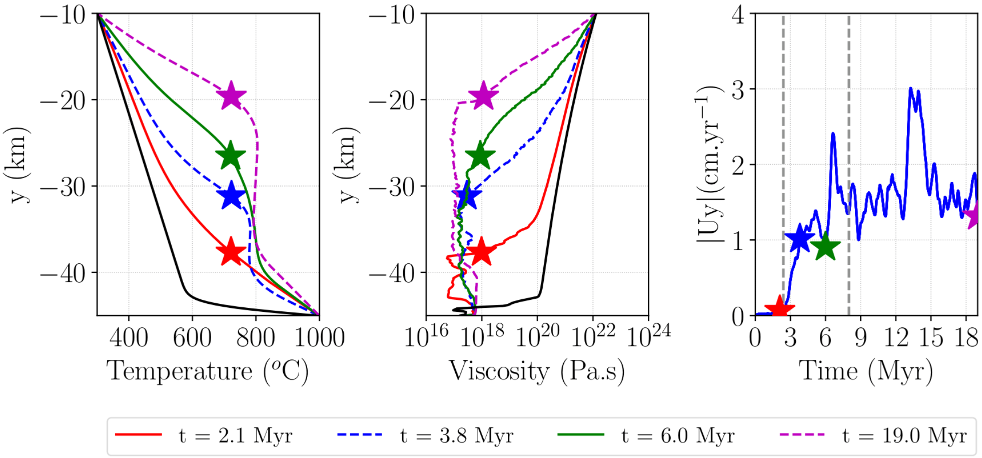

(g) $Ar = 2$

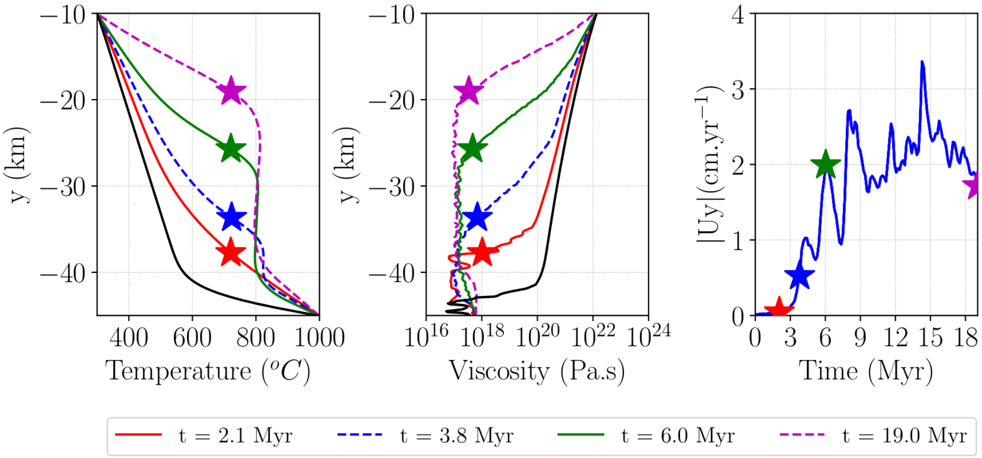

Figure A6. a) Time evolution of the melting front position for three cases with different Archimedes numbers, $Ar = 0.02$, $Ar = 0.2$, $Ar = 2$. b-c-d) Snapshots of the viscosity, temperature and inclusions distribution in these three cases. e-g-h) Vertical profiles of the horizontally-averaged temperature and viscosity, respectively (stars indicate melting front location) and time evolution of the mean vertical velocity for these three Ar.

4.4 Applicability of the incompressibility condition to our geodyamic setting

As mentioned in section 3.2, our model setting involves non-negligible density variations over the inclusions travelling distances, of several tens of kilometers. One may thus wonder if they are subjected to local expansion (for the rising light particles) or contraction (for the settling heavy particles) due to hydrostatic pressure variations, in nature.

Here, this effect can be estimated by comparing two characteristic length scales, namely $\mathcal{L}$ the typical distance covered by the inclusions and $\mathcal{H}$ the 'pressure head' related to expansion/contraction effects. We choose $\mathcal{L} = H_T/2$ where H_T is the total crustal depth. We estimate $\mathcal{H} \approx \frac{P_0}{\Delta\rho g}$ with P_0 a reference pressure and $\Delta\rho$ the density difference between the inclusions and the ambient fluid (BED). We write $\Delta\rho = |\rho_{i\neq 1} - \rho_1|$ for the light (i=2) and heavy (i=3) inclusions, respectively. For P_0, we take the maximum lithostatic pressure at the bottom of the computational domain, $P_0 \approx \rho_1 g H_T$. Taking the following values: $H_T = 45$ km, $\rho_1 = 2700$ kg.m^{-3}, $\rho_2 = 2500$ kg.m^{-3}, $\rho_3 = 2900$ kg.m^{-3} and $g = 9.81$ m.s^{-2}, we obtain $\mathcal{L} = 22.5$ km, $P_0 \approx 1.2$ GPa and $\mathcal{H} \approx 607$ km. Hence, $\mathcal{L}/\mathcal{H} \approx 4 \times 10^{-2} \ll 1$. This indicates that the inclusions are unlikely to 'feel' any expansion or contraction during displacement.

5 Settling inclusions in Rayleigh-Bénard convection: a comparison with previous studies

In this appendix, we compare the present simulations with previous studies of the interaction between rigid settling particles and Rayleigh-Bénard convection. This includes numerical simulations by Höink et al. (2005); Verhoeven & Schmalzl (2009); Patočka et al. (2020) and experiments by Lavorel & Le Bars (2009).

Figure A7 presents the residence time of particles in Rayleigh-Bénard convection in the diagram (St, Λ)= (particle response time, buoyancy ratio) obtained by Patočka et al. (2020). In this figure, the residence time is normalized by the terminal time τ_s, which is the time required by a particle to cross the characteristic domain size ($H_T/2$) at its Stokes velocity (v_s). With our notations, St and Λ become $St \approx \frac{1}{3}\left(\frac{r}{H_T/2}\right)^2 \sqrt{Ar_{PM}}$ and $\Lambda \approx \frac{2}{3}B$, respectively. Recall that we assumed here a density ratio between the particles and the ambient fluid close to one, as is the case for our inclusions with respect to the BED.

Our numerical experiments are plotted with red filled circles standing for the light inclusions and black crosses for the heavy inclusions. They all fall in the 'dust-like' regime, and hence the residence time of our inclusions, denoted τ_r, is such that $\tau_r \approx 3\tau_s$ (Patočka et al. 2020). Using Eq. (13) and the definition of the Stokes velocity $v_s = (2\Delta\rho g r^2)/(9K_{eff}^{PM})$, the terminal time $\tau_s = (H_T/2)/v_s$ can be written in dimensionless form as $\tau_s^* = q\tau_s = \left(\frac{3H_T}{4r}\right)^2$. Accordingly, the dimensionless residence time is $\tau_r^* \approx 3\tau_s^* = 3\left(\frac{3H_T}{4r}\right)^2$. In our models, we have $H_T = 45$ km and $r = 300$ m, so that we can estimate the residence time $\tau_r^* \approx 3\left(\frac{3H_T}{4r}\right)^2 \approx 4 \times 10^4$.

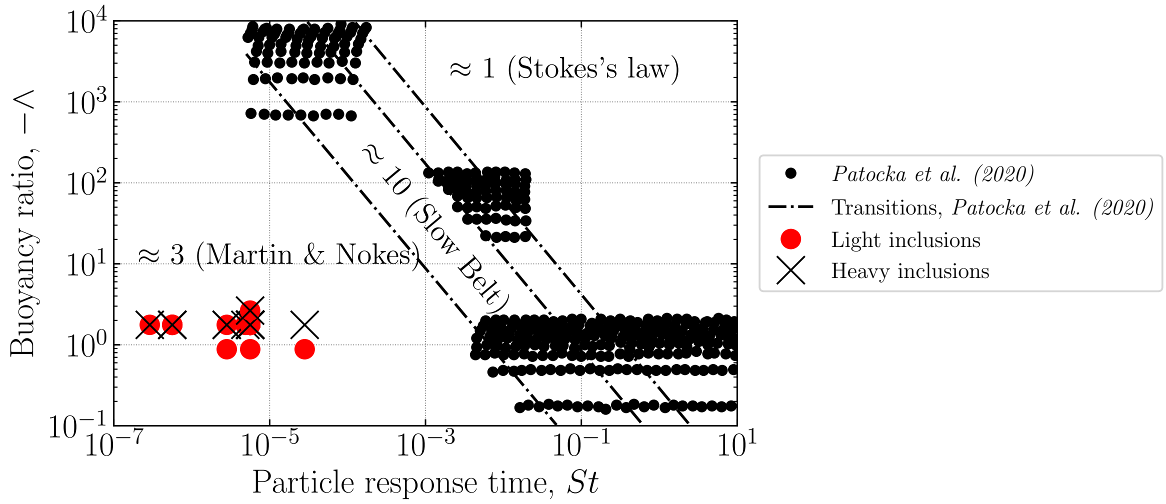

Figure A7. Diagram of the residence time of particles in Rayleigh-Bénard convection, after Patočka et al. (2020), normalized by the terminal time (ratio of the domain size to the Stokes velocity) in the parameter space (St, Λ) with $St \approx \frac{1}{3}\left(\frac{r}{H_T/2}\right)^2 \sqrt{Ar_{PM}}$ and $\Lambda \approx \frac{2}{3}B$. Lines separate four regimes, of which the 'dust-like' regime where the residence time ≈ 3 (bottom left part of the diagram, corresponding to the ratio of Stokes velocity v_t to convection velocity u_{rms} less than 0.02); the 'transitional' regime ($0.02 \leq v_t/u_{rms} \leq 0.4$) and the 'bi-linear' regime ($0.4 \leq v_t/u_{rms} \leq 2.0$) where the residence time can increase up to 10; the 'stone-like' regime where the residence time ≈ 1 (upper right of the diagram with $v_t/u_{rms} > 0.4$). Our numerical experiments are plotted with red filled circles standing for the light inclusions and black crosses for the heavy inclusions. They all fall in the 'dust-like' regime. The other plotted symbols represent Patočka et al. (2020)'s 2D simulations with various particle sizes, density ratios and thermal forcing.

For each run, one can compute the dimensionless time (Eq. 13) $q^{-1} = \frac{2K_{eff}^{PM}}{\rho_1^{L0}\alpha g \Delta T_{PM}(H_T/2)}$ with the parameters given in Table 3, to estimate the dimensional residence time $\tau_r \approx 4 \times 10^4 q^{-1}$. For example, in case $I_1M_1H_0$, we have $\mu_1^0 = 5 \times 10^{15}$ Pa.s, hence $K_{eff}^{PM} \approx 1.7 \times 10^{17}$ Pa.s (Eq. 23).

Then, using $\rho_1^{L0} = 2700$ kg.m^3, $\alpha = 3 \times 10^{-5}$ K^{-1}, $g = 9.81$ m.s^{-2}, $\Delta T_{PM} = 1000 - 720 = 280$ ^{o}C and $H_T = 45$ km, we obtain $q^{-1} \approx 2200$ yr. Consequently, the residence time of the inclusions in case $I_1 M_1 H_0$ is $\tau_r \approx 4 \times 10^4 q^{-1} \approx 88$ Myr.

It is worth noting that we expect the inclusions residence time in all our models to be larger than 88 Myr since case $I_1 M_1 H_0$ has the lowest viscosity. Consequently, since we run our models for about 20 Myr, the present analysis indicates that some inclusions are expected to remain in the convective zone, as is indeed observed (Fig. 7).

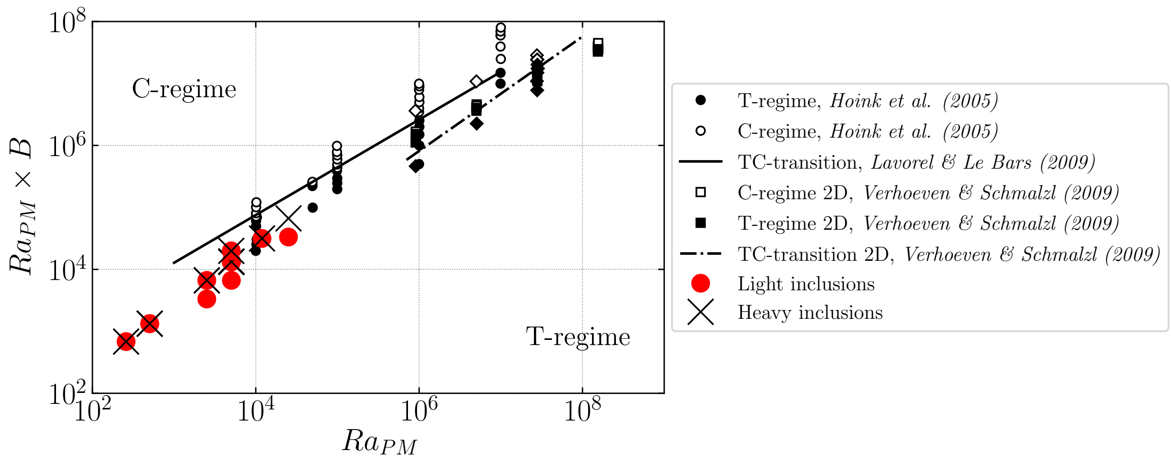

Figure A8. Interaction between particles and convection: regime diagram separating the so-called T-regime which is dominated by thermal convection and the C-regime characterized by the existence of a sediment layer and a suspension layer with few particles (where the volume fraction is $\phi < 0.3$), in the parameter space $(Ra_{PM}, Ra_{PM} \times B)$. $Ra_{PM} = \frac{\rho \alpha g \Delta T_{PM} (H_T/2)^3}{\kappa K_{eff}^{PM}}$ is the Rayleigh number of the partially molten crust and $B = \frac{\Delta \rho}{\rho \alpha \Delta T}$ is the buoyancy number, with $\Delta \rho$ the density difference between the particles and the ambient fluid. Present work: (red filled circles) light inclusions, (black crosses) heavy inclusions in the suspension regime only. Höink et al. (2005): (open and closed black circles) 2D computations at infinite Prandtl number. Verhoeven & Schmalzl (2009): (open and closed black squares) 2D computations, (open and closed black diamonds) 3D computations, (black dashed line) theoretical criterion. Filled symbols correspond to the T-regime and open symbols to the C-regime. Lavorel & Le Bars (2009): (black solid line) theoretical criterion for the transition between regimes based on a critical equivalent Peclet number $Pe_s = 3.5 \times 10^3$, with $Pe_s = \frac{2\, Ra\, B}{9\pi} \left(\frac{Ra_c}{Ra}\right)^{\beta} \left(\frac{r}{H}\right)^2$, $\beta = 0.77$ and $Ra_c = 1708$.

Figure A8 presents the regime diagram separating the so-called T-regime dominated by thermal convection and the C-regime characterized by the existence of a sediment layer and a suspension layer with few particles (where the volume fraction is $\phi < 0.3$), in the $(Ra_{PM}, Ra_{PM} \times B)$ space. $Ra_{PM} = \frac{\rho \alpha g \Delta T_{PM} (H_T/2)^3}{\kappa K_{eff}^{PM}}$ is the partially molten crust Rayleigh number, and $B = \frac{\Delta \rho}{\rho \alpha \Delta T}$ is the buoyancy number, with $\Delta \rho$ the particles and the ambient fluid density difference. Note that $Ra_{PM} \times B$ corresponds to the chemical Rayleigh number defined by Verhoeven & Schmalzl (2009).

The present simulations are performed for small Rayleigh numbers since our system is meant to describe partially molten crust, while that of the previous authors is meant to describe the mantle. Note also that it is difficult to conclude about whether our simulations lie in the T- or C-regime since (i) our plotted points -at least those with large Ra_{PM}- seem close to the transition identified by the previous authors, and (ii) as mentioned above, the time duration of our runs is smaller than the expected typical residence time of the inclusions. Simulation time durations larger than the expected expected residence time are thus required to further clarify our flow regimes. This stands beyond the scope of the present work.

6 Regimes diagram expressed in terms of crustal viscosities

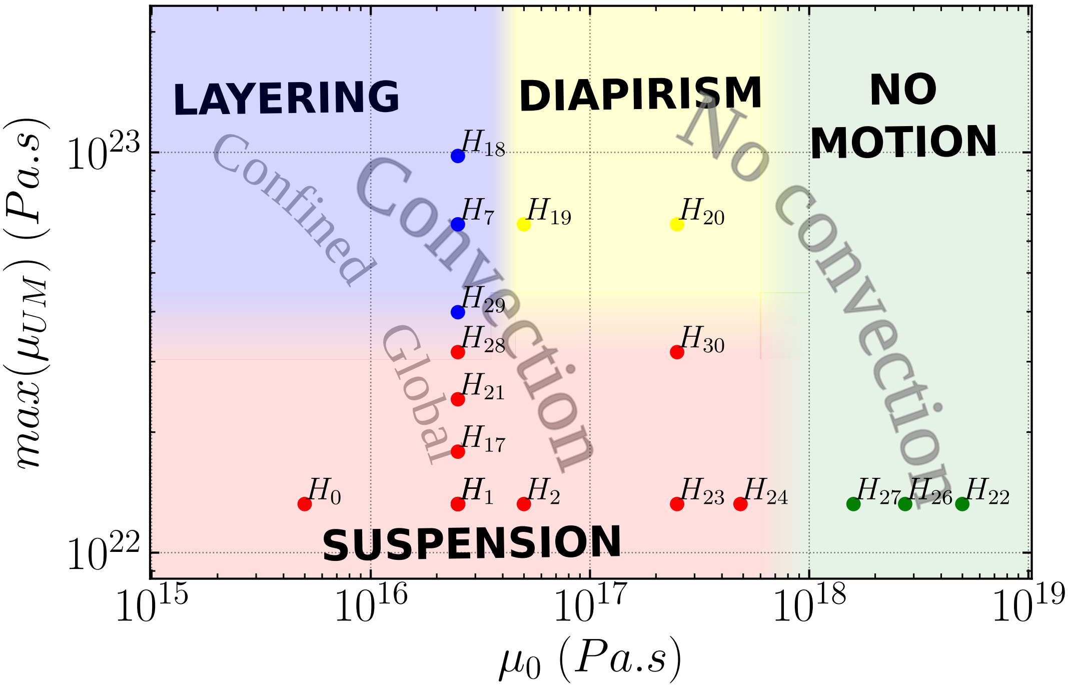

Figure A9. Flow regimes diagram for a hot orogenic crust that is melting and contains heterogeneous inclusions, as a function of the system's lowest viscosity μ_0 (molten rheology in Eq. (9) with $M = 1$) and its highest viscosity $max(\mu_{UM})$ (unmolten rheology in Eq. (9) with $T = 300^o$C, $\dot{\varepsilon} = 10^{-16}$ s^{-1}, $n = 2.3$, $Q = 1.54 \times 10^5$ J.mol^{-1}). Associated threshold values of A and μ_0 for each regime are provided in Table 4.